UNIVERSITÀ DEGLI STUDI DI PADOVA

Dipartimento di Fisica e Astronomia "Galileo Galilei"

Master Degree in Physics

Final Dissertation

Performance assessment of the new plasma position reflectometer antennas for the RFX-mod2 device

Thesis supervisor
Prof. Matteo Zuin
Thesis co-supervisor
Dr. Roberto Cavazzana
Dr. Gianluca De Masi

Candidate
Federico Ruffini

Academic Year 2022/2023

Abstract

The present thesis is dedicated to the characterization of the performances of the new antennas to be installed on the RFX-mod2 plasma position reflectometer (PPR). RFX-mod2 is the upgraded version of the RFX-mod device, in operation at Consorzio RFX and dedicated to the study of magnetically confined plasmas. One of the new RFX-mod2 diagnostics will be a PPR system for real time control of the plasma position within the vacuum chamber. The main goal of this thesis is, thus, to study the performance, i.e. the radiation pattern, of the antennas which will be mounted on the PPR. In particular, according to the different assembly constraints, these antennas feature two different geometries: a pyramidal horn shape and a hoghorn shape. The important feature of these antennas is that they were built through additive manufacturing technique. Since such kind of antennas have never been used in any fusion machine, their characterization assumes a certain relevance. The experimental radiation patterns of the antennas is then compared with both the theoretical model and the numerically simulated patterns through the COMSOL Multiphysics software. As additional analysis, the experimental layout on RFX-mod2 is reproduced in laboratory using a metallic mirror with the goal of mimicking the performance on the plasma. This last step is important in order to have a first preliminary test on the functioning of the reflectometric system. Overall, the results indicate that both antennas have a good agreement, at least in the angular distribution of the emitted radiation, with respect to the simulated models. The hoghorn antenna, as expected, turns out to be more critical with a lower directivity and higher deviation from the simulated model, despite it proves to able to correctly estimate the distance from the reflecting mirror.

Contents

Chapter 1

Introduction

1.1 The need for Fusion Energy

We live in a world whose population has been constantly raising over the last hundred years. The same holds for the industrialisation level, especially in the developing nations. The striking consequence of the latter fact is that, as shown in Figure 1.1, world energy consumption has been almost constantly on the rise, with a particularly steep increase in the last 50 years. Covid-19 pandemic contributed to a trend reversal in 2020, but during 2021 the energy consumption already started to climb up again. It is clear from Figure 1.1 that the vast majority of the required energy is derived from oil, followed by coal, gas, and only then by a non-fossil fuel power. The massive use of fossil fuels has a significant impact on CO_2 emissions, and it is widely recognised that these emissions are one of the primarly causes of climate change and atmosphere overheating[1]. The world, thus, urgently needs new energy sources able both to satisfy the humanity's huge energy request and to safeguard the environment.

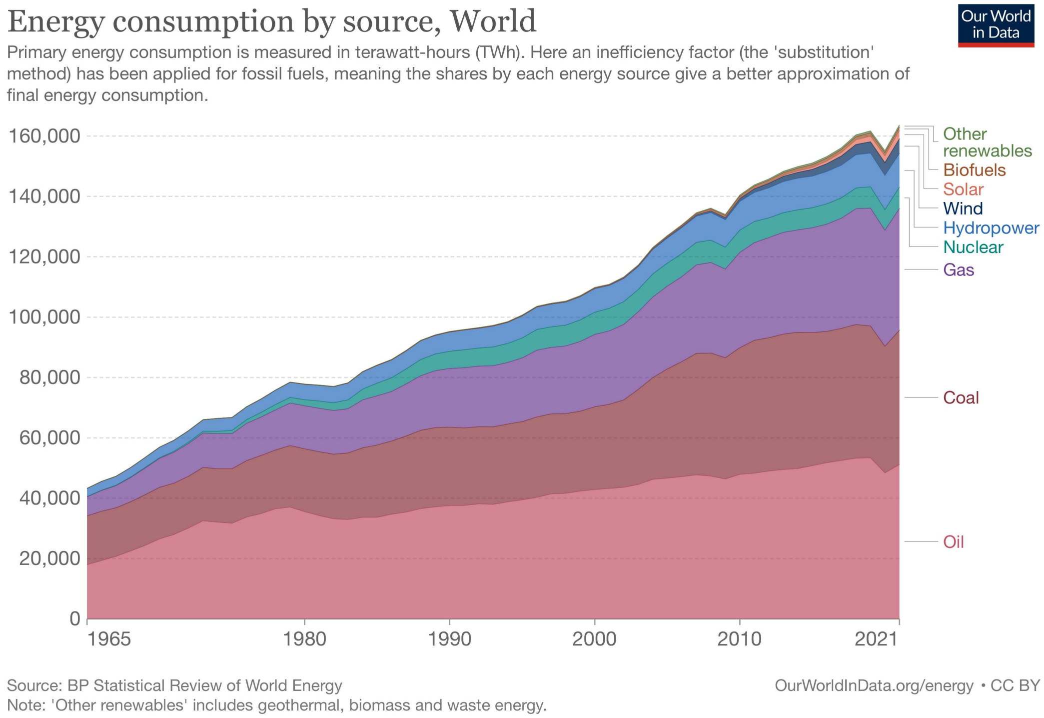

Energy consumption by source, World

Primary energy consumption is measured in terawatt-hours (TWh). Here an inefficiency factor (the 'substitution' method) has been applied for fossil fuels, meaning the shares by each energy source give a better approximation of final energy consumption.

Source: BP Statistical Review of World Energy

Note: 'Other renewables' includes geothermal, biomass and waste energy.

Figure 1.1: Global energy consumption divided by year [2]

It is for these reasons that nuclear fusion research is of primarly interest for the scientific community. The basic principle behind the exploitation of nuclear fusion for energy producton is that the nuclei of some atomic species can fuse giving raise to a heavier element and releasing a great amount of energy. Every atomic species indeed, as can be seen from Figure 1.2, has its own binding energy, i.e the energy needed to remove one nucleon from the stable configuration. In Figure 1.2 the plot of the binding energy per nucleon as a function of mass number A is shown, and it can easily be seen that until ^{56}Fe binding energy has an increasing trend with A. This means that fusing two atoms in order to create an heavier one leads to an increase of the total binding energy. This energy difference is released and it is what's meant by nuclear fusion energy.

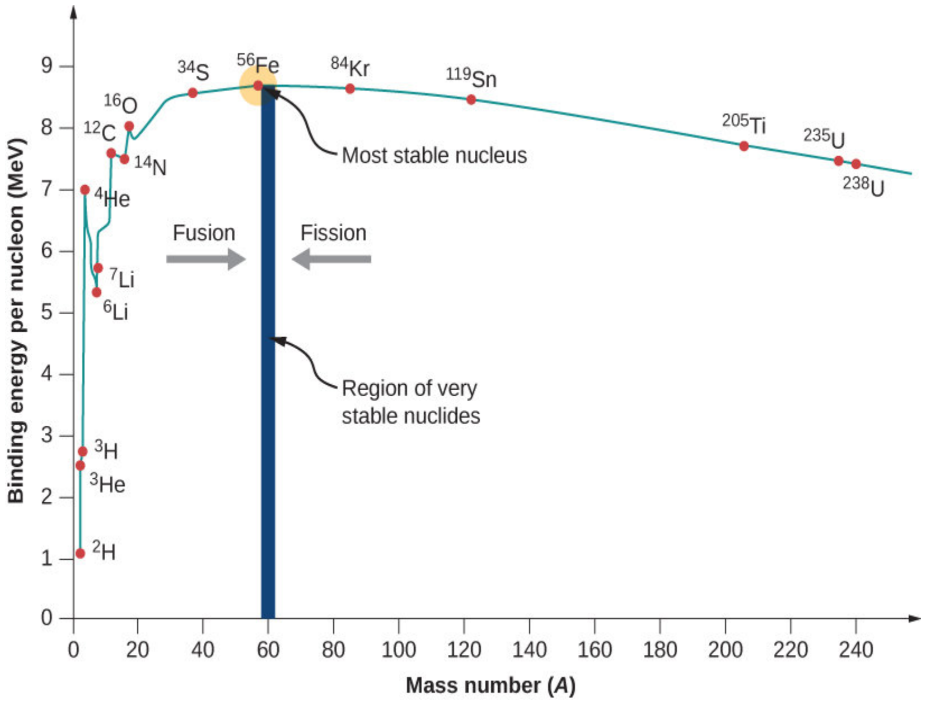

Figure 1.2: Binding Energy per nucleon as a function of mass number[3]

Many different reactions can release fusion energy, but the most interesting are the following ones:

$$^{2}D +^{2} D \rightarrow^{3} He +^{1} n + 3.27\ Mev \tag{1.1}$$

$$^{2}D +^{2} D \rightarrow^{3} T +^{1} H + 4.03\ Mev \tag{1.2}$$

$$^{2}D +^{3} T \rightarrow^{4} He +^{1} n + 17.6\ Mev \tag{1.3}$$

$$^{2}D +^{3} He \rightarrow^{4} He +^{1} H +^{1} n + 18.3\ Mev \tag{1.4}$$

However, while fusion processes happen naturally in the stars, on Earth nuclear fusion is quite an unlikely process, limited by the high temperature and pressure required to overcome the Coulomb repulsion which tends to separate different nuclei. The probability for a fusion reaction to occur is proportional to the cross-section σ, which is dependent on the particles' energy as shown in Figure 1.3:

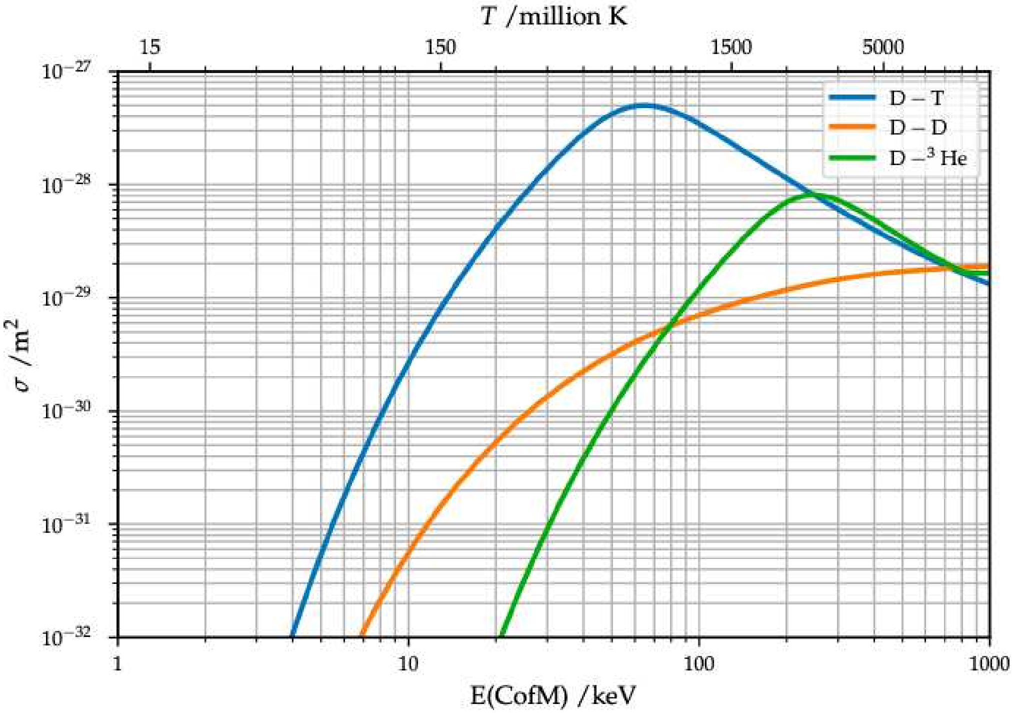

Figure 1.3: Cross sections of the main fusion reactions, as a function of both the center of mass energy [keV] and the temperature T [10^6K], from [4]

It's easy to see from the picture above that, at the temperatures which are experimentally reachable ($T \sim 10^7\ K$), the reaction with the highest cross section is the one involving Deuterium and Tritium, also called D-T reaction. Regarding Deuterium and Tritium availability, the first one is practically limitless since it can be found in the ocean's water with an abundance of 0.015%, while the latter is quite rare but will be produced by future reactors themselves. They will, indeed, be provided with a Lithium blanket that will produce Tritium through the reaction:

$$n +^6 Li \rightarrow^4 He +^3 T + 4.8\ Mev \tag{1.5}$$

Where the neutrons are the ones coming from the fusion reactions. Thus, the limits are set on Lithium's availability and not on Tritium's one. Lithium's production, at present, is by far less problematic with respect to what concern Tritium's extraction. Considering all of this, it's easy to understand that nuclear fusion research is remarkably attractive, since it could lead to a practically limitless and sustainable source of energy.

1.2 Nuclear fusion research in the world

In the previous section an introduction to explain why fusion energy could, in principle, represent a limitless energy source was given. Practically, realizing fusion and exploiting its energy is, unfortunately, a very complex task. Since the 50s of the previous century, when research on nuclear fusion started, many different approaches have been investigated. To the present day, the most studied and consolidated approach towards nuclear fusion is the so-called Magnetic Confinement approach. This approach consists in exploiting the D-T reaction creating a plasma of Deuterium and Tritium. The plasma is brought to the temperature and pressure conditions needed for fusion by confining it in a toroidal shape with the magnetic field created by system of coils, of which an illustration is given in Figure 1.4. The plasma will of course be sensitive to coils, being composed by ionized particles.

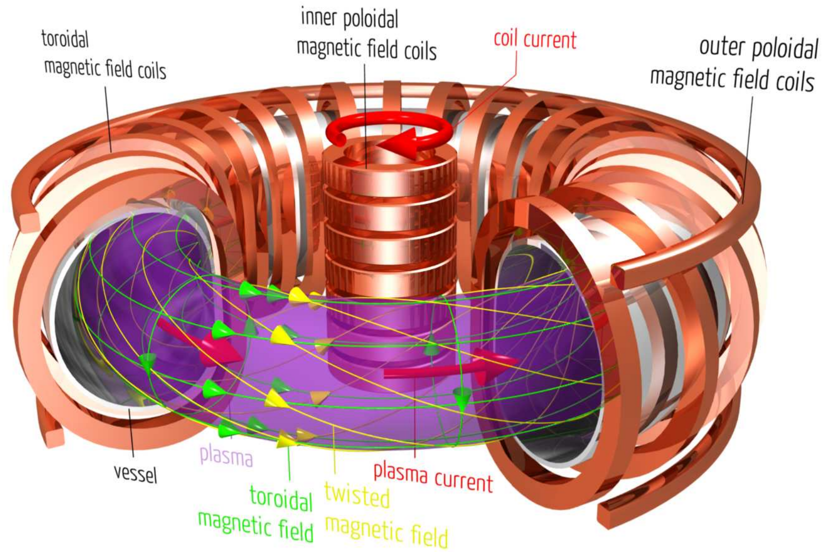

Figure 1.4: Representation of a magnetic confinement fusion machine (Tokamak type)[5]

To give a very qualitative idea of how ionized particles are confined in a torus, it is convenient start from the well-known fact that a charged particle of charge q and mass m, in the presence of a constant magnetic field $\mathbf{B}$, is confined on the plane perdendicular to field lines within its gyroradius :

$$r_g = \frac{mv_\perp}{|q|B} \tag{1.6}$$

Where $v_\perp$ is the velocity of the particle in the direction perpendicular to field lines. So, if one has a sufficiently high toroidal field component, the particles will be well confined on the poloidal plane of the torus. This field component, with reference to Figure 1.4, is provided by the toroidal field coils. The confinement on the toroidal plane, instead, is partially ensured by the closed structure of the torus. It's also important to say that a poloidal field is usually present, with the aim of correcting some complicated drifts which won't be discussed in this work. Different kind of machines working with magnetic confinement exist, but maybe the most important is the Tokamak. The main feature of a Tokamak is that it has a predominant toroidal field component alongside with a usually much smaller poloidal component for plasma stabilization. It is also characterized by an an axisymmetric plasma shape. The most important project on Tokamak physics is without any doubt the ITER project, an international collaboration aimed at the construction of the biggest Tokamak ever built, which will hopefully allow to make significant steps forward towards the production of commercial nuclear fusion energy.

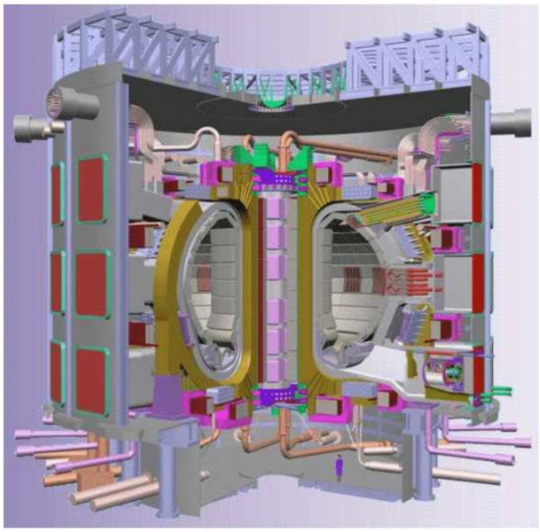

Figure 1.5: ITER's tokamak [6]

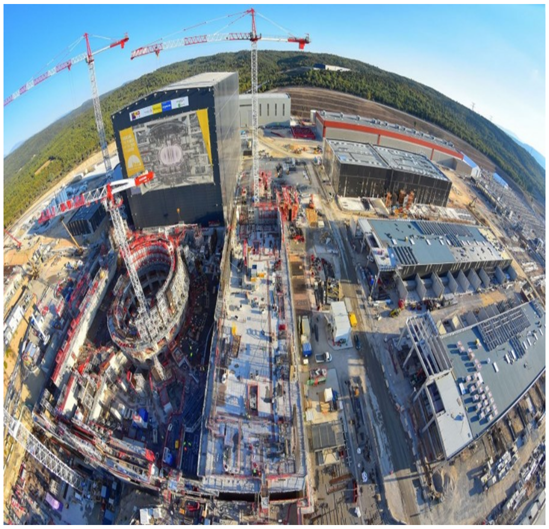

Figure 1.6: ITER's construction site in October 2017 [7]

ITER, of course, is not the only fusion experiment present in the world. By now, indeed, basically every continent has various experiments on nuclear fusion, each one which focuses on a particular aspect of the problem. This work was carried out at Consorzio RFX, an important Italian research center on nuclear fusion, whose history and achievements will be illustrated in the following section.

1.3 Nuclear Fusion in Padua: the RFX Consortium

Research on nuclear fusion in Padua started at the beginning of the 50s of the last century, and rapidly developed until the construction of the first two experiments on fusion: Eta Beta I and Eta Beta II (1970-1980). A crucial milestone was the constitution, in 1996, of Consorzio RFX, which from that moment was the reference for fusion research in Padua and in Italy. The main focus of Consorzio RFX has always been the investigation of the so-called Reversed-Field Pinch(RFP) configuration[8]. RFP is a particular plasma configuration which differs from the Tokamak configuration mainly because of the fact that the toroidal field component gets reversed in the outer part of the torus, as illustrated in Figure 1.7. This feature has a huge impact on the plasma behaviour and on the plasma parameters. An RFP device requires, indeed, a lower magnetic field and has no need of external heating, in principle being able to fully rely on Ohmic heating.

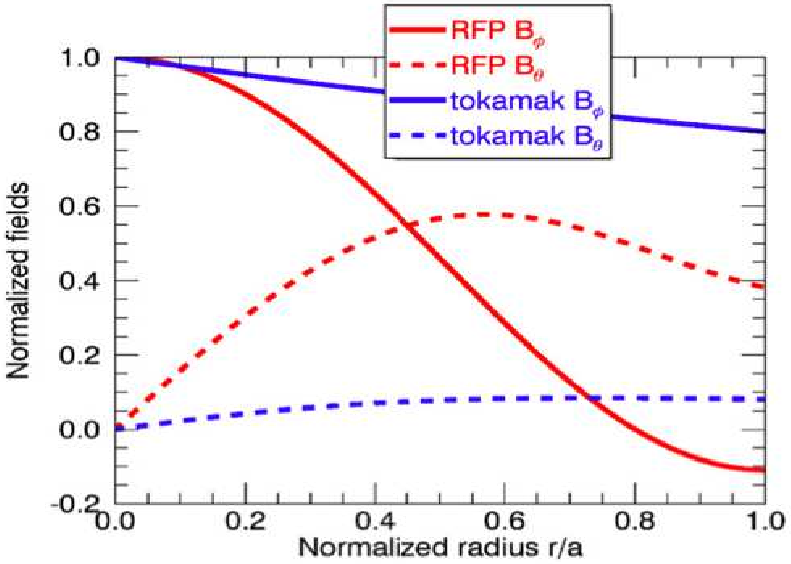

Figure 1.7: Tokamak and RFP radial field behaviour: reversal is evident in the latter [8]

The main aspects of the RFP configuration were studied in Padua since 1996 with the experiments RFX and RFX-mod, leading to outstanding results. RFX-mod is currently dismounted, waiting for the assembly of a new machine which will continue the studies on the RFP configuration: RFX-mod2. With respect to RFX-mod, the new machine has a larger plasma volume, and an improved plasma control system. These changes are expected to reduce both the magnetic chaos of the plasma core and the localized deformation, in order to diminish the power deposition of the first wall. It is important to state that both RFX-mod (due to its control system of 192 saddle coils) and RFX-mod2 (due to its improved control system), are able to switch from the RFP to the Tokamak configuration. On RFX-mod, the Tokamak operations gave successfull results, with the achievement of the H-mode regime and the creation of D-shaped plasmas (see Figure 1.8). This proves the flexibility of the machine also in the Tokamak configuration. As will be explained in the next section, the ability of operating in Tokamak configuration is fundamental for the main topic of this work, which is Plasma Position Reflectometry (PPR).

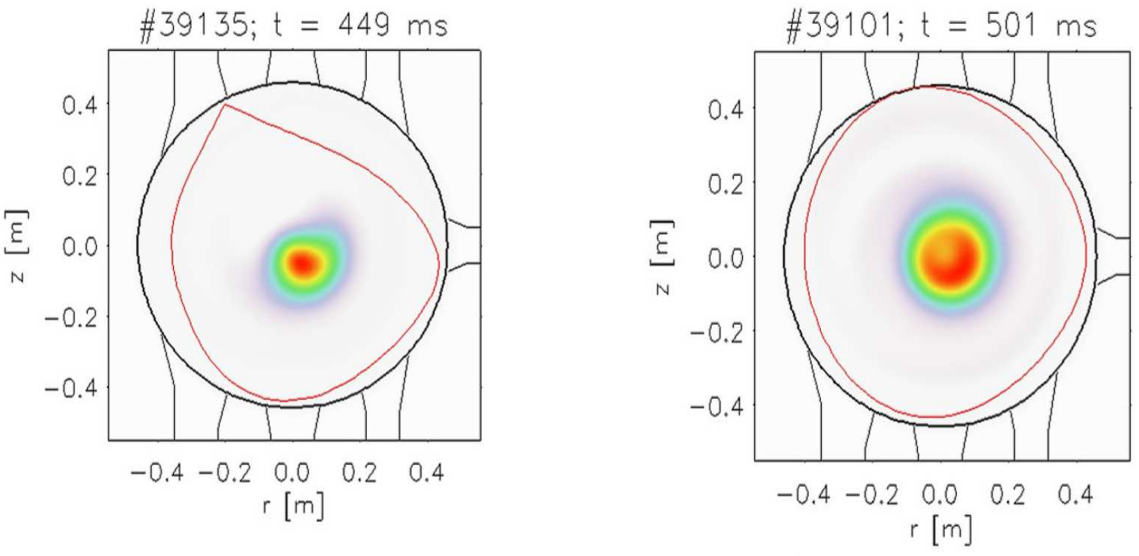

Figure 1.8: Example of a poloidal section of two D-shaped plasmas (red line is the Last Closed Flux Surface(LCFS)) obtained during RFX-mod's Tokamak operations

1.4 Microwave reflectometry in RFX: achievements and future perspectives

In fusion machines, the control of the plasma density (especially at the plasma edge) plays a crucial role. Some of the most successful and accurate methods to determine the latter quantity use electromagnetic waves as a probe into the plasma. Provided their intensity is not too high, such waves cause negligible perturbation to the plasma, but can give informations about the internal plasma properties with quite good spatial resolution. One of these methods is the microwave reflectometry, that basically consists in sending into the plasma an electromagnetic wave which will be reflected when some conditions in the plasma are met. If the reflected wave is detected, it is possible to use it to diagnose the plasma density at the reflection point. More details on the theoretical foundations of reflectometry will be given in chapter 2. Microwave reflectometry is, by now, a widely adopted technique for density profile reconstruction, due to its high temporal ($\sim \mu s$) and spatial ($\sim cm$) resolution. It has also been applied on the RFX-mod experiment, where an ultrafast reflectometric unit, which allowed to obtain a time resolution of 2 μs [9](needed because of the high level of fluctuations of the RFP configuration), was used. As an example of the successful application of reflectometry on the latter machine, Figure 1.9 shows a comparison between a reflectometric measurement and an edge Thomson scattering measurement on RFX-mod:

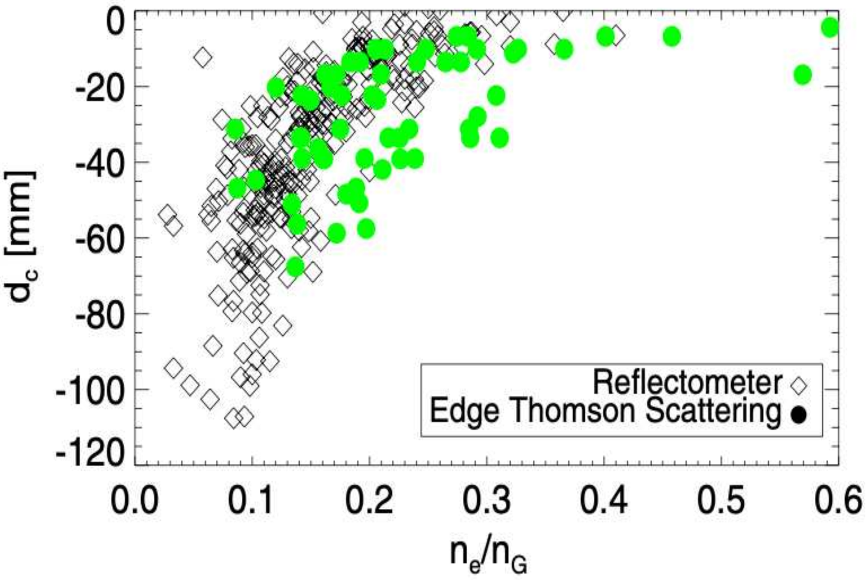

Figure 1.9: Comparison between reflectometric and Thomson scattering measurements of the distance of the cutoff layer of density 10^{19} m^{-3} from the first wall d_c, as a function of the ratio between the global density and the Greenwald density $\frac{n_e}{n_G}$[9]

The previous image shows that, especially at high global densities, the reflectometric measurement have a quite good agreement with the Thomson scattering measurements. On RFX-mod2, in addition to the same reflectometry system for density reconstruction of RFX-mod, a new reflectometric system for position control will be installed. Over the last years, indeed, reflectometry has also been proposed to complement magnetic diagnostics for position control, by placing a set of antennas at different poloidal positions in the same toroidal sector. Future reactors, indeed, will be characterized by high neutron fluxes and long pulse duration, so a plasma position control system which is entirely based on magnetic diagnostics is expected not to be feasible. More details about the application of reflectometry to plasma position control are given in 2.3. The most important upcoming machines where reflectometry is under consideration for position control are the Divertor Tokamak Test (DTT), under construction in Rome, and DEMO, the first reactor intended to demonstrate the feasibility of net energy production from fusion (see Figure 1.10 for a scheme of the lines of sight of DEMO's proposed reflectometer). Plasma Position Reflectometry (PPR) has already been successfully applied on the ASDEX-Upgrade machine for horizontal position control[10][11].

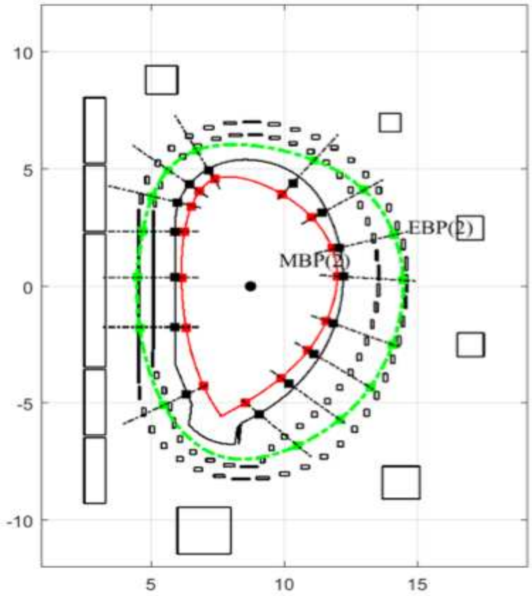

Figure 1.10: Antenna positions (black squares) and lines of sight (black dashed segments) of DEMO's proposed reflectometer [12]

For what concerns RFX-mod2's PPR, the novelty here is represented by the fact that, for the first time, it will be able to give both vertical and horizontal plasma position control. In particular, the diagnostic system will consist of four bistatic ultrafast independent reflectometric units working in the microwave frequency range (16–26.5 GHz) and installed in four different poloidal locations at the same toroidal angle: two on the equatorial plane (high field side/low field side) and two at the vertical top/bottom ports. Standard pyramidal horns will be installed in the external midplane and in the vertical ports, while parabolic hoghorn reflectors have been designed for the internal midplane. The experimental setup is illustrated in the following image:

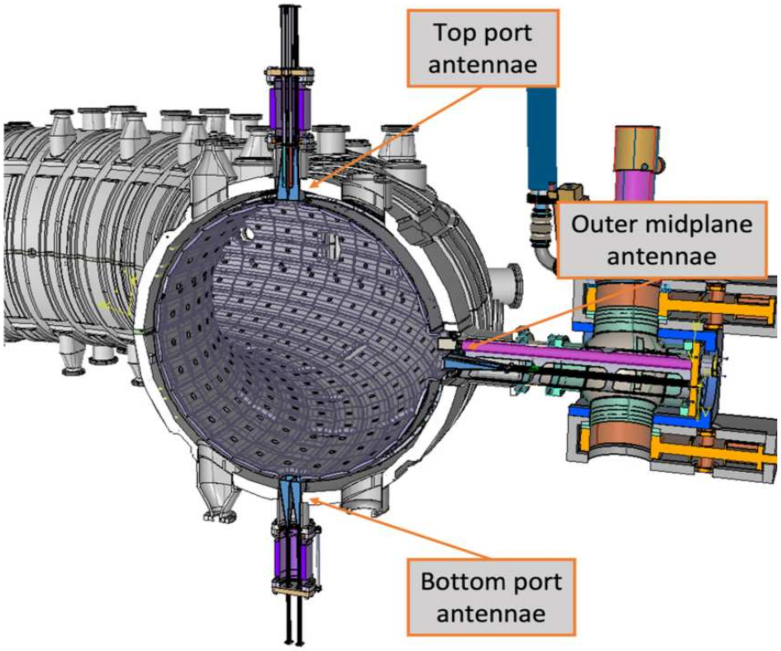

Figure 1.11: Sectional representation of RFX-Mod2's reflectometer [13]

In the next image, instead, the hoghorn antenna with his placement on the high field side of the machine is shown:

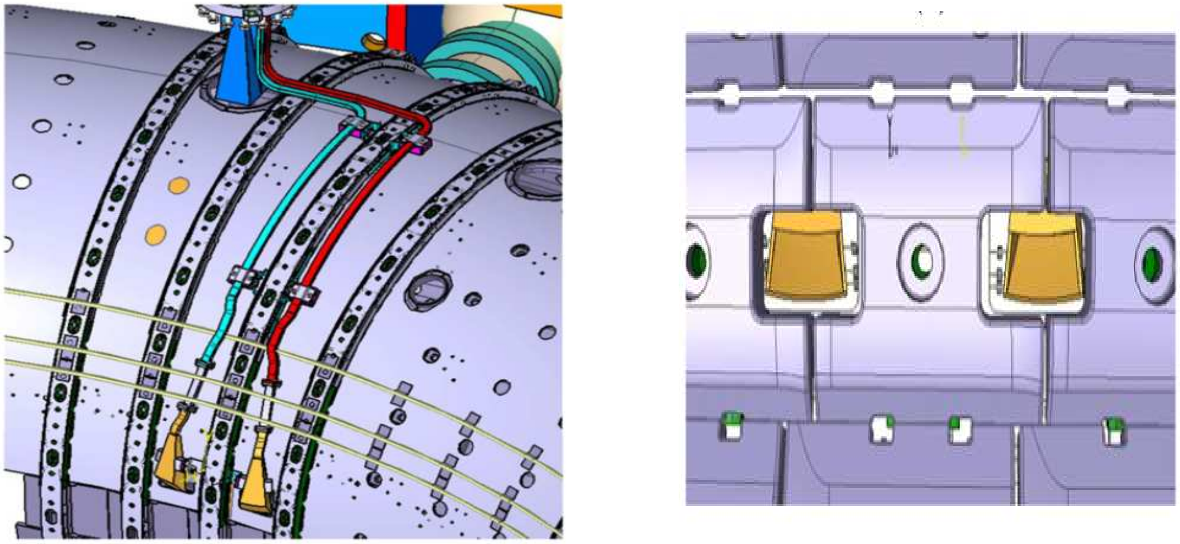

Figure 1.12: External(left) and internal (right) representation of high-field side's hoghorn antennas [13]

The design of the hoghorn antenna and of its waveguides was rather complicated, since they had to be adapted to the severe space constraints set by the diagnostic instrumentations already present on the RFX-mod2's high field side. This required a construction realized trough additive manufacturing for this antenna. Section 4.1 will be dedicated to a complete description of the experimental apparatus of the RFX-mod2's reflectometer. At this point, it is easy to understand why PPR works better in the Tokamak configuration. The typical axisymmetry of Tokamak plasmas, indeed, allows to fully characterize the plasma shape with a PPR positioned on one poloidal plane only.

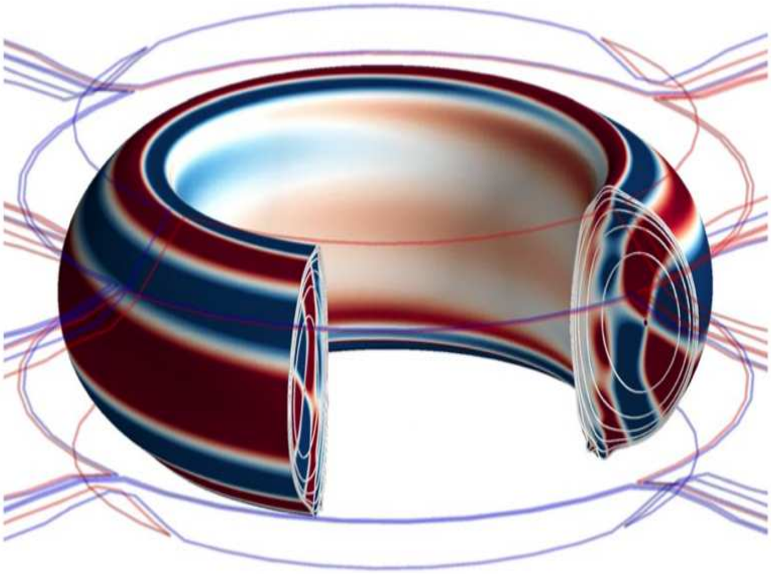

Figure 1.13: Pictorial representation of a typical Tokamak plasma'shape [14]

1.5 Aim and layout of the thesis

It is appropriate, now, to introduce the general aim and the structure of this work. This thesis is mainly concerned with the characterization of the above described antennas for the new RFX-mod2's reflectometer, through a comparison between theory, experimental measurements and simulated results. In particular, the focus is placed on the hoghorn antenna, due to its manufacturing process and geometry which make a performance investigation relevant for the fusion community. Finally, an additional experiment is performed, mimicking the plasma presence with a plane reflecting mirror, in order to verify if the hoghorn antenna is able to correctly predict the distance from the mirror. For what concerns the structure of this thesis, chapter 2 is dedicated to a theoretical introduction to reflectometry for density reconstruction and position control. Chapter 3, instead, is devoted to an introduction to antenna theory and modelling. In chapter 4 the experimental apparatus used in the antennas characterization process and in the measurements of the distance from the reflecting mirror is discussed. The results of this work, instead, are illustrated and commented in chapter 5. Finally, the conclusions of this thesis work are drawn in chapter 6.

Chapter 2

Basics of microwave reflectometry

In chapter 1, a short overview on microwave reflectometry was given. This chapter will be dedicated to a more quantitive description of the physical basics of reflectometry. In particular, in the first part of the chapter the theory of electromagnetic waves propagation in plasmas and its application to density profile measurements will be described. The final part of the chapter, instead, will focus on a more detailed discussion on PPR, explaining its main advantges and open problems.

2.1 Propagation of electromagnetic waves in plasmas

2.1.1 Waves in uniform media

The way waves propagate in magnetized plasmas is rather more complicated than the way they propagate in most other media, because the magnetic field causes the electrical properties of the plasma to be highly anisotropic. This is due to the difference in the electron dynamics between motions parallel and perpendicular to the magnetic field. For our purposes, plasma can be treated as a continuous medium in which current can flow, but that is otherwise governed by Maxwell's equations [15]:

$$\begin{aligned}
\nabla \cdot \mathbf{E} &= \frac{\rho}{\epsilon_0} \\
\nabla \cdot \mathbf{B} &= 0 \\
\nabla \times \mathbf{E} &= -\frac{\partial \mathbf{B}}{\partial t} \\
\nabla \times \mathbf{B} &= \mu_0 \mathbf{j} + \frac{1}{c^2}\frac{\partial \mathbf{E}}{\partial t}
\end{aligned} \tag{2.1}$$

Where $\mathbf{E}$ and $\mathbf{B}$ are respectively the electric field and the magnetic flux density, while ρ and $\mathbf{j}$ are the charge and current densities. $\mathbf{B}$ can now be eliminated by taking the curl of the third Maxwell's equation and the time derivative of the fourth one to get:

$$\nabla \times \nabla \times \mathbf{E} + \frac{\partial}{\partial t}\left(\mu_0 \mathbf{j} + \epsilon_0 \mu_0 \frac{\partial \mathbf{E}}{\partial t}\right) = 0 \tag{2.2}$$

At this point it is reasonable to suppose that the wave fields, which usually are written as perturbations to the equilibrium quantities, are small enough that the current is a linear functional of the electric field. Furthermore, plasma is considered to be homogeneous in space and time. Under these conditions the fields can be Fourier decomposed:

$$\mathbf{E}(\mathbf{x}, t) = \frac{1}{(2\pi)^4} \int \mathbf{E}(\mathbf{k}, \omega) e^{i(\mathbf{k}\cdot\mathbf{x} - \omega t)} d^3\mathbf{k} d\omega \tag{2.3}$$

In this way each Fourier mode satisfies Eq. (2.2) in the form:

$$\mathbf{k} \times \mathbf{k} \times \mathbf{E} + i\omega(\mu_0 \mathbf{j} - \epsilon_0 \mu_0 i\omega \mathbf{E}) = 0 \tag{2.4}$$

The assumption of linearity allows, for each mode, to write the relationship between current and electric field as:

$$\mathbf{j}(\mathbf{k}, \omega) = \boldsymbol{\sigma}(\mathbf{k}, \omega) \cdot \mathbf{E}(\mathbf{k}, \omega) \tag{2.5}$$

Thus, Eq. (2.4) becomes:

$$\mathbf{k} \times \mathbf{k} \times \mathbf{E} + i\omega(\mu_0 \boldsymbol{\sigma} \cdot \mathbf{E} - \epsilon_0 \mu_0 i\omega \mathbf{E}) = 0 \tag{2.6}$$

Which, noting that $\epsilon_0 \mu_0 = \frac{1}{c^2}$, can be written as:

$$(\mathbf{kk} - k^2 \mathbf{1} + \frac{\omega^2}{c^2} \boldsymbol{\epsilon}) \cdot \mathbf{E} = 0 \tag{2.7}$$

Where $(\mathbf{kk})_{ij} = k_i k_j$, and $\mathbf{1}$ is the 3x3 unit matrix. $\boldsymbol{\epsilon}$ is the dielectric tensor:

$$\boldsymbol{\epsilon} = \mathbf{1} + \frac{i}{\omega \epsilon_0} \boldsymbol{\sigma} \tag{2.8}$$

Eq. (2.7) contains three homogeneous simultaneous equations for the three components of $\mathbf{E}$. In order for these three equations to have a nonzero solution, the determinant of the matrix of the coefficients must be equal to zero:

$$det(\mathbf{kk} - k^2 \mathbf{1} + \frac{\omega^2}{c^2} \boldsymbol{\epsilon}) = 0 \tag{2.9}$$

This equation relates the $\mathbf{k}$ vector and the ω for different waves and is the dispersion relation. For any given wave vector $\mathbf{k}$ the latter determines the corresponding frequency or vice versa.

Mathematically, one may regard the propagation equation Eq. (2.7) as a matrix eigenvalue problem. The eigenvalue, making the determinant zero, provides the dispersion relation, while the eigenvector, which is the solution for **E** corresponding to a particular eigenvalue, determines the characteristic polarization of the wave with that **k** and ω. So far everything that has been said applies quite generally to any uniform linear medium in which electromagnetic waves may propagate. The above treatment shows that, in order to calculate the wave propagation properties in such a medium, a knowledge of the conductivity $\boldsymbol{\sigma}(\mathbf{k}, \omega)$ or, equivalently, the permittivity $\boldsymbol{\epsilon}(\mathbf{k}, \omega)$ is needed. The particular properties of plasmas as a media enter the treatment through their expressions for these quantities.

2.1.2 Plasma conductivity

The task is now to calculate the plasma conductivity and permittivity on the basis of an understanding of the nature of the plasma. This can be done at various levels of sophistication, from a kinetic-theory treatment down to a fluid treatment. The kinetic treatment incorporates details of the distribution function, whereas the simplest fluid treatment ignores all but the zeroth moment, the density. For the present purposes it turns out that the simplest of treatments is perfectly adequate, due to the fact that, for reflectometric applications, one is concerned with waves traveling at phase velocities close to the speed of light in plasmas whose thermal electron speed is $v_{e,t} << c$. Thermal particles motions can, therefore, be ignored and the so-called cold plasma approximation can be adopted. In the cold plasma approximation, electrons are taken to be at rest, except for the motions induced by the wave presence. Ions instead, due to their larger mass, are always considered at rest. To obtain $\boldsymbol{\sigma}$, the current induced by a specific electric field on the electrons has to be computed. To do that, it is convenient to start from the well-known expression of the Lorentz force on a single electron:

$$m_e \frac{\partial \mathbf{v}}{\partial t} = -e(\mathbf{E} + \mathbf{v} \times \mathbf{B}) \tag{2.10}$$

Since a perturbative analysis will be performed, each quantity can be written as the sum of an equilibrium value, indicated with the subscript 0, and a perturbation to that value caused by the wave presence, indicated with the subscript 1. Considering that in the cold plasma approximation the equilibrium electron velocity is zero, and linearizing the equation at first order:

$$m_e \frac{\partial \mathbf{v}_1}{\partial t} = -e(\mathbf{E}_1 + \mathbf{v}_1 \times \mathbf{B}_0) \tag{2.11}$$

Where a null equilibrium electric field and a static equilibrium magnetic field $\mathbf{B}_0$ (magnetized plasma) were considered. Furthermore, in this approximations, collisions between plasma particles will be ignored. For a single Fourier mode, the perturbations can be taken to be proportional to $e^{-i\omega t}$. Taking the z-axis parallel to $\mathbf{B}_0$ the three components of Eq. (2.11) can be written as:

$$\begin{aligned} -m_e i\omega v_x &= -eE_x - eB_0 v_y \\ -m_e i\omega v_y &= -eE_y + eB_0 v_x \\ -m_e i\omega v_z &= -eE_z \end{aligned} \tag{2.12}$$

At this point it is easy to solve for the three components of $\mathbf{v}$ to get:

$$\begin{aligned} v_x &= \frac{-ie}{m_e\omega}\frac{1}{1-\frac{\Omega^2}{\omega^2}}(E_x - i\frac{\Omega}{\omega}E_y) \\ v_y &= \frac{-ie}{m_e\omega}\frac{1}{1-\frac{\Omega^2}{\omega^2}}(E_y + i\frac{\Omega}{\omega}E_x) \\ v_z &= \frac{-ie}{\omega m_e}E_z \end{aligned} \tag{2.13}$$

Where $\Omega = \frac{eB_0}{m_e}$ is the electron cyclotron frequency. In this cold plasma approximation all electrons move alike and so the current density is simply:

$$\mathbf{j} = -en_e\mathbf{v} = \boldsymbol{\sigma}\cdot\mathbf{E} \tag{2.14}$$

With:

$$\boldsymbol{\sigma} = \frac{in_e e^2}{m_e\omega}\cdot\frac{1}{1-\frac{\Omega^2}{2}}\begin{bmatrix} 1 & \frac{-i\Omega}{\omega} & 0 \\ \frac{+i\Omega}{\omega} & 1 & 0 \\ 0 & 0 & 1-\frac{\Omega^2}{\omega^2} \end{bmatrix} \tag{2.15}$$

One can now write $\boldsymbol{\epsilon}$ from Eq. (2.8) and write the dispersion relation Eq. (2.9). To do that, it is convenient to choose axes such that $k_x = 0$, in order to have only the angle θ of $\mathbf{k}$ with respect to the direction of $\mathbf{B}_0$ as parameter. This means:

$$\mathbf{k} = k(0, sin(\theta), cos(\theta)) \tag{2.16}$$

It is now useful to introduce the following parameters:

$$\begin{aligned} X &= \frac{\omega_p^2}{\omega^2} \\ Y &= \frac{\Omega}{\omega} \\ N &= \frac{kc}{\omega} \end{aligned} \tag{2.17}$$

Clearly, the parameter N is the refractive index of the plasma, which is a fundamental parameter with respect to electromagnetic properties. After some computations, it can now be proved that Eq. 2.9 reads:

$$det\begin{bmatrix} -N^2+1-\frac{X}{1-Y^2} & \frac{iXY}{1-Y^2} & 0 \\ \frac{-iXY}{1-Y^2} & -N^2\cos^2\theta+1-\frac{X}{1-Y^2} & N^2\sin\theta\cos\theta \\ 0 & N^2\sin\theta\cos\theta & -N^2\sin^2\theta+1-X \end{bmatrix}=0 \tag{2.18}$$

Since the algebra to solve the latter is heavy, the final solution is reported:

$$N^2=1-\frac{X(1-X)}{1-X-\frac{1}{2}Y^2\sin^2\theta\pm[(\frac{1}{2}Y^2\sin^2\theta)^2+(1-X)^2Y^2\cos^2\theta]^{\frac{1}{2}}} \tag{2.19}$$

Where θ is the angle between the wave vector $\mathbf{k}$ and $\mathbf{B}_0$. This equation is basically the dispersion relation for waves propagating in a cold magnetized plasma and it is called Appleton-Hartree formula. Two fundamental propagation states can be distinguished:

- **Parallel propagation** ($\theta=0$): in this case Eq.(2.19) reduces to:

  $$N^2=1-\frac{X}{1-Y^2}\pm\frac{XY}{1-Y^2} \tag{2.20}$$

  for which the characteristic polarization of the wave electric field is:

  $$\begin{gathered}\frac{E_x}{E_y}=\pm i\\ E_z=0\end{gathered} \tag{2.21}$$

  Two waves belong to this mode, both propagating parallel to the magnetic field and which are respectively right and left circularly polarized on the plane perpendicular to $\mathbf{B}_0$.

- **Perpendicular propagation** ($\theta=\frac{\pi}{2}$): from Eq. (2.19) it is easy to see that also in this case two different modes are present, the first one being called the Ordinary Mode (O-Mode), and having the following dispersion relation:

  $$N^2=1-X \tag{2.22}$$

  With a polarization given by:

  $$E_x=E_y=0 \tag{2.23}$$

  So this mode is characterized by an electric field oscillating parallel to $\mathbf{B}_0$, implying that electron motions induced by the wave presence won't be influenced by the magnetic field of the plasma. That is why the dispersion relation of the O-Mode is the same dispersion relation of a unmagnetized plasma with $\mathbf{B}_0 = 0$. The other mode which characterizes the perpendicular propagation is the one obtained taking the minus sign in Eq. (2.19) and it is called the Extraordinary Mode (X-Mode). It has a dispersion relation given by:

$$N^2 = 1 - \frac{X(1-X)}{1-X-Y^2} \tag{2.24}$$

With polarization given by:

$$\begin{aligned} \frac{E_x}{E_y} &= -i \cdot \frac{1-X-Y^2}{XY} \\ E_z &= 0 \end{aligned} \tag{2.25}$$

So this mode has a a field which oscillates perpendicular to $\mathbf{B}_0$, making the dispersion relation dependent on the the magnetic field.

2.1.3 Non uniform media: WKBJ approximation

Naturally, no practical plasma or any other medium satisfies the condition of being uniform throughout all space. It is important to consider, then, what happens when there are spatial gradients in the electromagnetic properties. Mathematically, the results are that the fields of the form exp $e^{i(\mathbf{k}\cdot\mathbf{x}-\omega t)}$ no longer separately satisfy Maxwell's equations. One can still express any solution as a sum of such Fourier modes, but these will, in general, be coupled together by the nonuniformities of the medium. If the properties of the plasma vary sufficiently slowly, then locally the wave can be thought of as propagating in an approximately uniform medium and, hence, behaving as if all the previous treatment applied. Thus, for any frequency and propagation direction, there is locally a well defined k and refractive index N corresponding to the local values of the plasma parameters. In this context the WKBJ approach, also called geometric optics approximation, plays an important role. Basically, it consists in assuming that the wave propagates as a ray, which locally behaves as a wave propagating in an homogeneous medium with the same local properties. The field is assumed to have the form:

$$E \sim \exp\left(i \int \mathbf{k} \cdot \mathbf{dl} - \omega t\right) \tag{2.26}$$

where l is the distance along the ray path and k is the solution of the homogeneous plasma dispersion relation for the given ω, based on the local plasma parameters. This will be a good approximate solution provided that the fractional variation of k in one wavelength of the wave is small:

$$\frac{|\nabla k|}{k^2} \ll 1 \tag{2.27}$$

In this case the coupling to other waves is small and may generally be ignored as far as the single transmitted wave is concerned. For the purposes of this work, it is sufficient to note that the phase of the emerging wave is given by $\int \mathbf{k} \cdot \mathbf{dl}$, which may be written as $\int \frac{\omega}{c} N dl$ provided the ray direction and k approximately coincide (for example if the plasma is approximately isotropic). From here on, reflectometry will be described using the latter approximation.

2.2 Reflectometry

2.2.1 Principle of measurements

When a wave of a certain frequency propagates through a plasma with increasing density in the direction of propagation, it may arrive at a point where the electron density equals the so-called cutoff density n_c. The cutoff density is the density above which the refractive index N^2 goes negative. From the definition of N, this would clearly imply that $\mathbf{k}$ should have an imaginary component, making the wave evanescent. Therefore, what will happen is that the wave will be reflected from the cutoff point and will propagate out of the plasma. Detecting the reflected wave, it is possible to use it to diagnose the plasma density at the cutoff point. This is the conceptual foundation of reflectometry. Of course, the relation which relates the frequency or wavevector of the input wave to the cutoff density at which the latter will be reflected depends on the propagation mode of the input wave. For RFX-mod2, the frequency range of the PPR ($17 - 26.5$ GHz) has been chosen to exploit the upper X-Mode cutoff frequency [13], which using Eq. (2.24) can be put in the form :

$$\omega_{uxc} = \frac{1}{2}(\Omega + \sqrt{\Omega^2 + 4\omega_p^2}) \tag{2.28}$$

However, for an analytical description of reflectometry, it is convienent to use the O-Mode cutoff frequency, given by:

$$\omega_{oc} = \omega_p = \sqrt{\frac{n_{e,oc} e^2}{\epsilon_0 m_e}} \tag{2.29}$$

A one-dimensional model will be now used to illustrate how to measure density profiles with reflectometry. The starting point consists in considering a one-dimensional plasma slab model in which the electron density n_e varies with position x giving rise to a plasma frequency that is a function of the position $\omega_p(x)$.

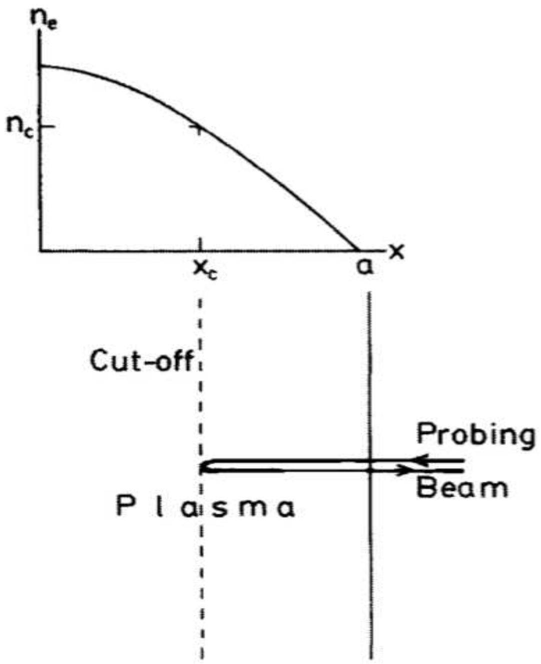

Figure 2.1: Schematic representation of the 1d plasma slab model [16]

The WKBJ form of the phase difference between two arbitrary points within the plasma, A and B is then:

$$\phi(A) - \phi(B) = \frac{\omega}{c}\int_A^B N dx \tag{2.30}$$

Near the reflection point, i.e. $N = 0$,the usual conditions for the applicability of the WKBJ approximation breaks down because $k \to 0$. However, it can be shown that, provided the density gradient can be taken as uniform in the region of reflection, the phase difference at position a between forward and reflected waves can be written[17]:

$$\phi = \frac{2\omega}{c}\int_{x_c}^{a} N dx - \frac{\pi}{2} \tag{2.31}$$

This equation basically states that the phase delay is just what would be obtained from simple-minded application of the WKBJ approach, regarding the cutoff layer as a mirror, except that an additional $\frac{\pi}{2}$ phase change at reflection must be included. Identifying a as the edge of the plasma, where the wave is launched, and recalling that the refractive index is a function of density and possibly magnetic field, it is clear that ϕ is determined, via Eq. (2.30), by an integral of n_e from the plasma edge to the cutoff point. This is the main limitation of single frequency reflectometry, i.e. the fact that only the integral of the density over a portion of the plasma can be determined. If, however, one wishes to deduce a complete density profile rather than just an average density, it is necessary to use a range of probing frequencies. To illustrate why the latter is necessary, it is sufficient to substitute Eq. (2.22) into Eq. (2.31) and to differentiate with respect to ω. Expressing the result in terms of the vacuum wavelength $\lambda = \frac{2\pi c}{\omega}$ as the integration variable leads, after some algebra, to:

$$\frac{d\phi}{d\omega} = 2\int_{\lambda}^{\infty} \frac{1}{c}\frac{dx_c}{d\lambda_p}\frac{\lambda_p d\lambda_p}{(\lambda_p^2 - \lambda^2)^{\frac{1}{2}}} \tag{2.32}$$

where $\lambda_p = \frac{2\pi c}{\omega_p}$. To go on, it is now appropriate to introduce the the Abel Inversion[18], which allows to deduce the local distribution of a given quantity from measurements of its integral. As an example, it is convenient to consider a cylindrically symmetric plasma in which a given quantity $f(r)$, with the same symmetry, has only chord integrals as accessible measurements. The system is illustrated in the following figure:

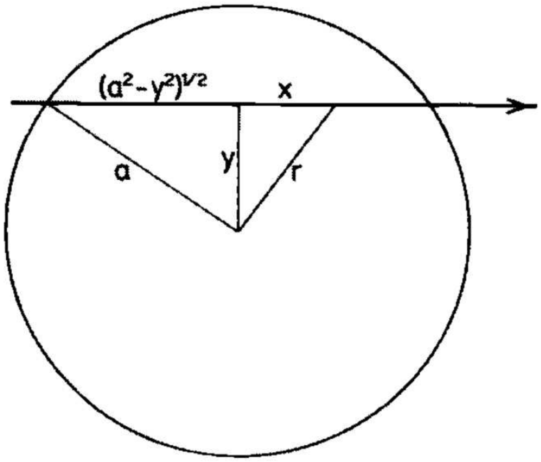

Figure 2.2: Chord integral on a cylindrically symmetric plasma [16]

The accessible chord integral can be written as:

$$F(y) = \int_{-\sqrt{a^2-y^2}}^{\sqrt{a^2-y^2}} f(r)dx \tag{2.33}$$

At this point, changing the integration variable to r easily leads to:

$$F(y) = 2\int_{y}^{a} f(r)\frac{rdr}{\sqrt{r^2-y^2}} \tag{2.34}$$

This relationship between F and f is an integral equation for F, first studied by the mathematician Abel in the nineteenth century. Abel showed that the following inverse transform, relating $f(r)$ and an integral of F, holds:

$$f(r) = -\frac{1}{\pi}\int_r^a \frac{dF}{dy}\frac{dy}{\sqrt{y^2 - r^2}} \tag{2.35}$$

provided that $f(a) = 0$. Therefore, a simple expression useful to obtain the radial profile of f from measurements of its chord integral has been derived. This process is often called Abel inversion, and it finds an application in our case for Eq. (2.32). Abel inversion can be applied here with the identifications:

$$\begin{aligned} \frac{d\phi}{d\omega} &\to F(y) \\ \frac{1}{c}\frac{dx_c}{d\lambda_p} &\to f(r) \\ \lambda &\to y \\ \lambda_p &\to r \end{aligned} \tag{2.36}$$

After some algebra, substitution into Eq.(2.35) gives:

$$x_c(\omega) = a - \frac{c}{\pi}\int_0^\omega \frac{d\phi}{d\omega'}\frac{d\omega'}{\sqrt{\omega^2 - \omega'^2}} \tag{2.37}$$

The position of the cutoff $x_c(\omega)$ can, therefore, be deduced, provided the derivative of the phase delay with respect to the angular frequency is known for all the angular frequencies less than ω. The latter is nothing else that the group delay τ_g, i.e. the round-trip time it would take a pulse to propagate out to the reflection layer and back:

$$\tau_g = \frac{\partial\phi}{\partial\omega} \tag{2.38}$$

This was, basically, the theoretical background behind reflectometric measeurements. Eq. (2.37) proves how to infer the cutoff position; subsequently the plasma density at the cutoff point can be computed by inverting Eq. (2.29) for O-mode propagation or Eq. (2.28) for X-mode propagation. This, in principle, enables to reconstruct the density profile of the plasma. The fundamental point is , however, how to estimate the derivative of the phase delay with respect to the angular frequency. This will be explained below.

2.2.2 Frequency Modulated Continous Wave (FM-CW) method for time delay estimation

In order to derive the derivative of the phase delay, the most adopted scheme in reflectometry is the so-called Frequency Modulated Continous Wave (FM-CW) method. This will also be the scheme abtopted by the RFX-mod2's reflectometer. In an FM-CW broadband microwave reflectometer, a density range $[n_{e1}, n_{e2}]$ is scanned by continously modulating a microwave source to produce a probing chirp with a frequency range $[F_1, F_2]$. In RFX-mod2 $F_1 = 16$ Ghz and $F_2 = 26.5$ Ghz. A schematic illustration of the FM-CW RFX-mod2 reflectometer electronics is shown in the following picture:

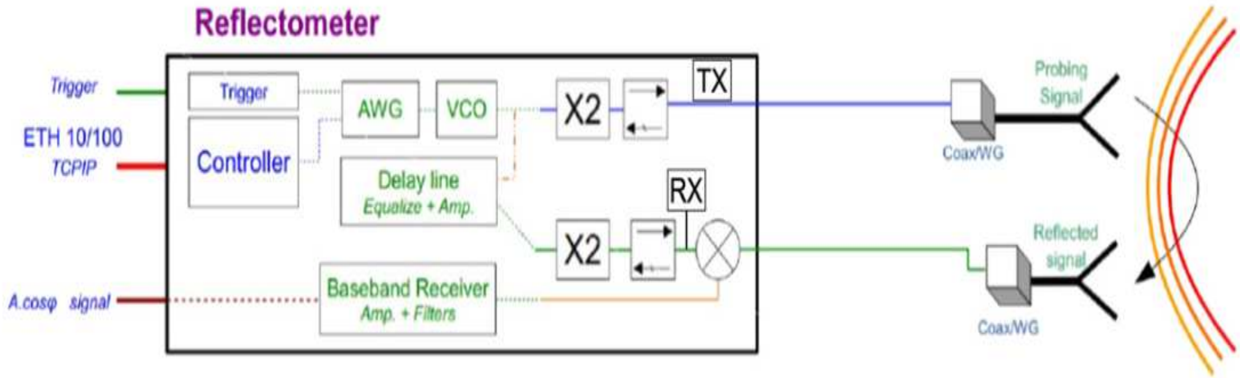

Figure 2.3: Scheme of the electronics of the RFX-mod2's reflectometer [13]

The frequency sweep is generated through a *Voltage Controlled Oscillator*(VCO) and a frequency multiplier , whose probing signal (TX) can be written as:

$$s_{TX}(t) = a_{TX} \cos(\theta(t)) \tag{2.39}$$

Assuming that the VCO is able to perform a linear sweep between F_1 and F_2, the probing frequency reads:

$$f_{TX}(t) = \frac{1}{2\pi}\frac{d\theta}{dt} = F_1 + \frac{F_2 - F_1}{T_{sw}} t \tag{2.40}$$

Where T_{sw} is the sweep duration. $\theta(t)$ can, thus, be written as:

$$\theta(t) = 2\pi F_1 t + \pi k_{sw} t^2 \tag{2.41}$$

Where:

$$k_{sw} = \frac{F_2 - F_1}{2T_{sw}} \tag{2.42}$$

Since RFX-mod2's reflectometer works using the so-called *homodyne detection scheme*[19], a copy of the TX signal is used as reference signal (i.e. as a Local Oscillator (LO)). The TX signal will, thus, be reflected from the plasma, providing the RX signal $s_{RX}(t)$:

$$s_{RX}(t) = a_{RX} \cos(\theta(t - \tau_g(t))) \tag{2.43}$$

Where τ_g is the delay time of s_{RX} with respect to s_{TX} (see Eq. (2.38)). The two signals s_{RX} and s_{TX}, in RFX-mod2, are mixed using a square-law mixer . The RX-LO signal will, thus, read:

$$\begin{aligned} s_m(t) &= (s_{TX}(t) + s_{RX}(t))^2 \\ &= a_{TX}^2 \cos^2(\theta(t)) + a_{RX}^2 \cos^2(\theta(t) - \tau_g(t)) + 2a_{TX}a_{RX} \cos\theta(t) \cos(\theta(t) - \tau_g(t)) \end{aligned} \tag{2.44}$$

The latter signal is eventually passed through a baseband receiver, which extracts the following low frequency component:

$$s_b(t) = \frac{a_{TX}^2 + a_{RX}^2}{2} + A(t)\cos(\phi(t)) \tag{2.45}$$

Where $A(t) = a_p(t)a_r(t)$ is a low frequency component and $\phi(t)$ is the phase shift of the reflected wave with respect to the local oscillator:

$$\begin{aligned} \phi(t) &= \theta(t) - \theta(t - \tau_g(t))) \\ &= 2\pi\tau_g(t)(F_1 + k_{sw}t) - \pi k_{sw}\tau_g^2(t) \end{aligned} \tag{2.46}$$

At this point, $A(t)$ and $\phi(t)$ can be extracted from the signal and its beating frequency can be estimated:

$$f_b = \frac{1}{2\pi}\frac{\partial\phi}{\partial t} = f_p(t)\frac{\partial\tau_g}{\partial t} + k_{sw}\tau_g(t)\left(1 - \frac{\partial\tau_g}{\partial t}\right) \tag{2.47}$$

Which, for typical values of $f_b(t)$ and $\frac{\partial\tau_g}{\partial t}$ can be approximated as:

$$f_b(t) \simeq k_{sw}\tau_g(t) \tag{2.48}$$

Where $k_{sw} = \frac{df_p}{dt}$ is the sweeping rate of the probing waves. This result agrees with [20]. The latter equation enables to obtain $\tau_g(t)$, i.e. the phase delay needed for the calculation of the cutoff position $x_c(\omega)$. From the cutoff position, the density at the cutoff is reconstructed by inverting, depending on the mode of propagation, Eq. (2.28) or Eq. (2.29). In this way the plasma density profile can be reconstructed. Of course, it is necessary to say that the sweep duration T_{sw} has to be adjusted in such a way that during a sweep the plasma could be considered as "frozen". If τ_p indicate the characteristic time during which plasma profile evolves, the latter condition reads:

$$T_{sw} << \tau_p \tag{2.49}$$

In particular , for RFX-mod2 it will be $T_{sw} \sim \mu s$ [13].

2.3 Plasma position reflectometry (PPR)

Until now, in this chapter, the theoretical basics of reflectometry were illustrated and the method to obtain the plasma density profile from a reflectometric measurement was described. The derivation of the plasma density profile is, by far, the most common application for which reflectometry has been extensively used until now in fusion machines. As already anticipated in 1.4, however, in last years reflectometry has been proposed to complement magnetic diagnostics for position control. Future fusion machines (such as DTT and DEMO), indeed, will be characterized by an ever increasing pulse duration and neutron flux. These two features are expected to be responsible of a dramatic deterioration of the signal coming from in-vessel magnetic diagnostics (which are, nowadays, the most adopted diagnostic for plasma position control). Magnetic diagnostics, indeed, are composed by a coil connected to an integrator circuit, which measures the magnetic field at the coil position. From the knowledge of the magnetic field at different poloidal positions the LCFS, which defines the plasma border, is then reconstructed by applying MHD equilibrium numerical algorithmes. The integrator signal may, thus, be drifted by long pulse duration, while undesired voltages may be induced by the high neutron radiation. As a consequence of the latter facts, Plasma Position Reflectometry (PPR) is acquiring importance in the scientific community. A PPR system should be composed of a set of antennas poloidally distributed on different positions, in the same toroidal sector (as shown in Figure 1.10). Despite PPR could seem a convenient and effective method to real-time control plasma position, still many problems remain with this method. The key challenge on PPR, indeed, lies in the reconstruction of the LCFS position on each line of sight. As said in 1.4, in ASDEX-Upgrade the LCFS was reconstructed with the help of interferometric diagnostics and of a neural network based algorithm. A risolutive and independent scheme, however, is still missing, while algorithms to reconstruct the LCFS once its position is known on each line of sight are already been preliminary obtained [12] (see Figure 2.4).

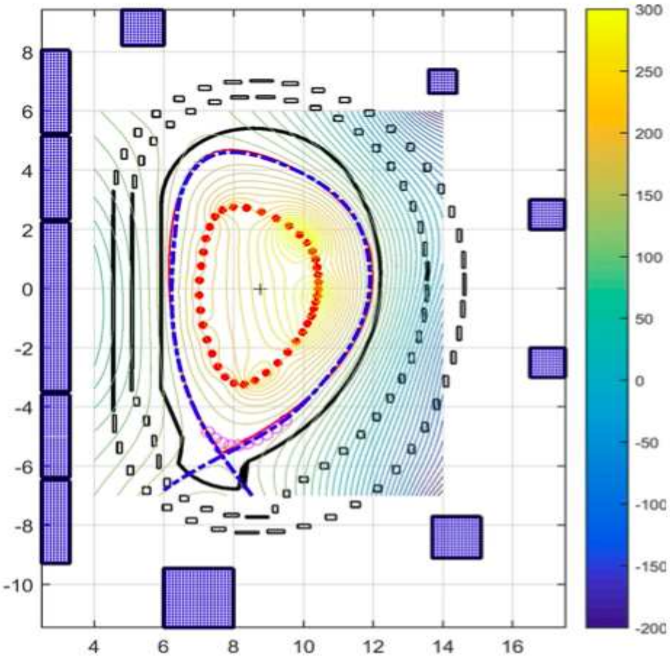

Figure 2.4: Reconstruction of the LCFS (blue line) on an expected DEMO plasma [12]

Another criticality of PPR is represented by the possible performance downgrade of the antennas when curvatures of the reflecting plasma surfaces (which approximately follow the shape of magnetic surfaces) are present. ASDEX-Upgrade's application of PPR, indeed, was characterized by lines of sight which were perpendicular to the magnetic surfaces, while simulations on curved surfaces showed a possible deterioration of the performances [21]. The latter open problems, together with the relevance of plasma position control in future fusion machines and of the PPR's possibilities in this sense, contribute to make the application of PPR on RFX-mod2 of great importance for the scientifc community.

Chapter 3

Basics of Antenna Theory and modelling

In this chapter a basic introduction to antenna theory and antenna modelling will be provided. Firstly, the definition of antenna and of the fundamental antenna parameters and radiation regions will be given. Subsequently, a theoretical derivation of the far-field radiation of the pyramidal and of the hoghorn antennas will be performed. The chapter will be concluded with an introduction to the numerical modelling methods used to simulate the fields around the antennas.

3.1 Basics of Antenna Theory

As anticipated, this section will be dedicated to an introduction to the fundamentals of antenna theory. First of all, an overview of the most important antenna parameters is presented. Subsequently, a theoretical derivation of the fields diffused by aperture antennas is briefly illustrated. Before going into the details of antenna theory, however, it is convenient to define what an antenna is. An antenna is defined by Webster's Dictionary [22] as "a usually metallic device (as a rod or wire) for radiating or receiving radio waves." In other words the antenna is the transitional structure between free-space and a guiding device, as shown in Figure 3.1:

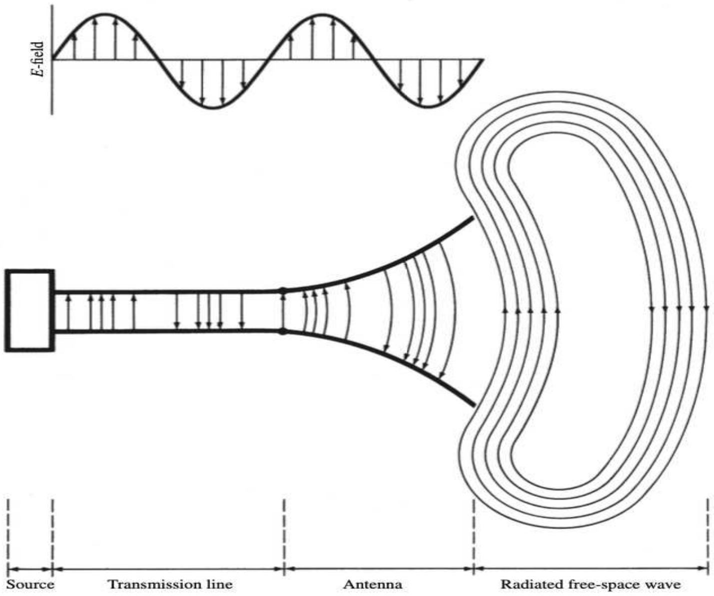

Figure 3.1: Scheme of an antenna, from [23]

For the purposes of this work, the guiding device or transmission line takes the form of a waveguide, and it is used to transport electromagnetic energy from the transmitting source to the antenna, or from the antenna to the receiver. In the former case, the antenna is called “transmitting antenna” and in the latter the antenna is called “receiving antenna”. The source, instead, will be a reflectometric unit (which will be illustrated in Chapter 5). There are many categories of antennas, but the most relevant for this thesis are the aperture antennas, which are antennas having some sort of opening through which electromagnetic waves are transmitted or received. As already anticipated in the previous section the antennas which will be installed on RFX-mod2 are of two kinds: pyramidal horn and hogghorn. Both will be described in the following.

3.1.1 Antennas radiation

It has been said above that, basically, antennas diffuse in outer space some radiation that, for the cases relevant to this work, comes from wave guides. So, to properly describe and characterize antennas, some mathematical quantities that describe the radiation diffused by these kind of objects have to be introduced. As it is known from electromagnetic theory, radiation basically consists of an oscillation of electric and magnetic fields, whose evolution is governed by Maxwell’s equations Eqs. (2.1). The fields **E** and **B** are, thus, the two basic quantities from which all the features of the radiation coming out from an antenna can be derived. For the moment these field will be considered known in all space and at all times. Only later on in this chapter the method used to compute the radiated fields, starting from the knowledge of the oscillation mode propagating into the waveguide, will be described.

3.1.2 Radiation power density

The first quantity, which can be associated with antennas radiation, that will be presented is its power density. It is known that electromagnetic waves are used to transport information through a wireless medium or a guiding structure, from one point to the other. It is then natural to assume that power and energy are associated with electromagnetic fields. The quantity used to describe the power associated with an electromagnetic wave is the instantaneous Poynting vector defined as:

$$\mathbf{S} = \mathbf{E} \times \mathbf{H} \tag{3.1}$$

Where **H** is the magnetic field intensity and is expressed as the difference between the magnetic flux density and the magnetization induced in matter by its presence [15]:

$$\mathbf{H} = \frac{\mathbf{B}}{\mu_0} - \mathbf{M} \tag{3.2}$$

In free space, of course, **M** is zero and **B** and **H** are proportional to each other. Poynting vector represents the power flow per unit area (i.e. the power density) of the electromagnetic wave in a specific point of space. In this work time varying fields will be treated, so it is useful to work in the frequency domain and use the average Poynting vector, integrating it over a period of oscillation. Fields are, thus, expressed in complex notation as:

$$\begin{aligned} \mathbf{E} &= Re[\boldsymbol{E} e^{j\omega t}] \\ \mathbf{H} &= Re[\boldsymbol{H} e^{j\omega t}] \end{aligned} \tag{3.3}$$

Where $\boldsymbol{E}$ and $\boldsymbol{H}$ are, in general, complex vectors. Using Eqs. (2.4) and the identity $Re[\boldsymbol{E} e^{j\omega t}] = \frac{1}{2}[\boldsymbol{E} e^{j\omega t} + \boldsymbol{E}^* e^{-j\omega t}]$, it is easy to prove that:

$$\mathbf{S} = \frac{1}{2} Re[\boldsymbol{E} \times \boldsymbol{H}] + \frac{1}{2} Re[\boldsymbol{E} \times \boldsymbol{H} e^{2j\omega t}] \tag{3.4}$$

Taking the time average one gets:

$$\mathbf{W}_{rad} =< \mathbf{S} >= \frac{1}{2} Re[\boldsymbol{E} \times \boldsymbol{H}] \tag{3.5}$$

Which is the radiation power density of the electromagnetic radiation exiting the antenna aperture. At this point it is easy to calculate the power radiated by the antenna P_{rad} through a simple integration of the latter over a closed surface:

$$P_{rad} = \iint_S \mathbf{W}_{rad} \cdot dS \tag{3.6}$$

Due to energy conservation the previous integral has to be, of course, independent of the chosen closed surface, as long as it contains the antenna. For simplicity reasons, from now on, $\mathbf{E}$ and $\mathbf{B}$ (and not $\boldsymbol{E}$ and $\boldsymbol{B}$) will indicate the whole complex vector. It is implicit that in order to compare with measurements one has to take the real part of each quantity.

3.1.3 Beamwidth

Associated with the pattern of an antenna is a parameter designated as beamwidth. The beamwidth of a pattern is defined as the angular separation between two identical points on opposite side of the pattern maximum. In an antenna pattern, there are a number of beamwidths. One of the most widely used beamwidths is the *Half-Power Beamwidth* (HPBW), which is defined as the angle between the two directions in which the radiation intensity is one-half value of the beam, in a plane containing the direction of the maximum of a beam. This is show in the figure below:

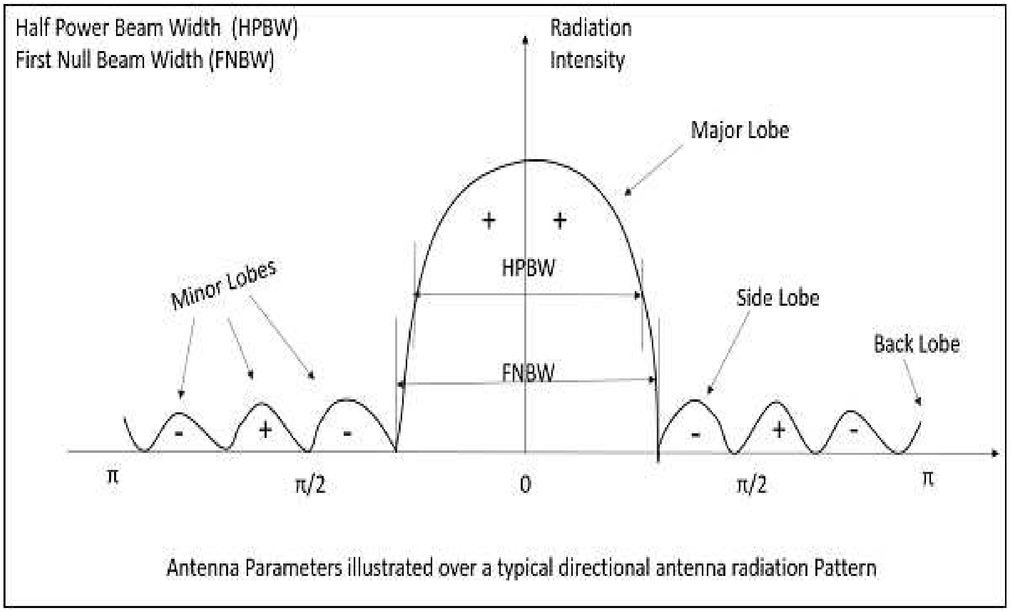

Figure 3.2: Illustration of HPBW and FNBW of a radiation pattern [24]

In particular, in this work, radiation power will be measured in dBm, defined as follows:

$$P_{rad}[dBm] = 10 \cdot \log_{10} P_{rad}[mW] \tag{3.7}$$

In this unit, the HPBW corresponds to the angle between the two directions in which radiation intensity is -3 dBm with respect to the beam maximum. Another important beamwidth is the angular separation between the first nulls of the pattern, and it is referred to as the First-Null Beamwidth (FNBW). However, in practice, the term beamwidth (if no other identification is reported) usually refers to the HPBW. The beamwidth of an antenna is a very important figure of merit and often it is used to quantify how much the antenna main lobe is extended from an angular point of view.

3.1.4 Radiation intensity and directivity

In the far-field region outside the antenna, that will be introduced in the following, the radiation intensity U can be defined as:

$$U(\theta, \phi) = r^2 \cdot W_{rad}(\theta, \phi) \tag{3.8}$$

where r is the distance from the origin of the coordinate systems, usually taken to be coinciding with the center of the antenna aperture. θ and ϕ, instead, are the spherical coordinates, which indicate the direction from the origin of the coordinate system to the observation point. The radiation intensity represents the power radiated by an antenna per unit solid angle. It follows that:

$$P_{rad} = \iint_{4\pi} U d\Omega \tag{3.9}$$

Considering an isotropic source which has a uniform intensity U_0, the following equation holds:

$$U_0 = \frac{P_{rad}}{4\pi} \tag{3.10}$$

From the radiation intensity it is natural to introduce the directivity. The directivity D of an antenna, in a given direction, is defined as the ratio between the intensity in that direction and the intensity of a uniform emitter. This means that:

$$D(\theta, \phi) = \frac{U(\theta, \phi)}{U_0} = \frac{4\pi U(\theta, \phi)}{P_{rad}} \tag{3.11}$$

If the direction is not specified, usually what is meant by directivity is the maximum directivity, i.e. the directivity in the direction where the intensity is maximum:

$$D_{max} = \frac{U_{max}}{U_0} = \frac{4\pi U_{max}}{P_{rad}} \tag{3.12}$$

It is then clear from the previous definitions that directivity measures the ability of the antenna to focus the radiation power in a restricted portion of space. So a high directivity is usually desired.

3.1.5 Radiation regions

Until now some parameters and physical quantities needed to describe radiation have been introduced. It is appropriate, at this point, to describe how the radiation emitted by an antenna is usually structured. The space around an antenna can be divided into three fundamental regions where the radiation has different characteristics, as pictured in 3.3:

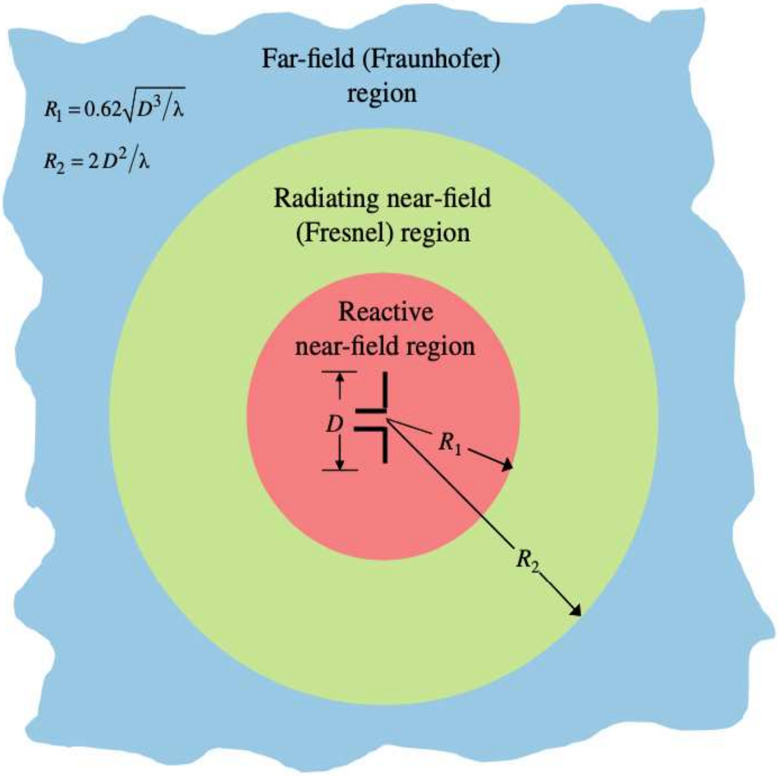

Figure 3.3: Radiation regions around an aperture antenna [23]

These regions are:

- **Reactive near-field region**: this is the portion of the near-field region immediately surrounding the antenna wherein the reactive field predominates. For most antennas, the outer boundary of this region is commonly taken to exist at a distance $r < 0.62\sqrt{\frac{D^3}{\lambda}}$ from the antenna surface, where λ is the wavelength and D is the largest dimension of the antenna.

- **Radiating near-field (Fresnel) region**: this is that region of the field of an antenna between the reactive near-field region and the far-field region wherein radiation fields predominate and wherein the angular field distribution is dependent upon the distance from the antenna. The inner boundary is taken to be the distance $r \geq 0.62\sqrt{\frac{D^3}{\lambda}}$ and the outer boundary the distance $r < 2\frac{D^2}{\lambda}$. In this region the field pattern is, in general, a function of the radial distance and the radial field component may be appreciable.

- **Far-field (Fraunhofer) region**: this is that region of the field of an antenna where the angular field distribution is essentially independent of the distance from the antenna. The far-field region is commonly taken to exist at distances greater than $2\frac{D^2}{\lambda}$ from the antenna. In this region, the field components are essentially transverse (radial component becomes unimportant) and the angular distribution is independent of the radial distance where the measurements are made. The fields amplitude is instead proportional to $\frac{1}{r}$ in this zone.

In this work, for what concerns the characterization of the antennas, the focus will be kept on far-field properties. Evaluating antennas performances in the far-field region is by now, indeed, a standard procedure, due to the fact that good performances in the far-field region usually indicate good performances also in the near-field region.

3.1.6 H and E planes

For the moment, some fundamental antenna parameters and quantities have been introduced. In general, these parameters depend on the space coordinates. Plotting and measuring a given quantity which depends on the three spatial coordinates, however, is quite uncomfortable. It is, thus, useful to plot and measure on some reference planes, which contain the relevant information about the radiation coming out from the antenna. These planes are the so-called H-plane and the E-plane. The first is defined as the plane ”containing the electric field vector on the aperture and the direction of maximum radiation” while the latter is defined as the plane ”containing the magnetic field vector on the aperture and the direction of maximum radiation”[23]. The following picture illustrates the H-plane and the E-plane for a pyramidal horn antenna:

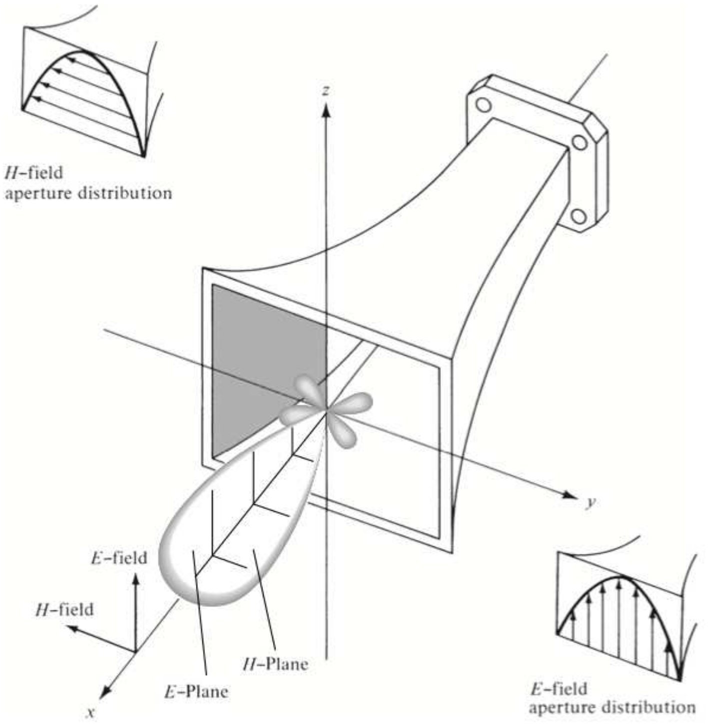

Figure 3.4: Illustration of H-plane and E-plane for a pyramidal horn antenna[23]

3.1.7 Far-fields in aperture antennas

As already pointed out earlier, the fundamental quantity needed to describe the radiation emitted by an antenna is the electromagnetic field. Once the electromagnetic field is known, many derived and more complex quantities can be computed. In this section a theoretical description of the method to compute the far-field radiation of aperture antennas will be illustrated. It is fair, however, to precise that just the main passages of the calculations will be reported, since it is not interest of this thesis to deeply enter into the technicalities of the theory. The computation of the far-fields is based on the Huygens equivalence principle [25] of electromagnetism, which states that the fields outside an imaginary closed surface, which contains the real sources, can obtained by placing over the closed surface suitable fictitious electric and magnetic currents which satisfy some boundary conditions. An illustration of the method is given in the following picture:

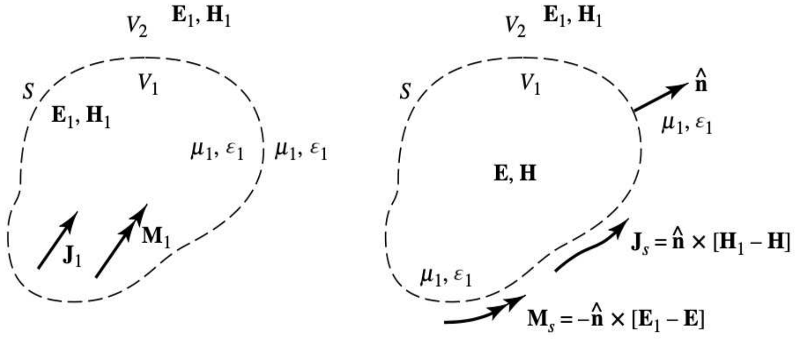

(a) Actual problem (b) Equivalent problem

Figure 3.5: Huygens equivalence principle [23]

With reference to the picture, the equivalent sources are give by:

$$\begin{aligned} \mathbf{J}_s &= \mathbf{n} \times [\mathbf{H}_1 - \mathbf{H}] \\ \mathbf{M}_s &= -\mathbf{n} \times [\mathbf{E}_1 - \mathbf{E}] \end{aligned} \tag{3.13}$$

The equivalent fields inside the surface can be chosen in different ways, due to the fact that their expression will influence the expression of the equivalent surface, but not the computed far-fields. For the present derivation, the equivalent surface will be taken to be the union of two surfaces. The first one is an infinite plane where one can draw a finite curve circumscribing the entire family of rays diffused by the antenna. The latter plane is exactly the plane containing the antenna aperture, while the curve is exactly the antenna aperture. On this plane, the sources will be considered to vanish outside the aperture. It is important to say that, in principle, this approach could lead to missing some of the diffraction effects around the edges of the aperture. The second part of the surface is, instead, the hemisperical cap of infinite radius directed behind the antenna, where the fields, and the equivalent surfaces, can be considered to vanish. At this point, once $\mathbf{J}_s$ and $\mathbf{M}_s$ are known on the aperture, the fields radiated by the antenna can be computed by manipulating Maxwell's equations Eqs. (2.1) . In order to illustrate how to compute the fields, it is convenient to start by noting that $\mathbf{B}$ is a solenoidal field, that means it can be expressed as the curl of a given vector potential $\mathbf{A}$. Thus $\mathbf{H}$ is expressed as:

$$\mathbf{H} = \frac{1}{\mu} \nabla \times \mathbf{A} \tag{3.14}$$

In the frequency domain, substituting into the Maxwell's equation for the curl of $\mathbf{E}$:

$$\nabla \times [\mathbf{E} + j\omega \mathbf{A}] = 0 \tag{3.15}$$

At this point, it is easy to understand that $\mathbf{E}$ can be expressed as the gradient of an electrostatic potential which will be called ϕ:

$$\mathbf{E} = -\nabla\phi - j\omega\mathbf{A} \tag{3.16}$$

Taking now the curl of Eq. (3.14), for an homogeneous medium:

$$\mu\nabla \times \mathbf{H} = \nabla(\nabla \cdot \mathbf{A}) - \nabla^2\mathbf{A} \tag{3.17}$$

At this point one can substitute the latter in the Maxwell's equation for the curl of $\mathbf{H}$ getting:

$$\mu\mathbf{J} + j\omega\mu\epsilon\mathbf{E} = \nabla(\nabla \cdot \mathbf{A}) - \nabla^2\mathbf{A} \tag{3.18}$$

Now, using Eq. (3.15) and Eq. (3.16) :

$$\nabla^2\mathbf{A} + k^2\mathbf{A} = -\mu\mathbf{J} + \nabla(\nabla \cdot \mathbf{A} + j\omega\mu\epsilon\phi) \tag{3.19}$$

Due to Gauge Invariance[15], there is a freedom in choosing the divergence of $\mathbf{A}$. The Lorentz condition is used here[15]:

$$\nabla \cdot \mathbf{A} = -j\omega\epsilon\mu\phi \tag{3.20}$$

In this way, Eq. (3.19) becomes:

$$\nabla^2\mathbf{A} + k^2\mathbf{A} = -\mu\mathbf{J} \tag{3.21}$$

A similar derivation can be made considering magnetic currents $\mathbf{M}$. Although magnetic currents are physically unrealizable, equivalent magnetic currents arise when we use the volume or the surface equivalence theorems. A vector potential $\mathbf{F}$ associated with these magnetic currents can be introduced and the following equation can be proven:

$$\nabla^2\mathbf{F} + k^2\mathbf{F} = -\epsilon\mathbf{M} \tag{3.22}$$

At this point, with some calculations, it is possible to express the solution of Eq. (3.21) and Eq. (3.22) as integrals of the electric and magnetic currents:

$$\begin{aligned} \mathbf{A} &= \frac{\mu}{4\pi}\iiint_V \mathbf{J}\frac{e^{-jkR}}{R}dv \\ \mathbf{F} &= \frac{\epsilon}{4\pi}\iiint_V \mathbf{M}\frac{e^{-jkR}}{R}dv \end{aligned} \tag{3.23}$$

Where $\mathbf{R} = \mathbf{r} - \mathbf{r}'$, $\mathbf{r}$ is the vector from the origin (which coincides with the aperture's center) to the observation point and $\mathbf{r}'$ is the integration variable which spans over the sources region

V. Once the potentials are known, the fields can be expressed as:

$$\begin{aligned}\mathbf{E} &= -j\omega\mathbf{A} - j\frac{1}{\mu\omega\epsilon}\nabla(\nabla\cdot\mathbf{A}) - \frac{1}{\epsilon}\nabla\times\mathbf{F} \\ \mathbf{H} &= \frac{1}{\mu}\nabla\times\mathbf{A} - j\omega\mathbf{F} - \frac{j}{\omega\mu\epsilon}\nabla(\nabla\cdot\mathbf{F})\end{aligned} \tag{3.24}$$

So, at this point, Eqs. (3.23) can be used to compute the field radiated by the antenna, by using the equivalent sources in the place of **J** and **M**, and integrating over the equivalent surface, i.e. the aperture. The problem is that the integrals of Eqs. (3.23) are usually very hard to compute. Luckily, they simplify when a point in the far-field domain is chosen as observation point. In the far-field domain, indeed, the following approximations hold :

$$\begin{aligned}R \simeq r - r'\cos\psi \rightarrow &\quad for\ phase\ variations \\ R \simeq r \rightarrow &\quad for\ amplitude\ variations\end{aligned} \tag{3.25}$$

Where ψ is the angle between **R** and **r**. Geometrically, this approximations derives from the assumption that **R** and **r** are almost parallel in the far-field limit. Substituting Eqs. (3.25) in Eqs. (3.23):

$$\begin{aligned}\mathbf{A} &\simeq \frac{\mu e^{-jkr}}{4\pi r}\mathbf{N} \\ \mathbf{F} &\simeq \frac{\epsilon e^{-jkr}}{4\pi r}\mathbf{L}\end{aligned} \tag{3.26}$$

Where **N** and **L** are defined as follows:

$$\begin{aligned}\mathbf{N} &= \iint_A \mathbf{J}_s e^{jkr'\cos\psi} \\ \mathbf{L} &= \iint_A \mathbf{M}_s e^{jkr'\cos\psi}\end{aligned} \tag{3.27}$$

The integration is now performed on the aperture A. One could now use Eqs. (3.26) to compute the fields in the far-field limit using Eqs. (3.23). After computations which won't be shown here it turns out that, as expected, in the far-field limit the radial components of both electric and magnetic field are negligible with respect to the angular ones. The angular components, instead, have the expression:

$$\begin{aligned}E_\theta &\simeq -\frac{jke^{-jkr}}{4\pi r}\left(L_\phi + \eta N_\theta\right) \\ E_\phi &\simeq \frac{jke^{-jkr}}{4\pi r}\left(L_\theta - \eta N_\phi\right) \\ H_\theta &\simeq \frac{jke^{-jkr}}{4\pi r}\left(N_\theta - \frac{L_\theta}{\eta}\right) \\ H_\phi &\simeq -\frac{jke^{-jkr}}{4\pi r}\left(N_\theta + \frac{L_\phi}{\eta}\right)\end{aligned} \tag{3.28}$$

Where $\eta = \mu_0 c$, while θ and ϕ denote the usual spherical angular coordinates. To conclude, it can be said that the described method provides a way to compute the far-fields radiated by the antenna, simply knowing the fields over the antenna aperture. For this reason the method is also called near to far-field transformation method. A possible issue with the latter method is represented by the fact that the integration over the aperture could lead to miss some of the diffraction effects on the aperture border [26]. For the interests of the present work, these effects can be nelected. In the following the derivations of the far-fields expressions for the pyramidal and the hoghorn antennas are presented.

Pyramidal horn

For a pyramidal horn, the aperture fields can be approximated by treating the horn as a radial waveguide [27]. The process is straightforward but laborious, and it will not be included here.

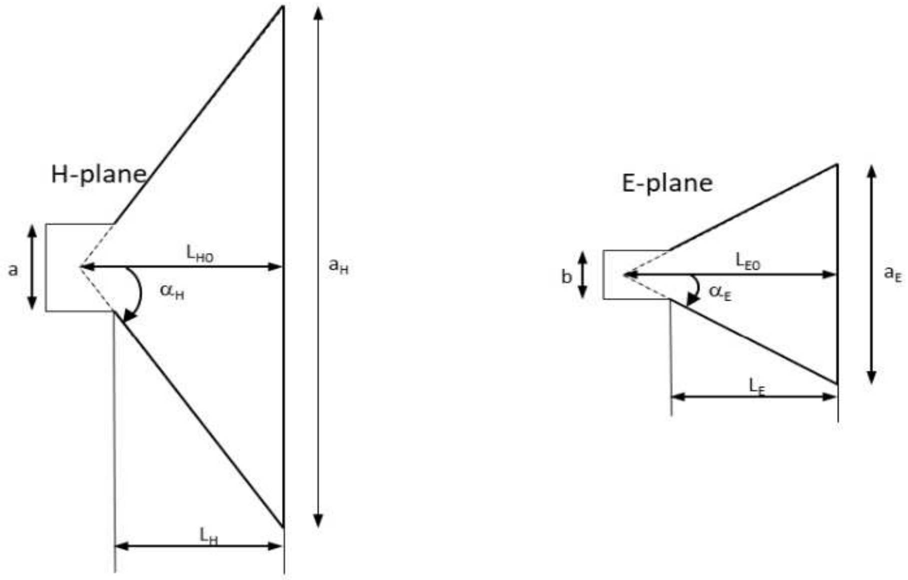

Figure 3.6: E-plane and H-plane views of pyramidal horn

A scheme of a standard pyramidal horn and of the parameters used in the following is illustrated in Figure 3.6. Furthermore, it has to be specified that the aperture is chosen to be in the xy plane, so that the **z** vector is the vector perpendicular to the aperture. In RFX-mod2's reflectometer, due to the waveguide's structure and due to the exploited frequency range, the dominant mode propagating into the waveguide is the TE_{10} mode, which has the electric field in the transverse direction with respect to the direction of propagation of the wave. In addition, the horn's length is large compared to the aperture's dimensions, so the lowest order mode fields at the aperture of the horn can be shown, by radial waveguide method, to read:

$$\begin{aligned} E_y(x',y') &= E_0 \cos\frac{\pi}{a_H}x' e^{-j\left[k\left(\frac{x'^2}{L_{H0}}+\frac{y'^2}{L_{E0}}\right)/2\right]} \\ H_x(x',y') &= -\frac{E_0}{\eta}\cos\frac{\pi}{a_H}x' e^{-j\left[k\left(\frac{x'^2}{L_{H0}}+\frac{y'^2}{L_{E0}}\right)/2\right]} \end{aligned} \tag{3.29}$$

Inserting these fields in Eq. (3.13), with **E** and **H** equal to zero and $\mathbf{n} = \mathbf{z}$, it is straightforward to prove that the equivalent currents on the aperture are given by:

$$\begin{aligned} M_x(x',y') &= E_0 \cos\frac{\pi}{a_H}x' e^{-j\left[k\left(\frac{x'^2}{L_{H0}}+\frac{y'^2}{L_{E0}}\right)/2\right]} \\ J_y(x',y') &= -\frac{E_0}{\eta}\cos\frac{\pi}{a_H}x' e^{-j\left[k\left(\frac{x'^2}{L_{H0}}+\frac{y'^2}{L_{E0}}\right)/2\right]} \end{aligned} \tag{3.30}$$

The N_θ,N_ϕ , L_θ and L_ϕ can now be computed using Eqs. (3.27), and it can be shown that the consequent far-fields read:

$$\begin{aligned} E_\theta &= -j\frac{kE_0e^{jkr}}{4\pi r}\left[sin(\phi)(1+cos(\theta))I_1I_2\right] \\ E_\phi &= j\frac{kE_0e^{-jkr}}{4\pi r}\left[cos(\phi)(cos(\theta)+1)I_1I_2\right] \end{aligned} \tag{3.31}$$

For what concerns the magnetic field, it has the same expression of the electric field but has a perpendicular direction and is rescaled by a factor η. I_1 and I_2, instead, are given by:

$$\begin{aligned} I_1 &= \int_{-\frac{a_H}{2}}^{+\frac{a_H}{2}} cos\left(\frac{\pi}{a_H}x'\right) e^{-jk\left[\frac{x'^2}{2L_{H0}}-x'sin(\theta)cos(\phi)\right]}dx' \\ I_2 &= \int_{-\frac{a_E}{2}}^{+\frac{a_E}{2}} cos\left(\frac{\pi}{a_H}x'\right) e^{-jk\left[\frac{y'^2}{2L_{E0}}-y'sin(\theta)cos(\phi)\right]}dx' \end{aligned} \tag{3.32}$$

It is possible to show, after some computation, that I_1 and I_2 can be put in the form:

$$\begin{aligned} I_1 =& \frac{1}{2}\sqrt{\frac{\pi L_{H0}}{k}}(e^{j\frac{k_x'^2 L_{E0}}{2k}}([C(t_2')-C(t_1')]-j[S(t_2')-S(t_1')])+ \\ & e^{j\frac{k_x''^2 L_{E0}}{2k}}([C(t_2'')-C(t_1'')]-j[S(t_2'')-S(t_1'')])) \end{aligned} \tag{3.33}$$

Where $C(x)$ and $S(x)$ are the tabulated cosine and sine Fresnel integrals, and t_1',t_2',t_1'',t_2'',k_x',k_x''

are defined by:

$$
\begin{aligned}
t_1' &= \frac{1}{\pi k L_{H0}}\left(-\frac{k a_H}{2} - k_x' \rho_2\right)\\
t_2' &= \frac{1}{\pi k L_{H0}}\left(+\frac{k a_H}{2} - k_x' \rho_2\right)\\
t_1'' &= \frac{1}{\pi k L_{H0}}\left(-\frac{k a_H}{2} - k_x'' \rho_2\right)\\
t_2'' &= \frac{1}{\pi k L_{H0}}\left(+\frac{k a_H}{2} - k_x'' \rho_2\right)\\
k_x' &= k\sin(\theta)\cos(\phi) + \frac{\pi}{a_H}\\
k_x'' &= k\sin(\theta)\cos(\phi) - \frac{\pi}{a_H}
\end{aligned}
\tag{3.34}
$$

I_2, instead, can be written as:

$$
I_2 = \frac{1}{2}\sqrt{\frac{\pi L_{E0}}{k}}\, e^{j\frac{k_y^2 L_{E0}}{2k}}\left([C(t_2) - C(t_1)] - j[S(t_2) - S(t_1)]\right) \tag{3.35}
$$

Where t_1,t_2 and k_y are given by:

$$
\begin{aligned}
t_1 &= \sqrt{\frac{1}{\pi k L_{E0}}}\left(-\frac{k a_E}{2} - k_y L_{H0}\right)\\
t_2 &= \sqrt{\frac{1}{\pi k L_{E0}}}\left(\frac{k a_E}{2} - k_y L_{E0}\right)\\
k_y &= k\sin(\phi)\sin(\theta)
\end{aligned}
\tag{3.36}
$$

From the expression of the fields one could compute the power density of the far-field radiation and the antennas directivity. The latter is an important parameter for the design of the antenna, since its dimensions have to be chosen in order to maximise it. Here, without showing the tedious calculations, it is sufficient to say that the directivity of the pyramidal horn can be expressed as:

$$
D_{pyr} = \frac{8_{E0} L_{H0}}{a_H a_E}\left[(C(u) - C(v))^2 + (S(u) - S(v))^2\right] \cdot \left[C\left(\frac{a_E}{\sqrt{2\lambda \text{Ł}_{E0}}}\right)^2 + S\left(\frac{a_E}{\sqrt{2\lambda \text{Ł}_{E0}}}\right)^2\right] \tag{3.37}
$$

Where:

$$
\begin{aligned}
u &= \frac{1}{\sqrt{2}}\left(\frac{\sqrt{\lambda L_{H0}}}{a_H} + \frac{a_H}{\sqrt{\lambda L_{H0}}}\right)\\
v &= \frac{1}{\sqrt{2}}\left(\frac{\sqrt{\lambda L_{H0}}}{a_H} - \frac{a_H}{\sqrt{\lambda L_{H0}}}\right)
\end{aligned}
\tag{3.38}
$$

It will be the core of this work to compare the latter theoretical expressions for directivity and for the angular distribution of the radiation with simulations and experimental measurements. In particular, this will be the topic of chapter 6.

Hogg-horn antenna

For the hoghorn antenna, an analytic theory would be far too complicated to develop in this context. The difficulty of such approach would lie in the fact that the hoghorn used in this work can be thought as made up by combination of a pyramidal horn and a reflector surface which has the role of deflecting the radiation of $\frac{\pi}{2}$ with respect to the pyramidal horn's axis. The theory is, however, complicated by the fact that not all the radiation coming out of the horn will be reflected by the reflector, and this undeflected part will interfere with the reflected radiation making the radiation pattern different from the pyramidal horn's one. It was thus decided, for this kind of antenna, to use the theory of the pyramidal horn explained above for comparison with experimental measurements. Despite it could seem an inappropriate approach, it was motivated by the necessity of making evident the difference between the pyramidal horn antenna and the hoghorn antenna. This is also important in view of reflectometry's applications on RFX-mod2 and DTT, where being aware of the differences between the two kind of antennas will be of primary importance.

3.2 Antennas Modelling

After having introduced the necessary theoretical background, this Section will be devoted to a brief introduction to the simulations tools used in this work. In particular, it will be focused on the description of COMSOL Multiphysics, the simulation software used for the modelling of the antennas. First of all, a general and concise introduction to the software and to its RF module is given. Then, a brief overview of the method used by COMSOL to compute far-fields is provided.

3.2.1 Introduction to COMSOL's RF Module

COMSOL Multiphysics is a finite element analysis, solver, and simulation software package for various physics and engineering applications. The software facilitates conventional physics-based user interfaces and coupled systems of partial differential equations. In particular, COMSOL is structured in various modules. Each module is dedicated to a given branch of physics, and they can also be combined together to solve more complex problems. For this work, only the RF Module of the software has been used. The RF Module, which is a module with functionality optimized for the analysis of electromagnetic waves, perfectly fits to the modelling of antennas. The underlying equations for electromagnetic waves Eqs. (2.1) are automatically available in all of the physics interfaces, and in this work have been solved in the frequency domain. In particular, the method used to solve Maxwell's equations is the Partial Element Equivalent Circuit (PEEC) method, which consists in formulating the electromagnetic problem in terms of circuits variables[28]. This method, over the years, has been extended to accurately include models for dielectrics and scattering problems, and so it is of great utility for antenna modelling [29]. In RF Module, a given physical model can be built from scratch drawing the component geometry and assigning materials properties and electromagnetic boundary conditions. A view of the interface of the COMSOL model for the hoghorn antennas is shown in the following image:

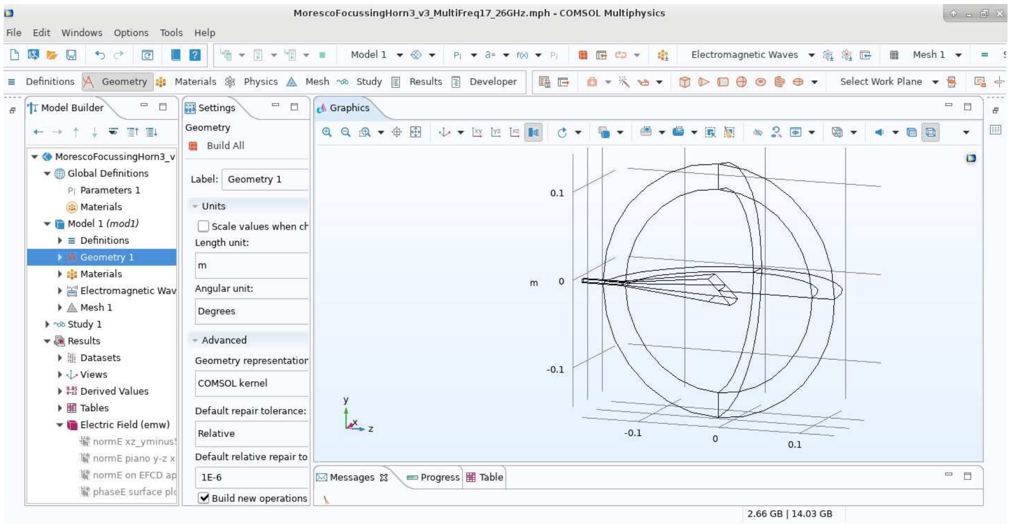
MorescoFocussingHorn3_v3_MultiFreq17_26GHz.mph - COMSOL Multiphysics

Label: Geometry 1

Units

☐ Scale values when ch

Length unit: m

Angular unit: Degrees

Advanced

Geometry representatior: COMSOL kernel

Default repair tolerance: Relative

Default relative repair to: 1E-6

☑ Build new operations

2.66 GB | 14.03 GB

Figure 3.7: Interface of the COMSOL model for the hoghorn antenna

In the model used for this work the antenna was set to be composed of perfectly conducting materials, and a port was inserted to simulate the waveguide. The port's input power was selected according to the experimental conditions, as reported in 5.1. The electromagnetic mode propagating into the waveguide was set to be the TE_{10}. Since the simulation was run in a finite domain, a perfectly matched layer (PML) was inserted at the domain edge. The PML is a perfectly absorbing material which ensures that the resulting field inside the domain doesn't include undesired reflection effects. Another important step of the construction of the model was represented by the choice of the mesh size in each domain. For this purpose it was decided to follow the same prescription used in teh simulations run in the antennas design process[30].

3.2.2 COMSOL's far-field computation

The most important quantity that was derived from the COMSOL simulations, in view of the antennas characterization, is their far-field radiation pattern. The RF Module, to compute far fields, uses the same method described in the previous Chapter. A numerical resolution of the full electromagnetic model in a domain which includes the far-field region, indeed, would almost surely require very high computational resources. The method used by COMSOL, instead, is way less computationally expansive, since it consists in numerically solving the near-field domain of the antenna, and using the solution to compute the far-fields through Eqs. (3.28).

Chapter 4

Experimental apparatus and methods

As mentioned in chapter 1, this thesis focuses on the characterization of the antennas which will be mounted on the RFX-mod2's reflectometer, and on the meausurement of the distance of the antennas from a reflecting mirror. Experimental measurements are thus fundamental for this work. This chapter will be dedicated to a detailed description of the experimental setup and methods, along with a description of the instruments used in the measurements. In particular, the first section of the chapter will be devoted to a more detailed description of the antennas which are to be characterized and mounted on RFX-mod2, while the second and last Section will concentrate on a detailed description of the experimental apparatus and methods

4.1 RFX-mod2's reflectometer antennas

RFX-mod2 will be equipped with four independent bistatic ultrafast reflectometric units working in the frequency range $16 - 26.5$ GHz, in order to be able to exploit the upper X-Mode cut-off frequency and cover the density profile around the LCFS [13]. The reflectometer's antennas are standard pyramidal horns for the low-field side of the torus, while hoghorn antennas are used for the high-field side. The design of the hoghorn antennas was anything but easy, and the choice of such a geometry was dictated by the severe space constraints (due to high-field side localization). The optimization process and the specifications of the final versions of the antennas are illustrated in [30]. Once designed, the antennas were produced in AISI 316 by additive manufacturing techniques (3D printing) commisioned to the company Sisma. Subsequently, they were first chemichally electropolished (to reduce surface porosity) and then covered with a silver and rhodium through galvanic bath (to improve conductivity). The main advantage of producing the antennas through additive manufacturing is represented by the fact that a much wider range of geometries can be explored with this technique, with respect to classical manufacturing. The latter fact, together with growing necessity of designing new antennas to fit the space constraints of upcoming machines, helps to understand why this manufacturing process was chosen. A performance assessment of antennas realized through additive manufacturing is, however, lacking in literature, and is the main objective of the present work. Images of the both the antennas' CAD models are shown in the following pictures:

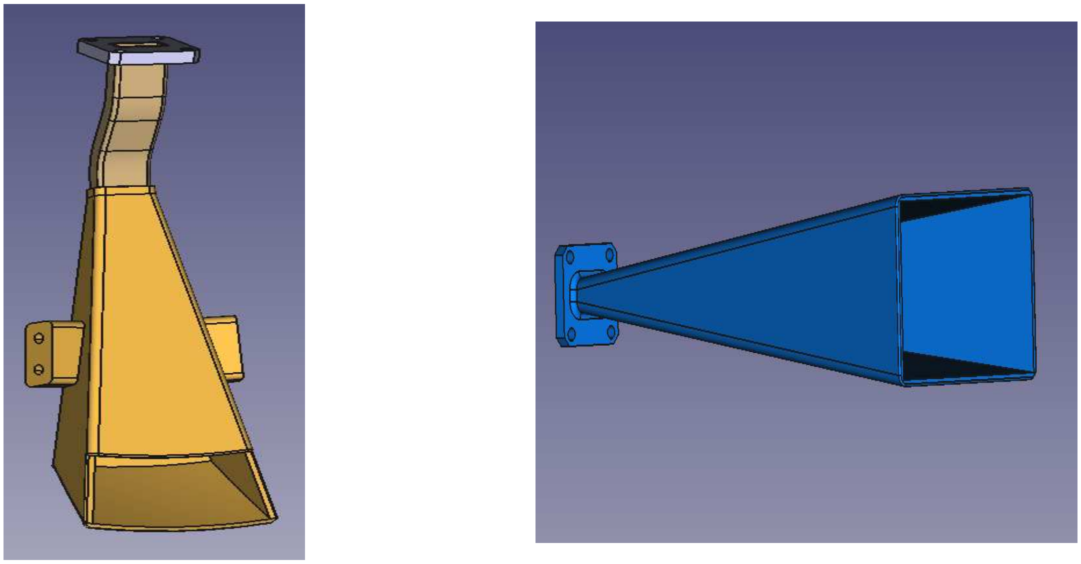

Figure 4.1: Hogg-horn(left) and pyramidal (right) antenna CAD models

4.2 Experimental setup

4.2.1 Setup for antennas characterization

The characterization of the antennas was based on the study of the radiation pattern. Obviously, a full three dimensional study of the latter would be both impracticable and redundant, so E-plane and H-plane have been chosen as evaluation planes where to take measurements. As already specified in chapter 3, it was decided to measure the far field radiation patterns of the two antennas. The far field limits for the pyramidal horn and hoghorn antennas are, at 21 GHz:

	Far-field distance [m]
Pyramidal horn antenna	~ 0.40
Hogg horn antenna	~ 0.25

Table 4.1: Far-field limits of pyramidal and hoghorn antennas

To measure the radiation a receiving pyramidal antenna, identical to the one to be characterized, was chosen. This antenna was connected, through microwave connector, to a HP-E4413A power sensor, which was in turn connected to a HP-E4419A powermeter. The measured quantity is, thus, the electromagnetic power entering into the receiving antenna. The latter was placed on a standard tripod, so that its height could be manually adjusted. The receiving antenna, mounted on the tripod, is reported in the following image:

Figure 4.2: Receiving antenna mounted on its tripod

It was decided that, for reasons of avaliable physical space, it was convenient to rotate the antenna to be characterized with respect to the receiving one. The probing antenna, thus, was mounted on a 3D printed support where it could be rotated on θ and ϕ angles, where the angles are the ones of the reference system used in 3.1.7. Rotation was possible thanks to two Edmund Optics Diameter Rotation Kinematic Mount. Furthermore, the antennas were connected, through a microwave connector and an RF Cable Assmebly SF104/11SMA/11SMA77, to the LC Technology Sweep Reflectometer 0496. In this context the reflectometric unit was only used as microwave source in the $17-26$ GHz band. The wave was then sent, through the connector, into the antenna and diffused into free space.

The riflectometer was remotely controlled through Telnet protocol. Both the pyramidal and hoghorn antennas, mounted on their support and connected to the reflectometric unit, are shown in the following pictures:

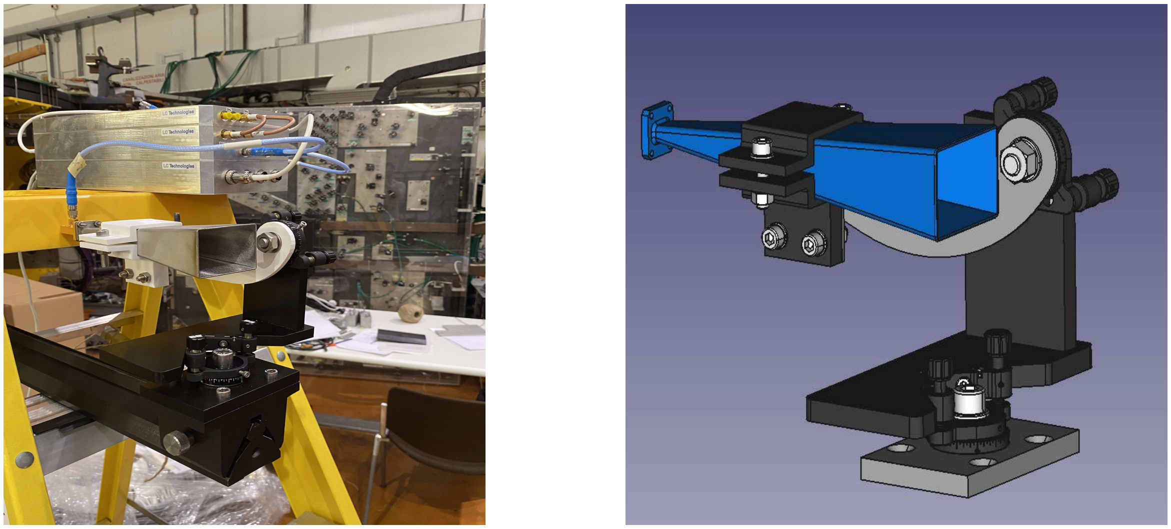

Figure 4.3: Picture(left) and CAD model(right) of the pyramidal antenna mounted on its support

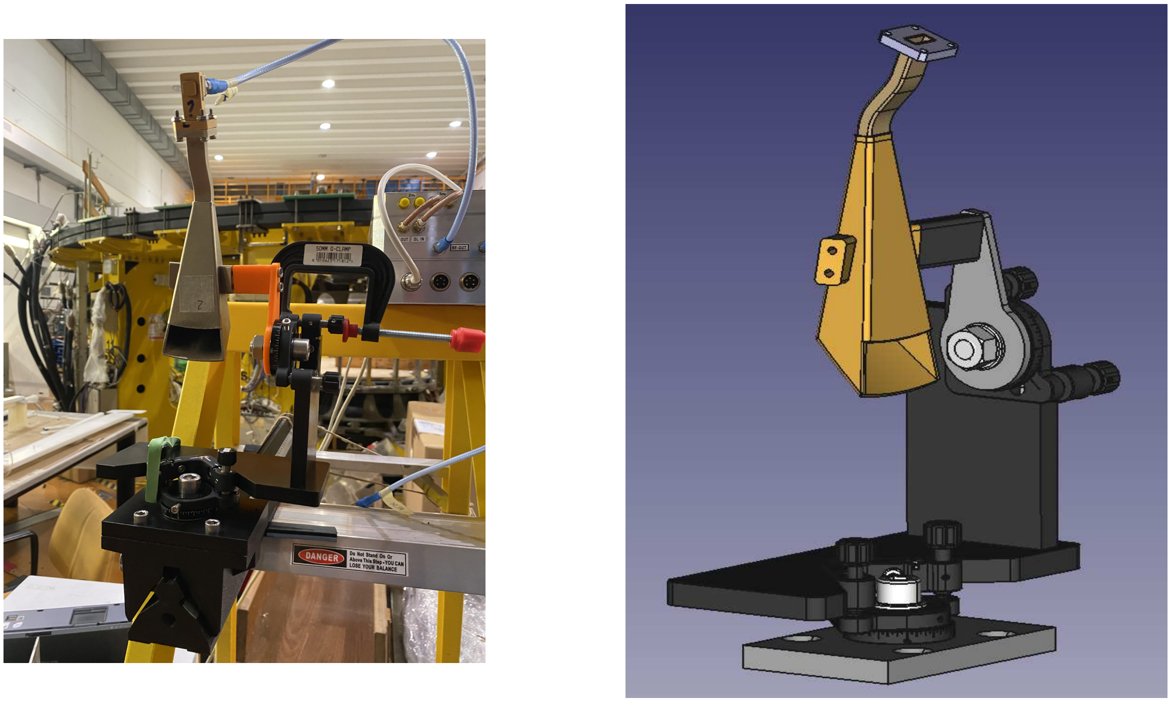

Figure 4.4: Picture(left) and CAD model(right) of the hoghorn antenna mounted on its support

It is also important to say that a standard microwave absorber had to be placed ahead of the receiving antenna, with the aim of avoiding unsolicited reflections that could affect measurements. Finally, a scheme of the full experimental setup is shown in the following picture:

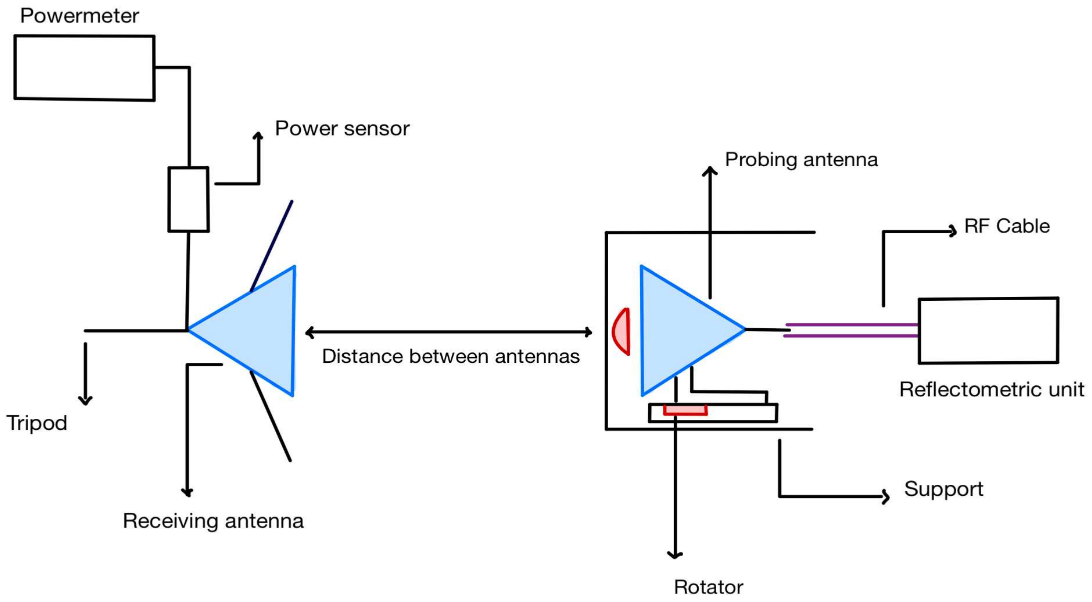

Figure 4.5: Scheme of the experimental apparatus for the antennas characterization

Finally, it needs to be specified that, in order to measure far-field properties, the distance of the probing antennas from the receiving one was set to $1.53\ m$ for the pyramidal antenna's characterization and to $0.63\ m$ for the hoghorn antenna's characterization.

4.2.2 Setup for measurement of the distance from a reflecting mirror

As an additional step, after the characterization of the antennas, it was decided to perform a reflectometric measurement where the plasma presence was simulated through a plane reflecting mirror. The aim of this measurement was to check if the hoghorn antenna, which is the most critical one (see next chapter), is able to provide reliable results at least in this simple case. Therefore, it was necessary to realize, through CAD software, a new support which could contain two hoghorn antennas. The CAD model of the support is shown in the following picture:

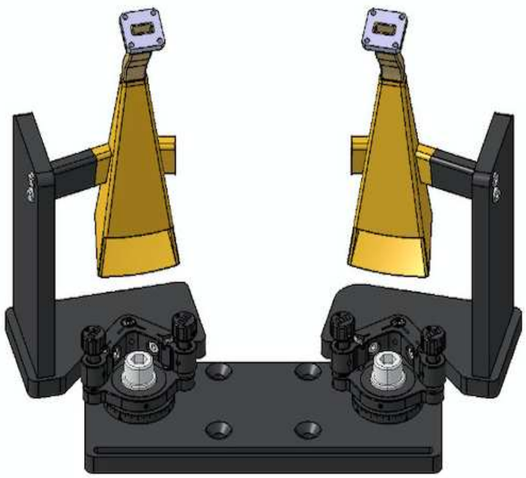

Figure 4.6: Receiving and Transmitting hoghorn antennas mounted on their support

The antennas were connected, through the same microwave connectors and RF cables which were previously named, to the LC technology Sweep Reflectometer 0496. One of the two antennas was used as transmitting antenna, while the other was used as receiving antenna to catch the reflected signal. Thanks to the support the antennas could be rotated, in order to check their performances when they are not parallel. In particular, measurements were taken with parallel antennas and with antennas titled of 10° and 15° with respect to each other. The reason for the chose of the latter inclinations lies in the fact that on RFX-mod2 the antennas will be mounted at a significant distance from each other, due to structural constraints of the machine. The chosen inclinations correspond to the focus at a point where the plasma is expected to be. These tests have, thus, the aim of verifying if the latter layout can work. The reflectometer was set, through Telnet protocol, to perform a sweep (as described in chapter 2) in a time $T_{sw} = 10\ \mu s$, with a frequency range in $[f_{min}[Ghz], f_{max}[Ghz]] = [17, 27]$. The reflectometric unit was connected to a digital Tektronix DPO 7054 Phosphor Oscilloscope, where the output signal of Eq. (2.45) could be read. A Thurbly Thandar Instruments TGP110 10 MHz Pulse Generator was used to generate the trigger signal and was connected both to the oscilloscope and to the reflectometric unit. The trigger signal was used to start both the oscilloscope acquisition and the frequency sweep from the reflectometric unit.

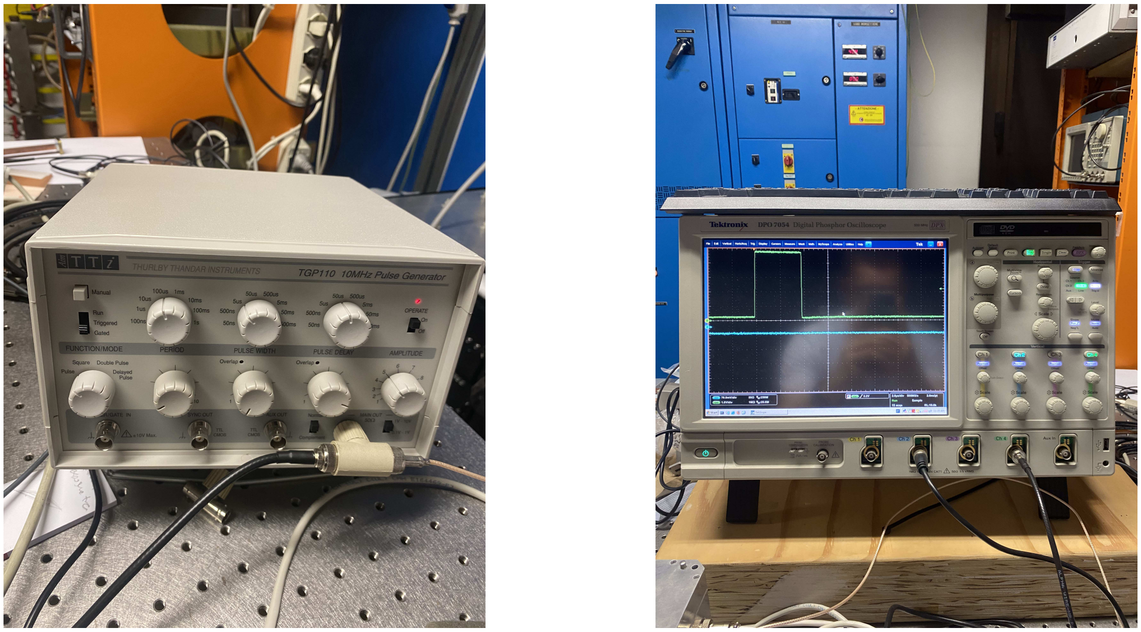

Figure 4.7: Pulse generator (left) and oscilloscope (right) used in the experiment

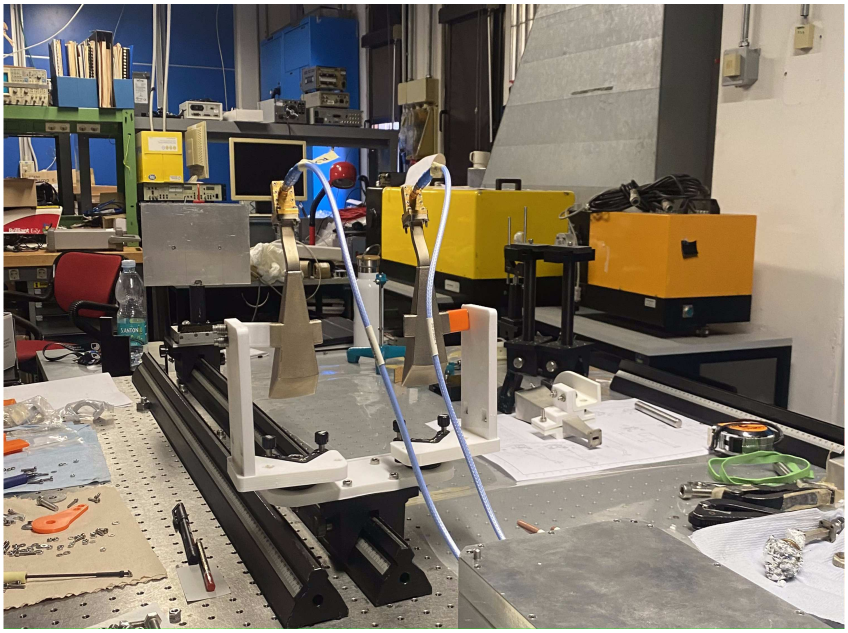

Figure 4.8: Experimental setup for the measurement of the distance from the reflecting mirror

Finally, the mirror was placed in front of the two antennas in such a way to reflect the wave radiated by the probing antenna. For what concerns the reflectometric measurement, in this case, it easy to understand that the ”plasma density” profile of the mirror can be written as:

$$n(x) = n_c \theta((a - L_c) - x) \tag{4.1}$$

Where the same notation of 2.2.1 has been used. L_c, here, is the distance of the antennas from the mirror. Inserting the latter in Eq. (2.30), and considering O-mode propagation, one gets:

$$\begin{aligned}\phi &= \frac{2\omega}{c}\int_{a-L_c}^{a}\sqrt{1-\frac{e^2}{\epsilon_0 m_e n_c \omega^2}\theta((a-L_c)-x)}dx-\frac{\pi}{2}\\ &= \frac{2\omega}{c}L_c-\frac{\pi}{2}\end{aligned} \tag{4.2}$$

Following the same reasoning as in Chapter 2, it is easy to conclude that the reflectometric signal read on the oscilloscope is proprtional to the cosine of the latter phase difference. The beating frequency of the signal is, considering the fact that a linear sweep in performed:

$$f_b = \frac{1}{2\pi}\frac{d\phi}{dt} = \frac{2L_c}{c}\frac{d\omega}{dt} = \frac{2L_c}{c}\frac{\omega_{max}-\omega_{min}}{T_{sw}} \tag{4.3}$$

Where $T_{sw} = 10\ \mu s$ is the sweep's duration and $\omega_{max}-\omega_{min} = 20\pi\ GHz$ is sweep's range in angular frequency. Thus, from the measurement of the beating frequency the distance $|2L_c|$, i.e. the difference between the optical paths of the probing (RX) and reference (RX) signal, can be computed. The module, here, derives from the used detection scheme (homodyne), which only allows to measure the absolute value of the phase shift. It is important to state, at this point, that the previous theory did not consider the fact that the RX-signal, in any reflectometeric unit, is passed through a delay line of length L_0 before being mixed with the TX-signal. A consequence of this fact is that, with the technique explained above, the measured quantity will be $|2L_c - L_0|$ instead of $|2L_c|$. To conclude, a scheme of the full experimental setup is shown in the following:

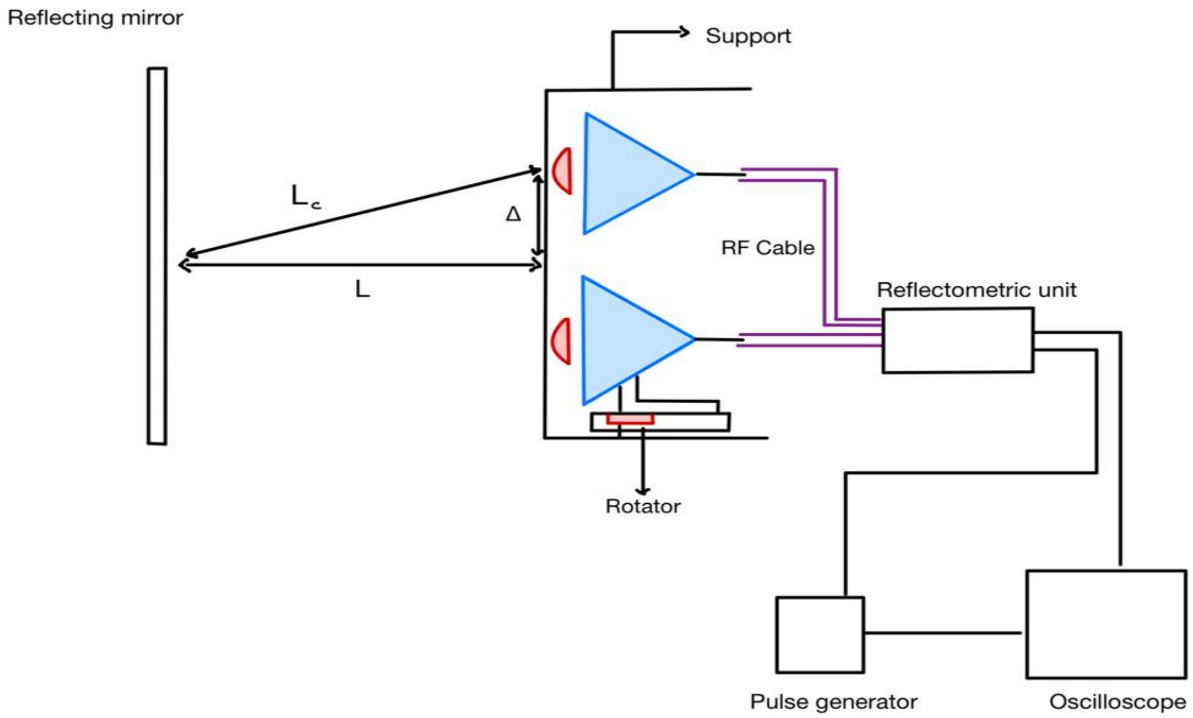

Figure 4.9: Scheme of the experimental apparatus for the measurement of the distance of the antennas from the reflecting mirror

As can be seen from the previous figure, L_c is the distance from the center of the antenna aperture to the mirror, along the oblique sides of the isosceles triangle formed by the two antenna centers and by the middle of the mirror, i.e. the distance covered by the part of the transmitted radiation which will be absorbed by the receiving antenna after reflection. The latter is, thus, the distance to be measured with reflectometry. Δ, instead, is half the distance between the centers of the two antenna apertures, and it is equal to $\Delta = 6.95\ cm$. The last parameter is L, which is the distance between the mirror plane and the plane which contains the two antenna aperture. This distance is the distance that was experimentally set during the present part of this work.

Chapter 5

Experimental results and discussion

In this chapter the results of the characterization of the antennas and of the measurements of the distance from the reflecting mirror will be presented and discussed. Experimental measurements, obtained with the methods described in chapter 4, will be compared with numerical results and with the theoretical model described in chapter 3. For what concerns the characterization of the antennas , results will be presented separately for pyramidal and hoghorn antennas, in order to put in evidence the differences between the two. The results of the reflectometric measurement of the distance from the reflecting mirror, instead, will be fully presented for the case of parallel antennas, while only the most significant plots will be shown for the case of tilted antennas. It is important to say, at this point, that some experimental measurements are reported in this chapter without the error. This happens when the experimental error turns out to be remarkably smaller with respect to the measurements. Reporting the error, thus, would be useless in this case.

5.1 Antennas characterization

5.1.1 Results

In this subsection the polar plots of the H-plane and E-plane's radiation patterns will be plotted for both antennas. It is important to say that the plotted quantity is the radiation entering the receiving antenna, which is the quantity that was experimentally measured. The COMSOL's estimation of the latter quantity was obtained extracting from the software the electric field $\mathbf{E}_C$ around the antenna, and using the known relation which says that for spherical waves (that is the case of far-field radiation) the power density of radiation is given by:

$$W = \frac{E_C^2}{2Z} \tag{5.1}$$

The same procedure was used for theoretical curves, with the only difference that the used electric field, in this case, is the one whose expression is given in 3.1.7. In this subsection, also the fundamental parameters of the antennas, which are HPBW and directivity, are reported.

Pyramidal Antenna

In the following, the radiation patterns on E-plane and H-plane for the pyramidal antenna are reported:

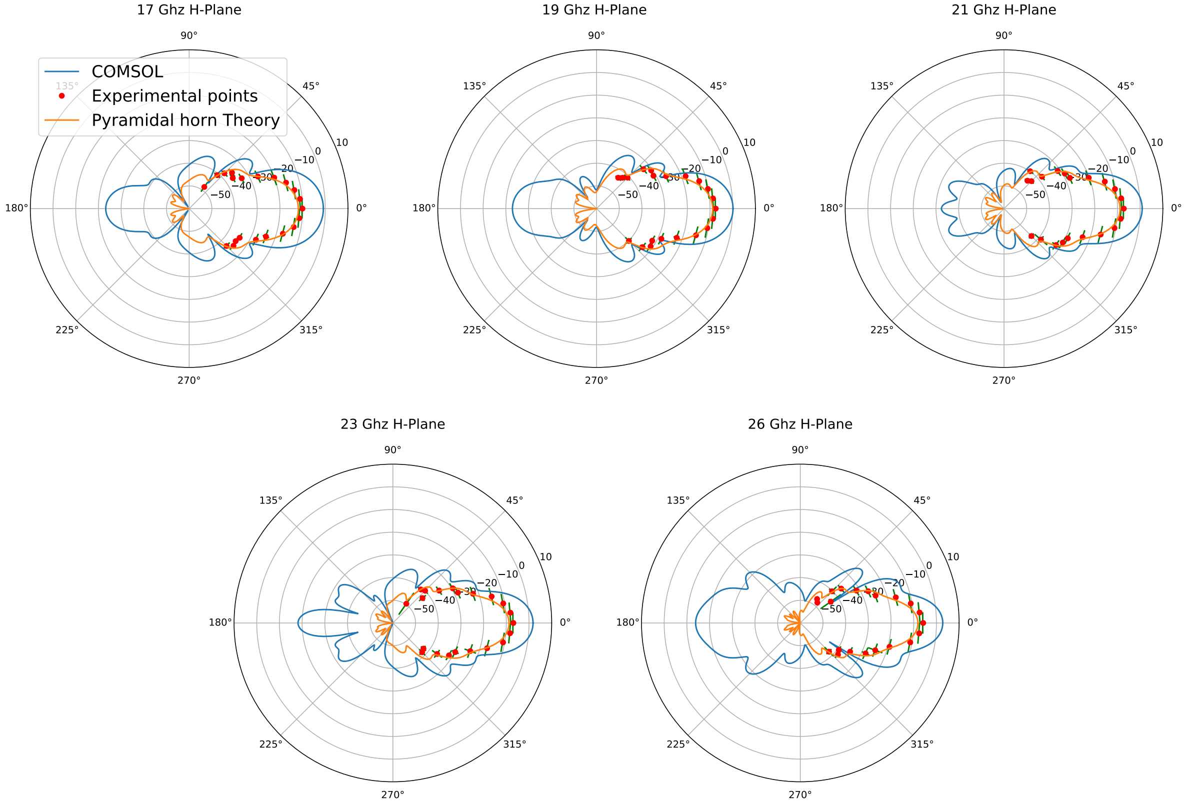
17 Ghz H-Plane
19 Ghz H-Plane
21 Ghz H-Plane
23 Ghz H-Plane
26 Ghz H-Plane

Figure 5.1: H-plane Radiation polar plots (dBm) at 1.53 m in K-band for pyramidal antenna

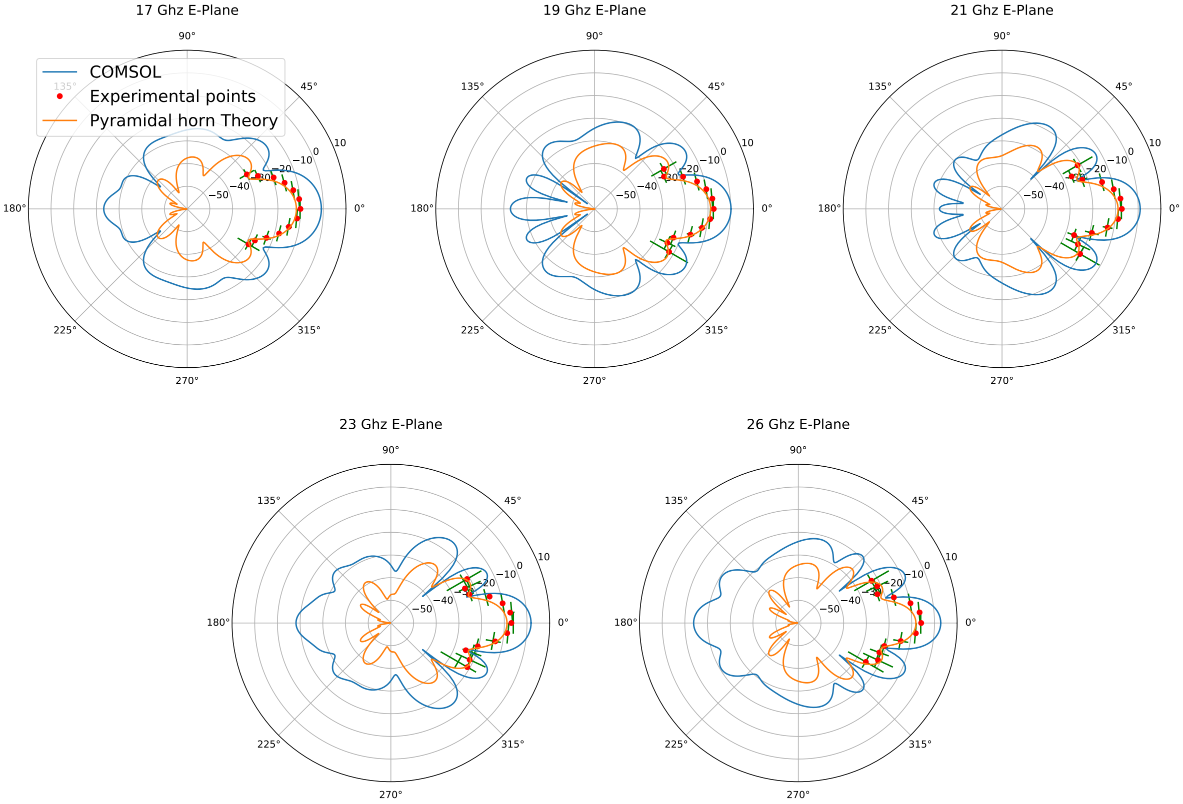

Figure 5.2: E-plane Radiation polar plots (dBm) at 1.53 m in K-band for pyramidal antenna

As can be seen from the previous figures, agreement between the theoretical model and the experimental points is excellent. The COMSOL simulation, instead, despite having an angular distribution which well mimics the one of the theoretical model, appears to present a radiation power which is higher in absolute value. It can be assumed that the reason for this behaviour lies both in the losses of the transmission line which carries the energy from the reflectometer to the antenna and in the antennas defects, which may absorb part of the radiation. The COMSOL simulation, instead, considers the antenna structure as a perfect conductor with no losses and defects, and is runned with the nominal power coming out of the reflectometric unit (~ 0.042 W) as input power. To estimate the actual power radiated by the antenna, the theoretical curves were used. Those curves, indeed, were obtained performing a best-fit on the E_0 of Eqs. (3.29) with respect to the experimental points. Once obtained E_0, the fitted expression could be numerically integrated over the sphere at $r = 1.53$ m at each frequency, in order to derive the actual power P_{rad} radiated by the antenna at each of the analysed frequencies. The effective radiated powers are reported below:

Frequency (Ghz)	$\mathbf{E_0[V/m]}$	$\mathbf{P_{rad}[mW]}$
17	193 ± 5	14 ± 1
19	246 ± 6	23 ± 1
21	225 ± 7	19 ± 1
23	210 ± 7	17 ± 1
26	205 ± 7	16 ± 1

Table 5.1: Effective radiated powers as a function of the frequency

The plots of the effective radiated powers, as a function of the experimental frequency, are reported for both antennas in appendix B. With the effective radiated powers as new input powers, it was decided to re-run the COMSOL simulations at each frequency. The same plots of Figure 5.1 and Figure 5.2 are now reported, as obtained with the new input powers:

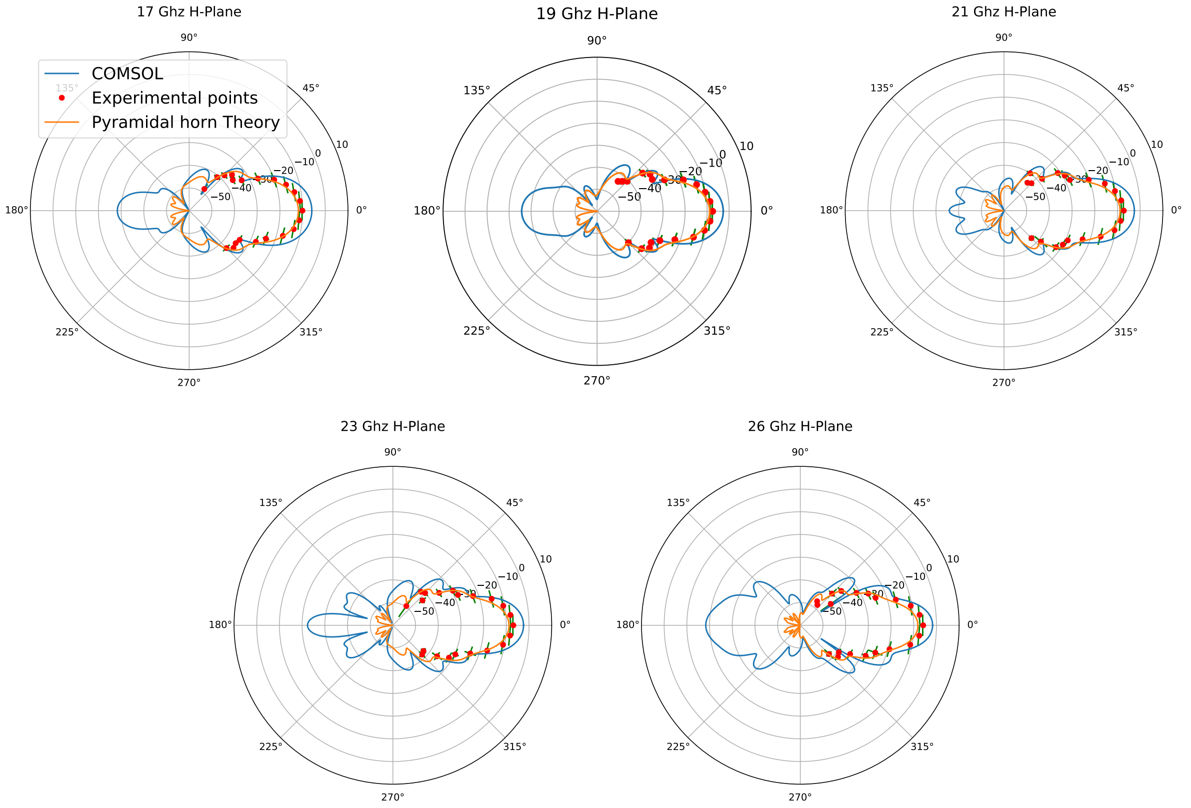

Figure 5.3: H-plane Radiation polar plots (dBm) at 1.53 m in K-band for pyramidal antenna with effective power

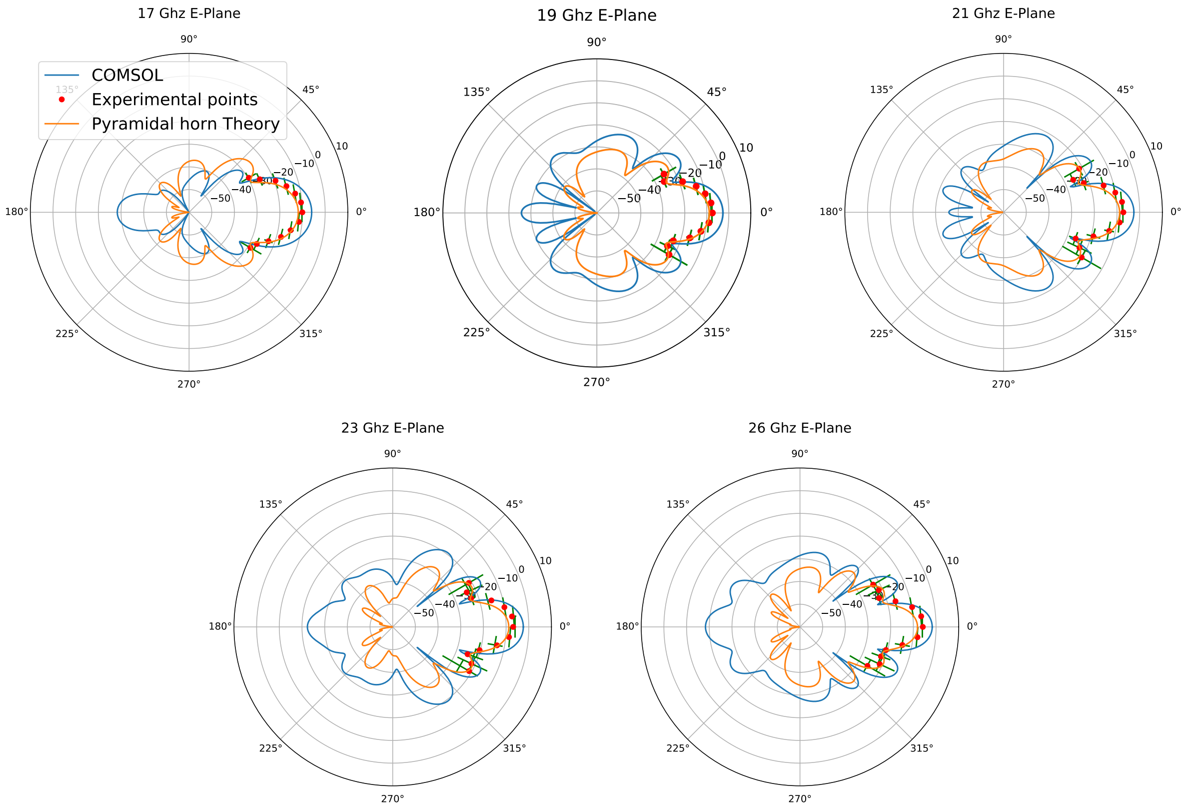

Figure 5.4: E-plane Radiation polar plots (dBm) at 1.53 m in K-band for pyramidal antenna with effective power

From the previous polar plots, it is evident that correcting the input powers clearly improved the results. On both H and E-planes and for all frequencies, especially close to the radiation maximum, the agreement between experimental points, theory and simulation is now remarkable. The region behind the antenna still is characterized by substantial divergence between the curves, but this shouldn't represent a problem for the purposes of this work, since the backward radiation of the antennas won't be involved in reflectometric physics. Furthermore, as described in [30], mesh size in this region was far less coarse, and this could be cause of inaccuracies in the COMSOL simulation. For completeness, just for the 17 GHz case, the cartesian plots of the E and H-plane patterns are reported. All the others cartesian plots (also the ones for the hoghorn antenna) can be found in appendix A.

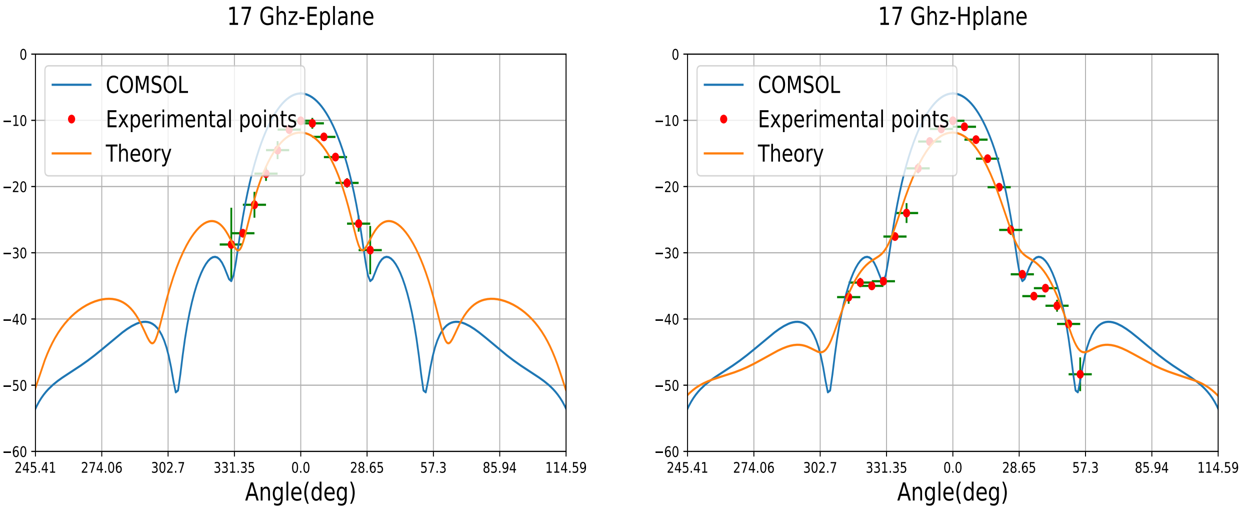

Figure 5.5: Cartesian plots of radiation(dBm) at 17 Ghz for pyramidal antenna with effective power

At this point, some parameters of the curves can be compared, in order to have a quantitative estimation of the accuracy between simulation, theory and experiment. In particular, the quantities that will be compared are the directivity and the HPBW, both defined in chapter 3. It is important to specify that, because of the high agreement between experimental measures and theory, it was decided to use the value of the fitted theoretical curves as experimental HPBW and directivity. The obtained directivities and HPBWs are reported in the following tables:

Frequency[Ghz]	**D**$_C$	**D**$_{exp}$
17	273.52	63.11
19	342.54	77.44
21	517.39	92.25
23	500.50	107.9
26	728.0	130.55

Table 5.2: COMSOL (D_C) and experimental (D_{exp}) directivity as a function of the frequency

Frequency[Ghz]	**HPBW**$_{E,C}$**[deg]**	**HPBW**$_{E,exp}$**[deg]**	**HPBW**$_{H,C}$**[deg]**	**HPBW**$_{H,exp}$**[deg]**
17	22	22	22	23
19	19	20	19	20
21	17	19	17	18
23	20	18	19	17
26	14	16	14	15

Table 5.3: COMSOL ($HPBW_C$) and experimental ($HPBW_{exp}$) directivity on both E and H-planes as a function of the frequency

Hoghorn antenna

In this section the results of the characterization of the hoghorn antenna are reported. The plots will be the same as those described in the previous Section. As already specified in 3.1.7, the theoretical model adopted in this case is the pyramidal horn's one. As input power for the COMSOL simulation, instead, it was decided to take, as a first try, the mean value of the effective input powers of Table 5.1.

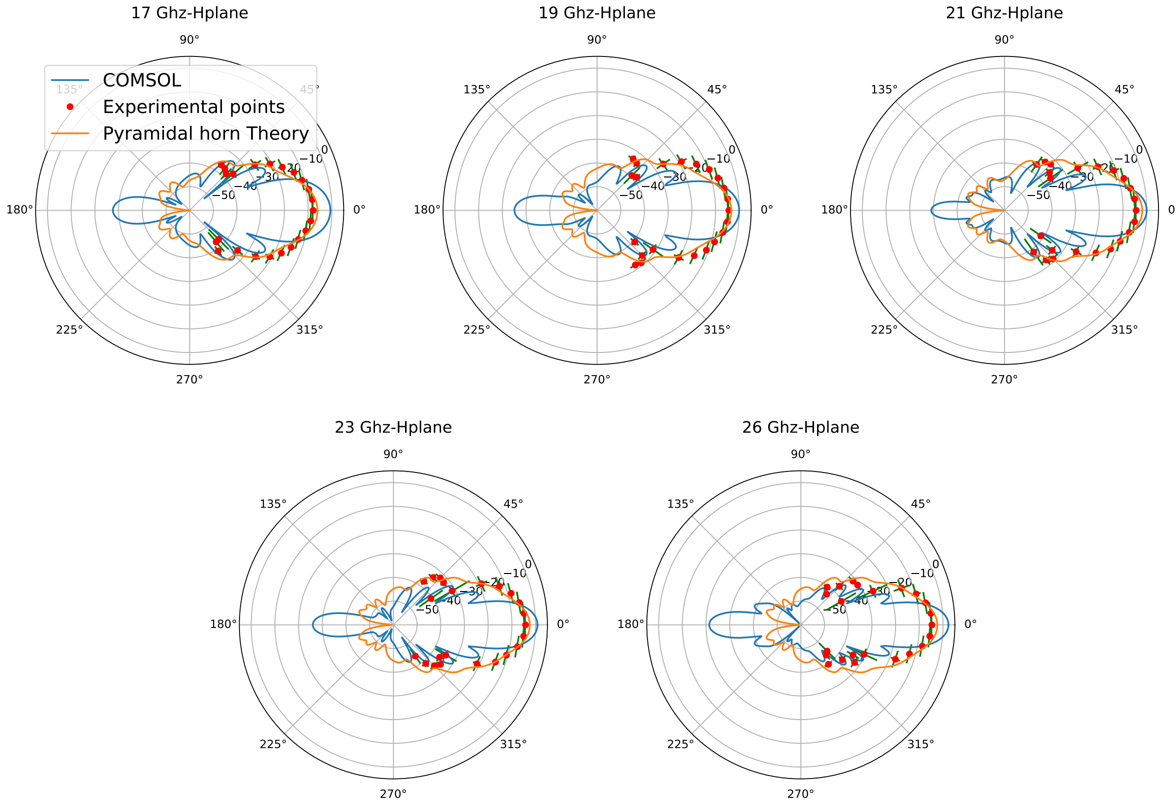

Figure 5.6: H-plane Radiation polar plots (dBm) at 0.63 m in K-band for hoghorn antenna

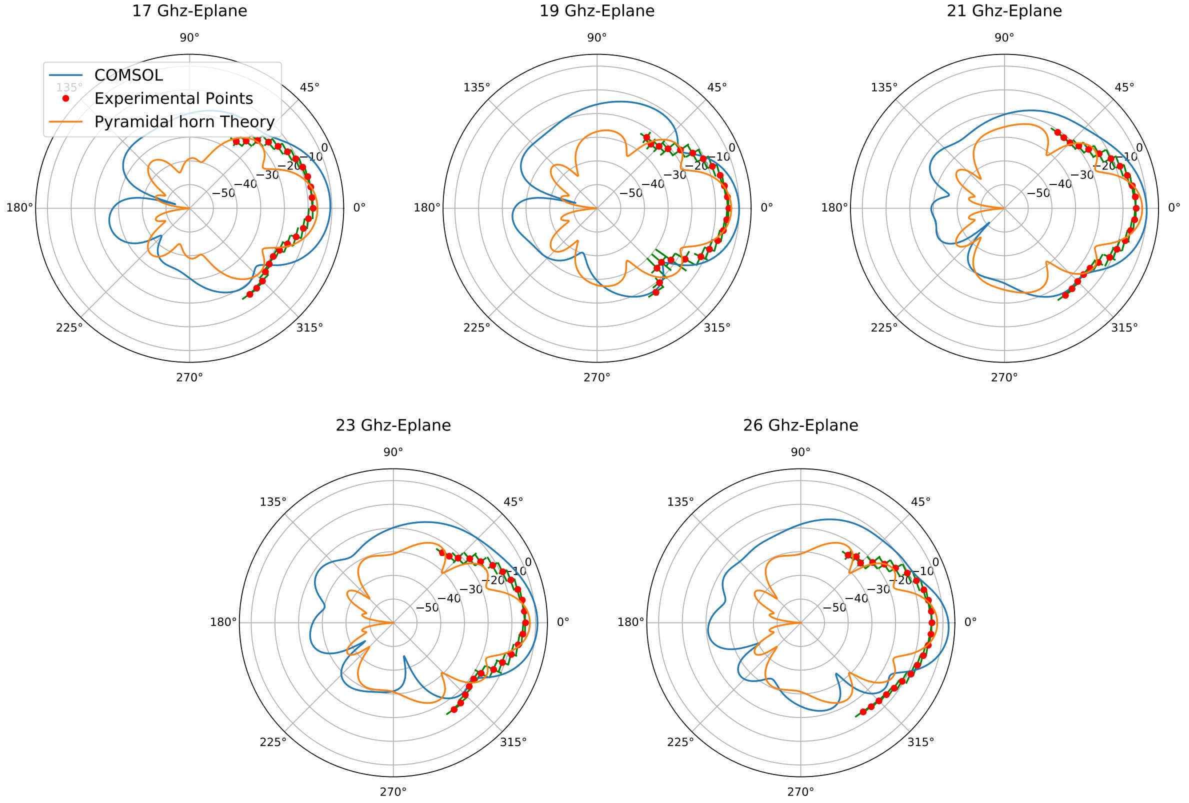

Figure 5.7: E-plane Radiation polar plots (dBm) at 0.63 m in K-band for hoghorn antenna

The previous plots clearly illustrate the difference between the pyramidal horn antenna and the hoghorn antenna. Despite the hoghorn antenna is basically a pyramidal horn with the addition of a parabolic reflector to tilt the radiation towards the plasma[30], its radiation pattern diverges significantly from the one of the pyramidal antenna. A more detailed discussion on the difference between the two antennas will be given in next Section. Also for the hoghorn antenna COMSOL's simulation were re-run with the radiated powers fitted from the theory:

Frequency (Ghz)	$\mathbf{E_0[V/m]}$	$\mathbf{P}_{rad}\mathbf{[mW]}$
17	150 ±7	9 ± 1
19	186±10	13 ± 1
21	204±11	16 ± 2
23	180 ±10	13 ± 1
26	151 ±9	9 ± 1

Table 5.4: Effective radiated powers as a function of the frequecny

As can be seen from the previous table, the effective power radiated by the hoghorn antenna is, in genereal, smaller than the effective power radiated by the pyramidal antenna. This proves that, also from the point of view of the energy losses, the two antennas are different. Running the COMSOL simulations with the effective radiated powers as new input powers, the following plots were obtained:

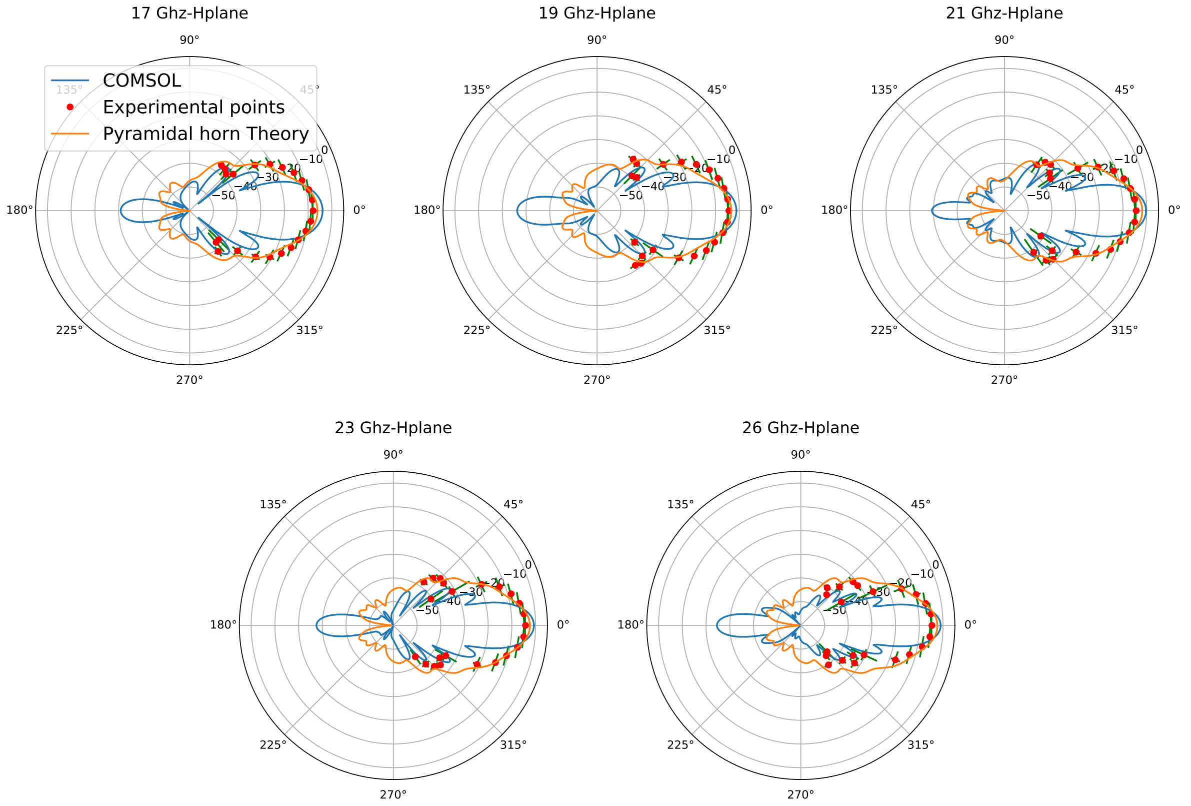

Figure 5.8: H-plane Radiation polar plots (dBm) at 0.63 m in K-band for hoghorn antenna and effective power

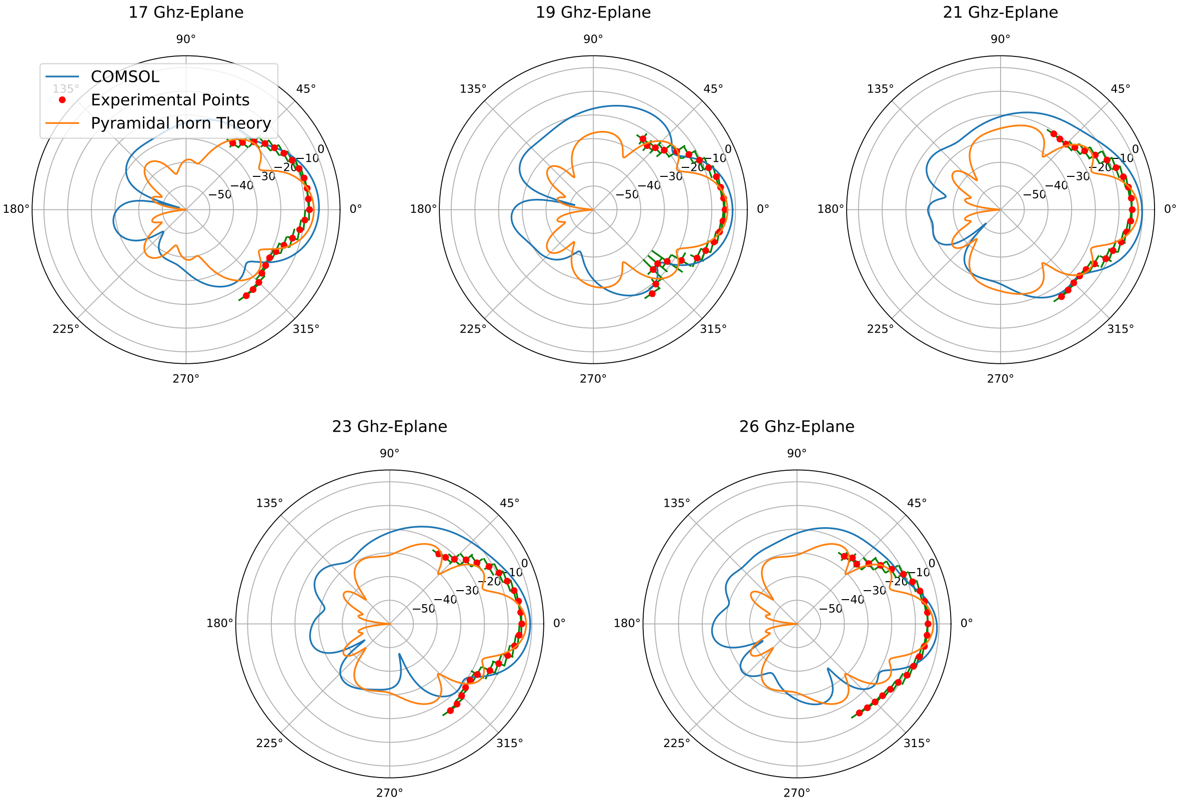
17 Ghz-Eplane
19 Ghz-Eplane
21 Ghz-Eplane
23 Ghz-Eplane
26 Ghz-Eplane

Figure 5.9: E-plane Radiation polar plots (dBm) at 0.63 m in K-band for hoghorn antenna and effective power

Also in this case, using the fitted powers improved the agreement between the curves in terms of scale. The angular distribution, instead, obviously remains the same, and all the considerations made above are still valid. As for the pyramidal horn's case, the parameters of the antenna are reported below. It is important to specify that, because of the extreme divergence between the theoretical model of the pyramidal horn antenna and the other curves, the theoretical parameters won't be reported in the following.

Frequency[Ghz]	$\mathbf{D}_C$	$\mathbf{D}_{exp}$
17	116.80	46.59
19	217.17	62.74
21	269.50	51.75
23	244.75	68.82
26	229.37	88.17

Table 5.5: COMSOL (D_C) and experimental (D_{exp}) directivity as a function of the frequency

Frequency[Ghz]	**HPBW$_{E,C}$[deg]**	**HPBW$_{E,exp}$[deg]**	**HPBW$_{H,C}$[deg]**	**HPBW$_{H,exp}$[deg]**
17	39	35	18	27
19	30	33	16	28
21	35	33	14	25
23	32	23	12	32
26	25	21	11	39

Table 5.6: COMSOL ($HPBW_C$) and experimental ($HPBW_{exp}$) directivity on both E and H-planes as a function of the frequency

5.1.2 Discussion of the results

It is now possible to discuss the characterization of the two antennas, through a comparison between their parameters and their radiation patterns. For what concerns the radiation patterns, it can be seen from Figure 5.3 and Figure 5.4 that the pyramidal horn antenna presents a very high agreement between experimental points, theory and simulation. The hoghorn antenna instead, looking at Figure 5.8, shows an H-plane pattern with an angular distribution which recalls the H-plane pyramidal horn's pattern, but is way less directive. On the same plane, instead, the COMSOL's plots are more directive and show small secondary lobes which could not be experimentally solved. The hoghorn's E-plane pattern of Figure 5.9, on the contrary, presents an asymmetric radiation pattern, which significantly differs from the corresponding pyramidal theory. As explained in Chapter 3, the latter fact is due to the interference effects between the radiation deflected by the reflector and the undeflected radiation, which contribute to create the wide lobes which can be seen on the E-plane patterns. On this plane, the COMSOL patterns are instead more representative of the experimental points, since the COMSOL simulation numerically finds the aperture fields to use to compute the far-fields. Looking now at Table 5.2 and Table 5.5, it is evident that for both antennas the simulated directivity D_C is way higher with respect to the experimental directivity D_{exp}. This is due to the fact that, despite the performed optimization of the input power, the COMSOL curves still have maximum of the radiation which are above the maximum measured radiations. As can be seen from Table 5.3 and Table 5.6 the HPBWs, instead, show for both antennas a good agreement between simulated and experimental values, indicating that the angular distribution of the radiation is similar in the two cases. The latter fact is remarkable, since the angular distribution of the radiation is expected to be a determining factor in view of reflectometric applications. On the other hand, the inaccuracy of the COMSOL plots in explaining the scale of the radiation (which results in the divergence of directivities) is probably due to the fact that simulations are performed using finite element method, which is still an approximation of the real physics. Another reason for the latter fact can be found in the problem of border effects. As pointed out in Chapter 3, indeed, the method used by COMSOL to compute far-fields could miss some border effects by integrating over the aperture. A possible future improvement, in this sense, could be to reduce the mesh size of the COMSOL simulation or to try to use an alternative simulations software like CST. To conclude, it can be said that the hoghorn antenna proved to be more critical with respect to the pyramidal one. Despite the H-plane radiation's angular distribution is resembling of the pyramidal horn's one, the two antennas present strong divergences on the E-plane, which is the plane where the asymmetry of the hoghorn antenna plays a crucial role. It will be fundamental, in the future, to carry out experiments in order to verify how the deformed radiation patterns of the hoghorn antenna may affect the quality of the reflectometric measurements. A very basical and preliminary experiment, in this sense, was the measurement of the distance of the antennas from the reflecting mirror, whose results will be illustrated in the next Section.

5.2 Measurement of the distance from the reflecting mirror

5.2.1 Results

First of all, the measurements taken with the antennas positioned parallel to each other will be analysed and discussed. Using the same parameters introduced in Figure 4.9, it is important to say that measurements were taken at the values of $L[cm] = 15, 20, 25, 30, 35, 40, 50$. The following images show the experimental signal, along with the cosine fit needed for beating frequency estimation, with mirror positioned at $L = 15\ cm$ and $L = 30\ cm$ from the antennas.

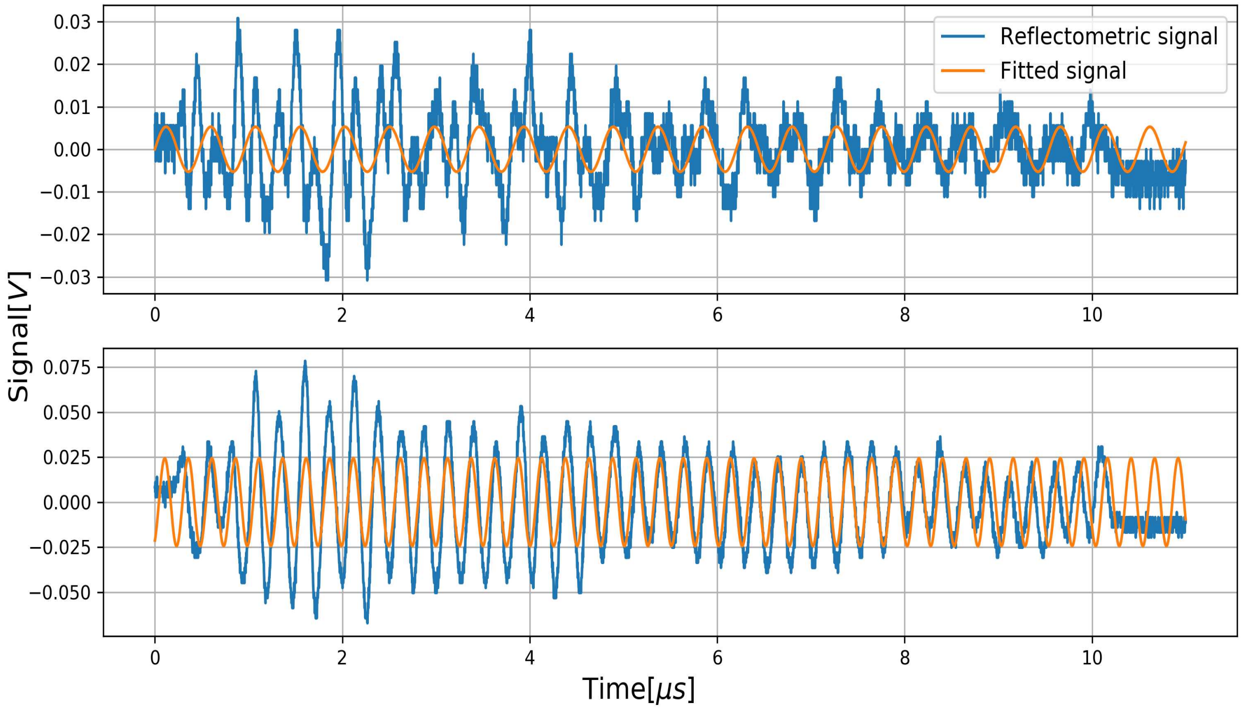

Figure 5.10: Reflectometric signal with mirror at 15 cm (top) and at 30 cm (bottom), along with cosine fit

It is evident from the previous images that the signal at 15 cm is more noisy and the cosine fit is less accurate with respect to the fit of the signal at 30 cm. This is due to the fact that 15 cm is too much below the far-field limit of the hoghorn antenna (which is ~ 25 cm), and so, at this distance, the irregularity of the near-field is still too high to have a clean signal. The signals corresponding to the other distances are reported in appendix C. As said in the previous chapter, due to the homodyne detection scheme adopted by the RFX-mod2's reflectometer, only the quantity $|2L_c - L_0|$ can be measured from the beating frequency ω_b of the reflectometric signal (thanks to Eq. (4.3)). The latter quantity and ω_b, as measured for each distance of the mirror from the antenna, are reported in the following table:

L[cm]	$\mathbf{L}_c[cm]$	$\boldsymbol{\omega}_b[10^6\text{Hz}]$	$\lvert\mathbf{2L}_c - \mathbf{L}_0\rvert_{exp}[cm]$
15	16.53	13.16	62.86
20	21.173	28.51	136.14
25	25.94	26.77	127.82
30	30.79	24.98	119.29
35	35.68	23.13	110.46
40	40.59	21.26	101.51
50	50.48	17.16	84.12

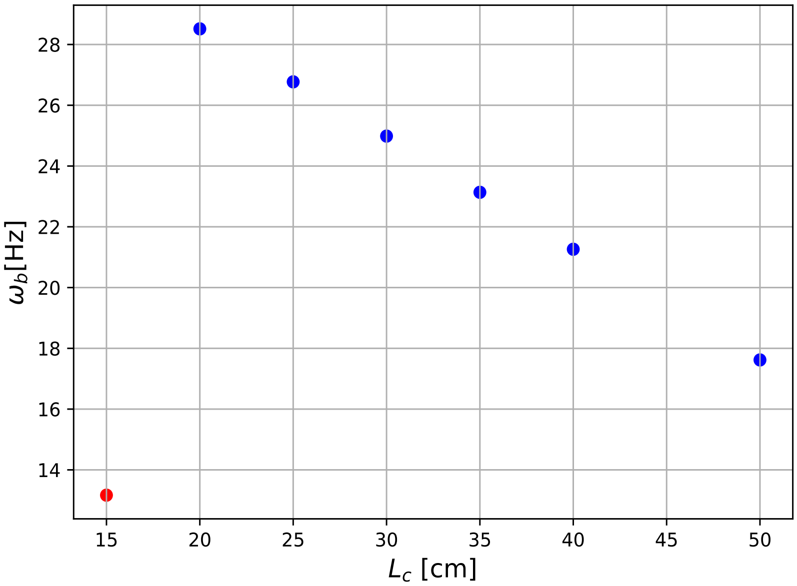

Figure 5.11: Signal's beating frequency as a function of L_c (the point in red refers, as said below, to the measurement at 15 *cm* influenced by near-field effects)

As can be seen from the previous plots, the behaviour of ω_b is linear with L_c, except for the red point at $L_c = 16.53\ cm$. The linear behaviour was expected since, as seen in 4.2.2, the beating frequency is proportional to $|2L_c - L_0|$. The deviation from linearity, at $L_c = 15\ cm$ (the red point on the previous plot), is of course a consequence of the noisy signal at this distance, whose cause was explained above. The latter measurement, thus, will not be considered in the following. To verify if the reflectometric measurement is able to predict the distance from the mirror, without the necessity of knowing the delay line's length L_0, it was decided to take the difference between the quantity $|2L_c - L_0|$, as measured between adjacent experimental distances L_c. This difference, looking to the expression for ω_b derived in 4.2.2, should be equal to two times the difference between the adjacent distances. The obtained results are shown in the following table:

	True value [cm]	**Measured value [cm]**
$\Delta(\lvert 2L_c - L_0\rvert_{exp})_{2,3}$	9.54	8.32
$\Delta(\lvert 2L_c - L_0\rvert_{exp})_{3,4}$	9.7	8.52
$\Delta(\lvert 2L_c - L_0\rvert_{exp})_{4,5}$	9.78	8.82
$\Delta(\lvert 2L_c - L_0\rvert_{exp})_{5,6}$	9.82	8.92
$\Delta(\lvert 2L_c - L_0\rvert_{exp})_{6,7}$	19.78	17.40

Table 5.7: Variation of $|2L_c - L_0|$ as measured for adjacent distances from the mirror compared with expected value

Where $\Delta(|2L_c - L_0|_{exp})_{i,j} = |2L_{c,j} - L_0|_{exp} - |2L_{c,i} - L_0|_{exp}$, with $L_{c,1}, L_{c,2}, L_{c,3}.., L_{c,7} = 16.53\ cm, 21.17\ cm, 25.94\ cm, ..., 50.48\ cm$. The latter table shows that the reflectometric measurements are sensitive, with an accuracy of the the order of the 10%, to variations of the mirror position. Again, in order to measure the distance of the antennas L_c only relying on the reflectometric signal, one should know the length of the delay line L_0. A measurement of L_0, i.e. a calibration of the instrument, can be performed using the previous measurements of the beating frequency and exploiting the fact that the experimental values of L_c are known. It is sufficient, indeed, to fit the ω_b's expression Eq. (4.3), as a function of the known experimental distances, with a linear relation. At this point it is trivial to derive L_0 from the fit's results.

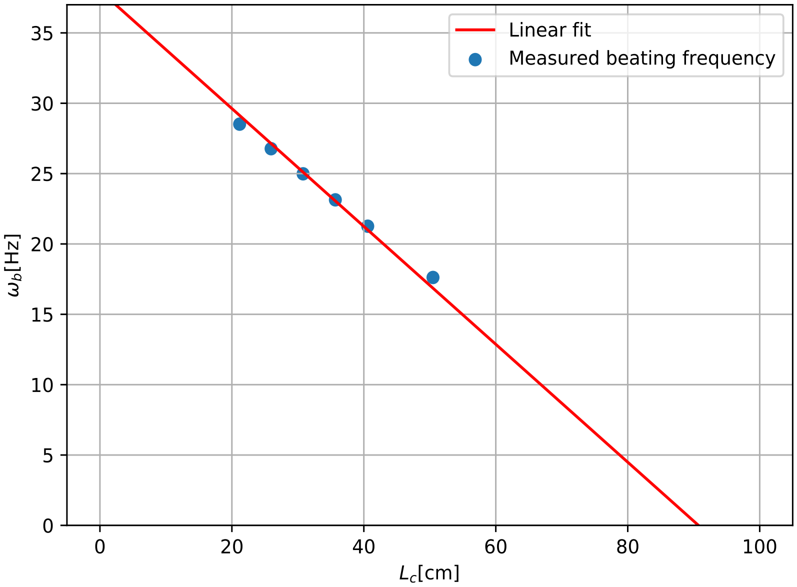

Figure 5.12: Signal's beating frequency as a function of mirror distance along with linear fit

Following the latter method, it turns out that :

$$L_0[cm] = 181.44 \tag{5.2}$$

Using the calibration performed above to derive the value of L_0, it is now possible to compute, from the measurements taken with the antennas tilted of 10° and 15°, the reflectometric estimation of L_c. The expected values of L_c, to be compared with the measured values, coincide with the ones of the parallel antennas case. This is due to the fact that, for small inclinations of the antennas, the radiation absorbed by the receiving antenna still predominantly follows the same optical path shown in Figure 4.9. In the following scatter plots, the comparison between expected and measured L_c for the two antennas inclinations are shown:

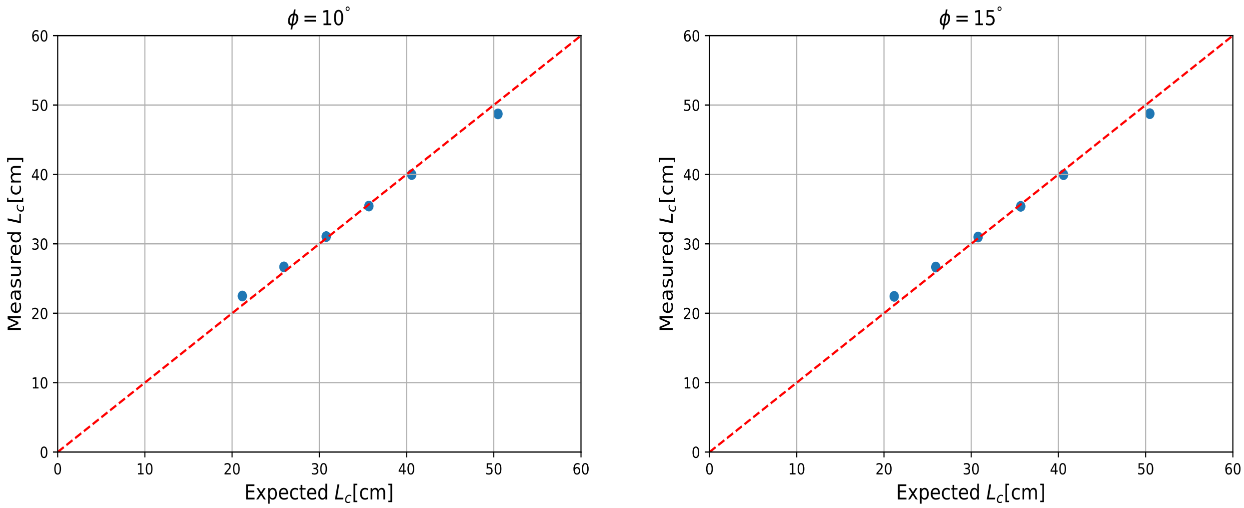

Figure 5.13: Scatter plot of expected vs measured L_c for the two antennas inclinations (named as ϕ). The red dashed line corresponds to perfect match between expected and measured values of L_c

5.2.2 Discussion of the results

As can be seen from Figure 5.10, when the distance from the mirror is higher than the far field limit of the hoghorn antenna, the cosine fit is quite well in agreement with the reflectometric signal. The consequence of the latter fact is that the measurements are sensitive to variations of the mirror position, as can be guessed from Table 5.7. Using the measurements with parallel antennas as a calibration to estimate the delay line's length L_0, Figure 5.13 shows that the reflectometric estimations of the distance of the reflecting mirror are, for tilted antennas, very well in agreement with the experimental distances. Furthermore, looking at the signals obtained with tilted antennas of Figure C.2 and C.3, it can be seen that the latter signals have about a double intensity with respect to the signals obtained with parallel antennas. This proves that, as expected, tilting the antennas with respect to each other (of angles of about $10^{\circ} - 15^{\circ}$), as will be done in the RFX-mod2's layout, contributes to greatly amplify the reflectometric signal. To conclude, it can be asserted that, despite the criticalities in its angular distribution, the hoghorn antennas proved to be able to correctly predict the distance from the reflecting mirror.

Chapter 6

Conclusions

The purpose of this thesis was to characterize the two new antennas which will be installed on the RFX-mod2's reflectometer for position control, and to simulate the RFX-mod2's experimental layout in order to assess the performance of the system on benchtest with a reflecting plane mirror. The antennas were realized through additive manufacturing, and this contributes, together with the application of reflectometry on upcoming fusion machines, to make their detailed characterization relevant for the fusion community. In order to achieve the latter objectives, it was decided to compare COMSOL Multiphysics numerical simulations of the antennas with a theoretical method and with experimental measurements. Results indicate that the characterization of the two antennas can be, overall, judged as successfull. The pyramidal antenna, for which less criticalities were expected, has radiation patterns which show an excellent agreement between theory, experimental points and simulated results. The few inaccuracies for the latter antenna, which are limited to its rear part, are not expected to cause any harm in the reflectomteric application and are easily linkable to the larger mesh of the simulation in the rear part of the antenna. The hoghorn antenna instead, due to its complex geometry, turned out to be more critical. Especially on the E-plane, indeed, the latter antenna presents an highly asymmetric radiation pattern, which significantly differs from the corresponding pyramidal horn's pattern. The present characterization, thus, constitutes a remarkable proof of the difference between the two antennas. This difference will have to be taken into account when this kind of antenna will be installed on RFX-mod2. Fortunately, an encouraging sign was given by the results of the measurements of the distance from the reflecting mirror. The latter results, indeed, indicated that the hoghorn antenna is able, at least in this simplified situation, to correctly predict with a good accuracy the distance from the mirror. Of course, due to the simplicity of the reflecting mirror setup, further investigations will be needed, in order to understand if, on real plasmas, the criticalities of the hoghorn's radiation pattern will play a role on the reflectometric measurements. In the simulation methods, instead, future improvements could be represented by a refinement of the COMSOL's mesh size, or by the exploitation of alternative softwares like CST. In general, however, this thesis work can be considered satisfactory, since a successfull characterization of the antennas has been performed for the first time on antennas obtained through additive manufacturing. The latter characterization indicates that, apart for some criticalities for the hoghorn antenna, the two antennas can be considered as reliable, and thus opens to a wide variety of future pissibilities.

Appendices

Appendix A

Cartesian plots for radiation patterns

In this appendix the cartesian plots of the radiation pattern for both pyramidal and hoghorn antennas are reported. For simplicity, only the plots with COMSOL simulation run with the effective powers are reported.

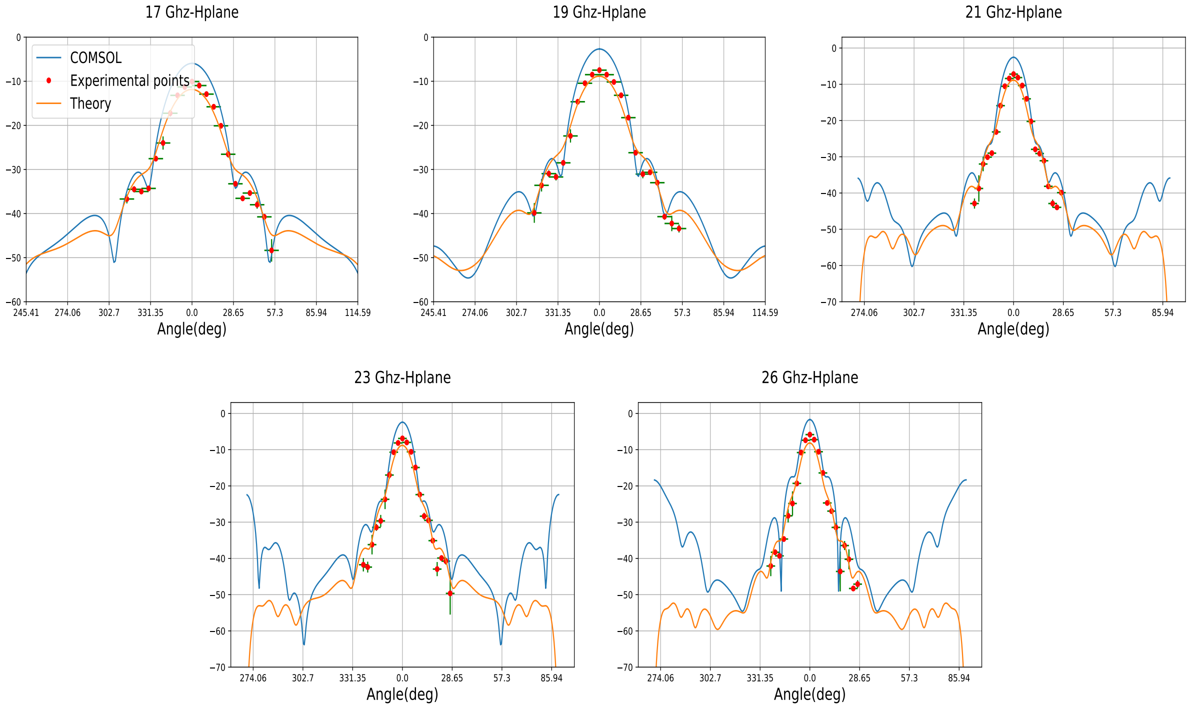

Figure A.1: Cartesian H-plane Radiation plots (dBm) at 1.53 m in K-band for pyramidal antenna with effective power

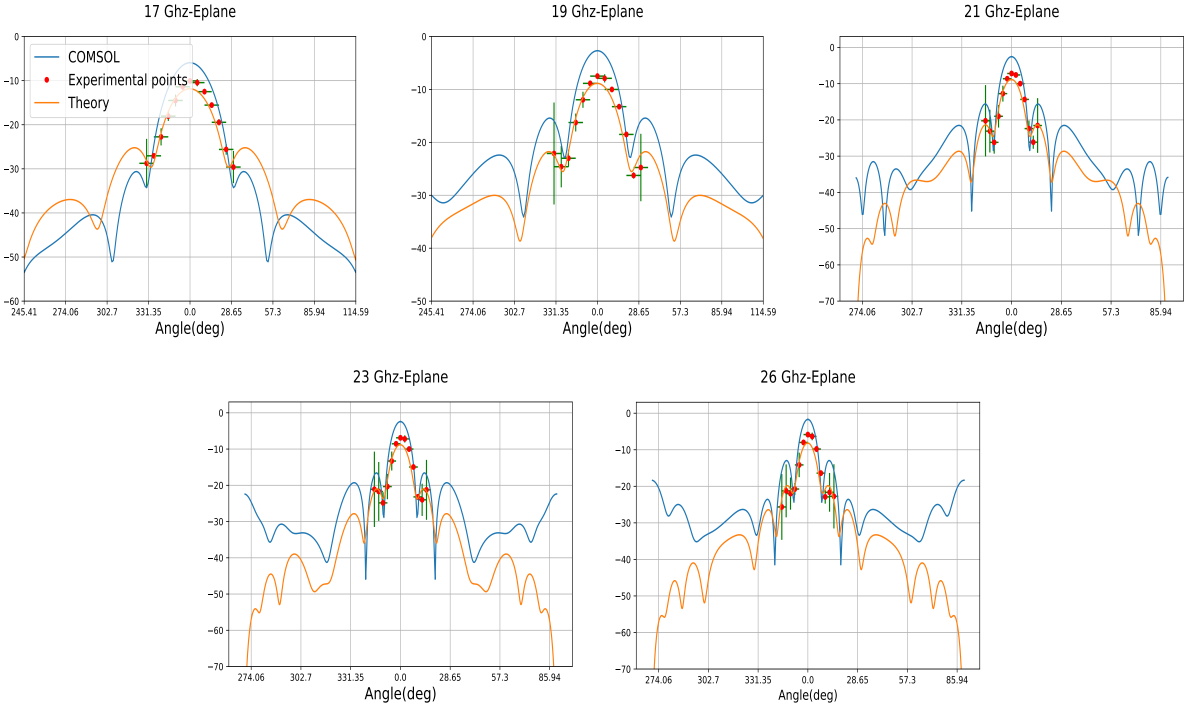

Figure A.2: Cartesian E-plane Radiation plots (dBm) at 1.53 m in K-band for pyramidal antenna with effective power

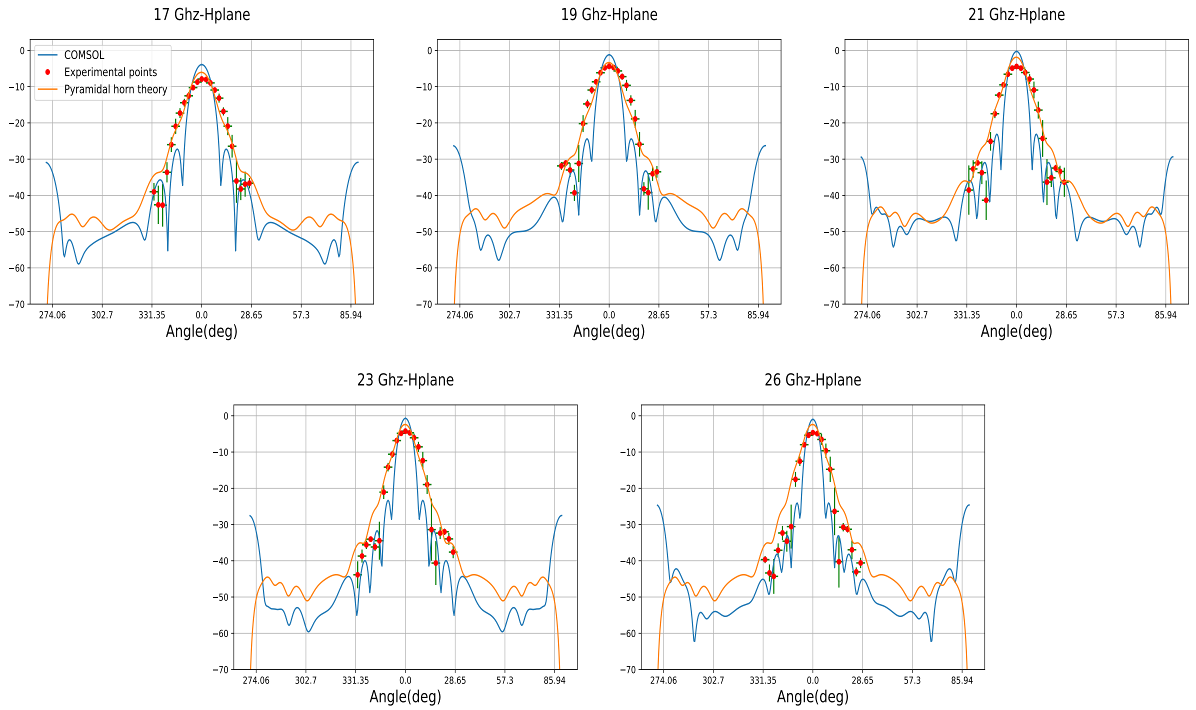

Figure A.3: Cartesian H-plane Radiation plots (dBm) at 0.63 m in K-band for hoghorn antenna with effective power

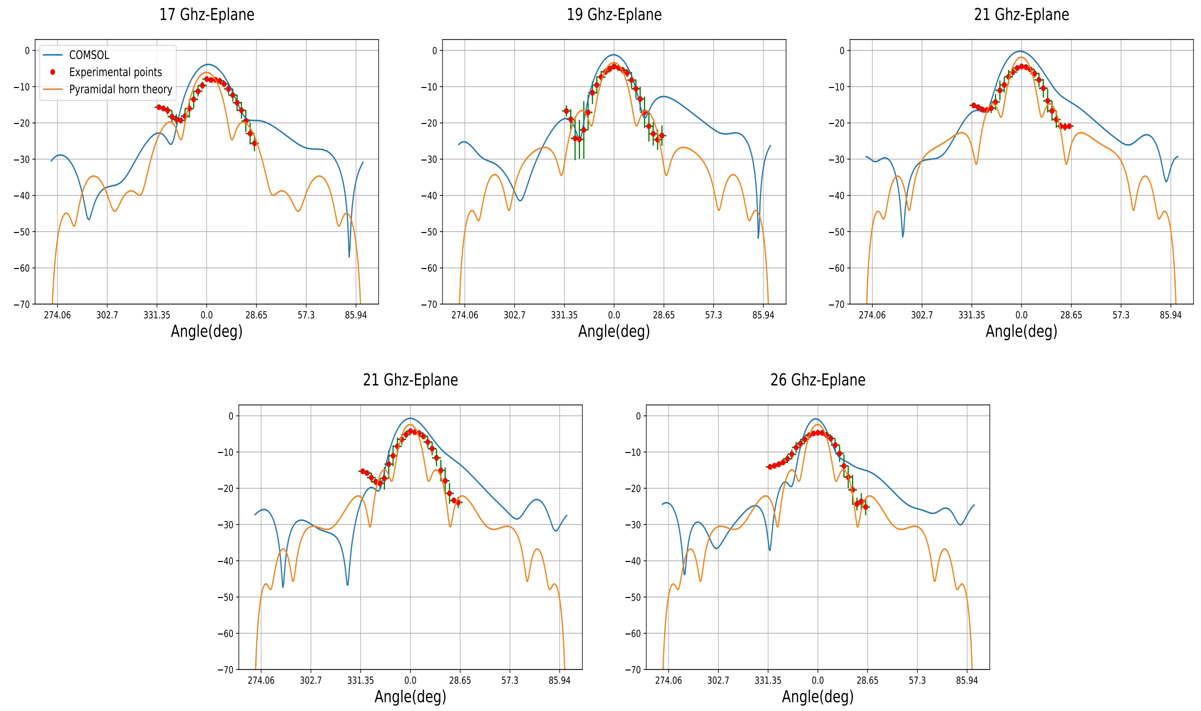

Figure A.4: Cartesian E-plane Radiation plots (dBm) at 0.63 m in K-band for hoghorn antenna with effective power

Appendix B

Effective radiated powers

In this appendix, the plots of the effective radiated powers from the antennas (see Chapter 6), as a function of the experimental frequencies, are reported for both the pyramdial horn antenna and the hoghorn antenna.

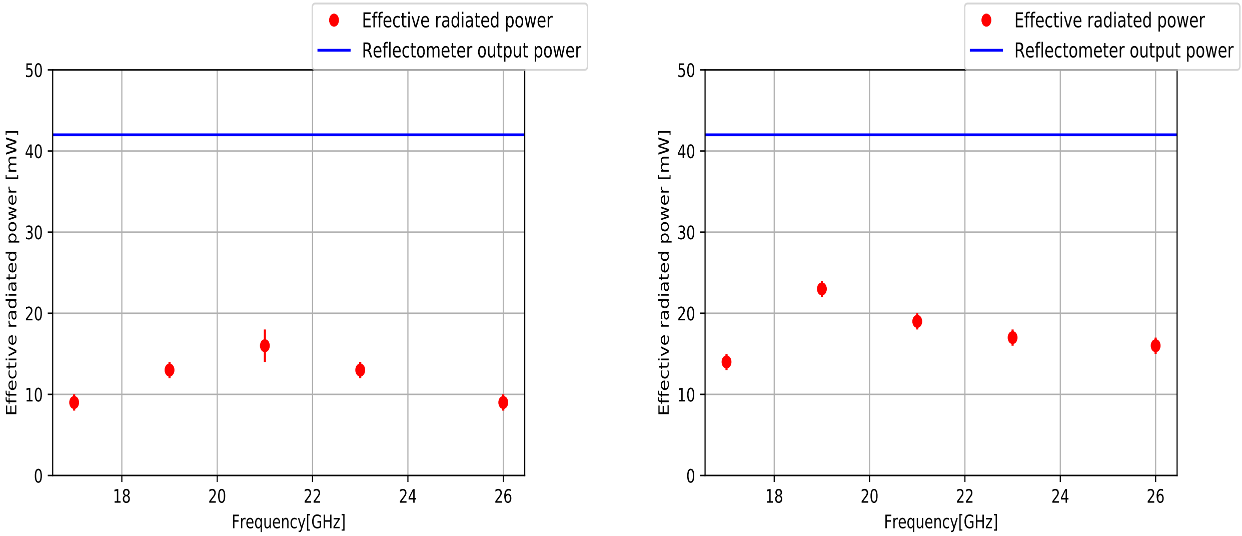

Figure B.1: Effective radiated powers for hoghorn antenna(left) and pyramidal horn antenna(right)

Appendix C

Reflectometric signals

In this appendix, the reflectometric signals obtained with both parallel and tilted antennas are reported.

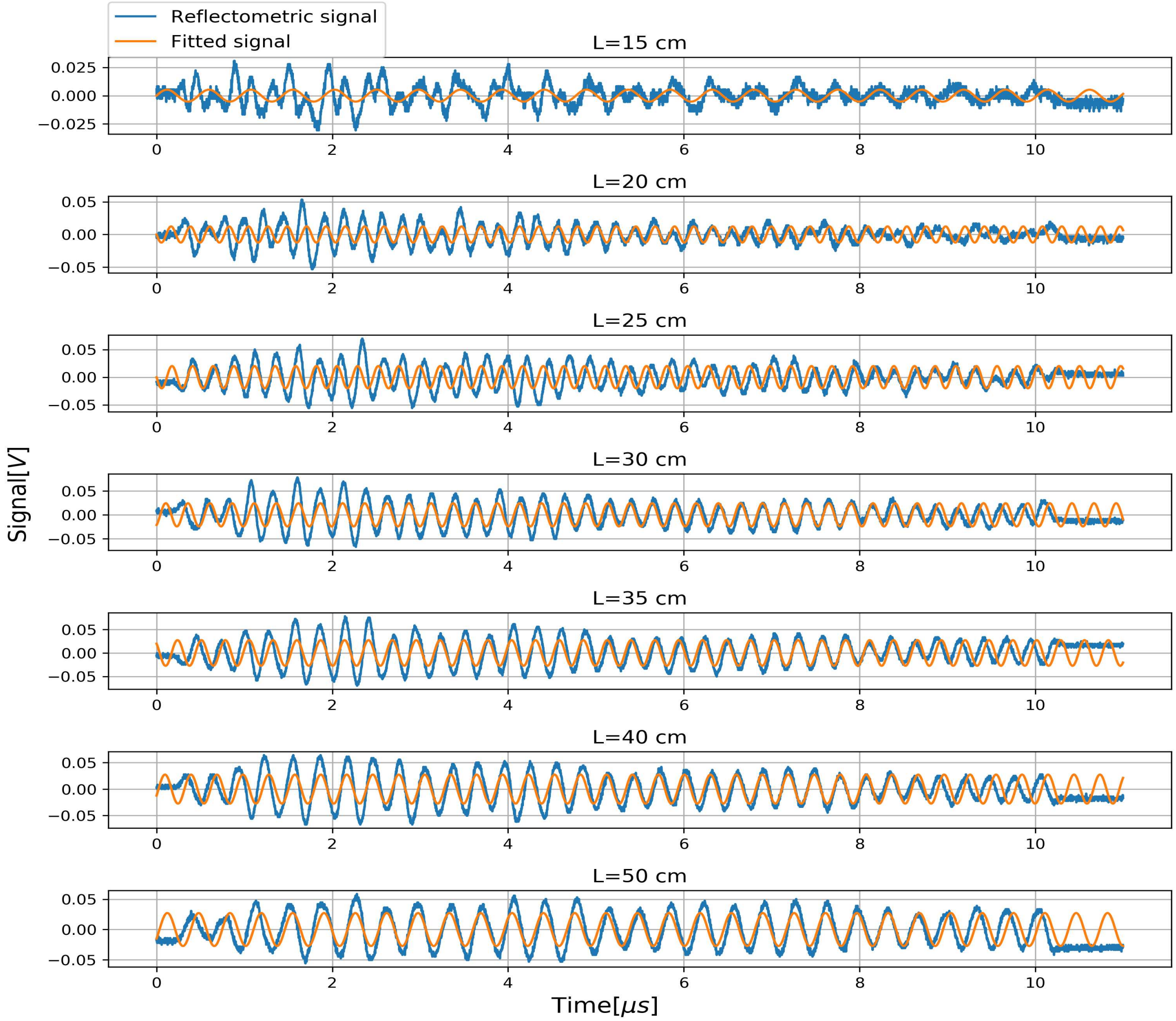

Figure C.1: Reflectometric signals and cosine fit for parallel antennas, at the different experimental distances from the mirror

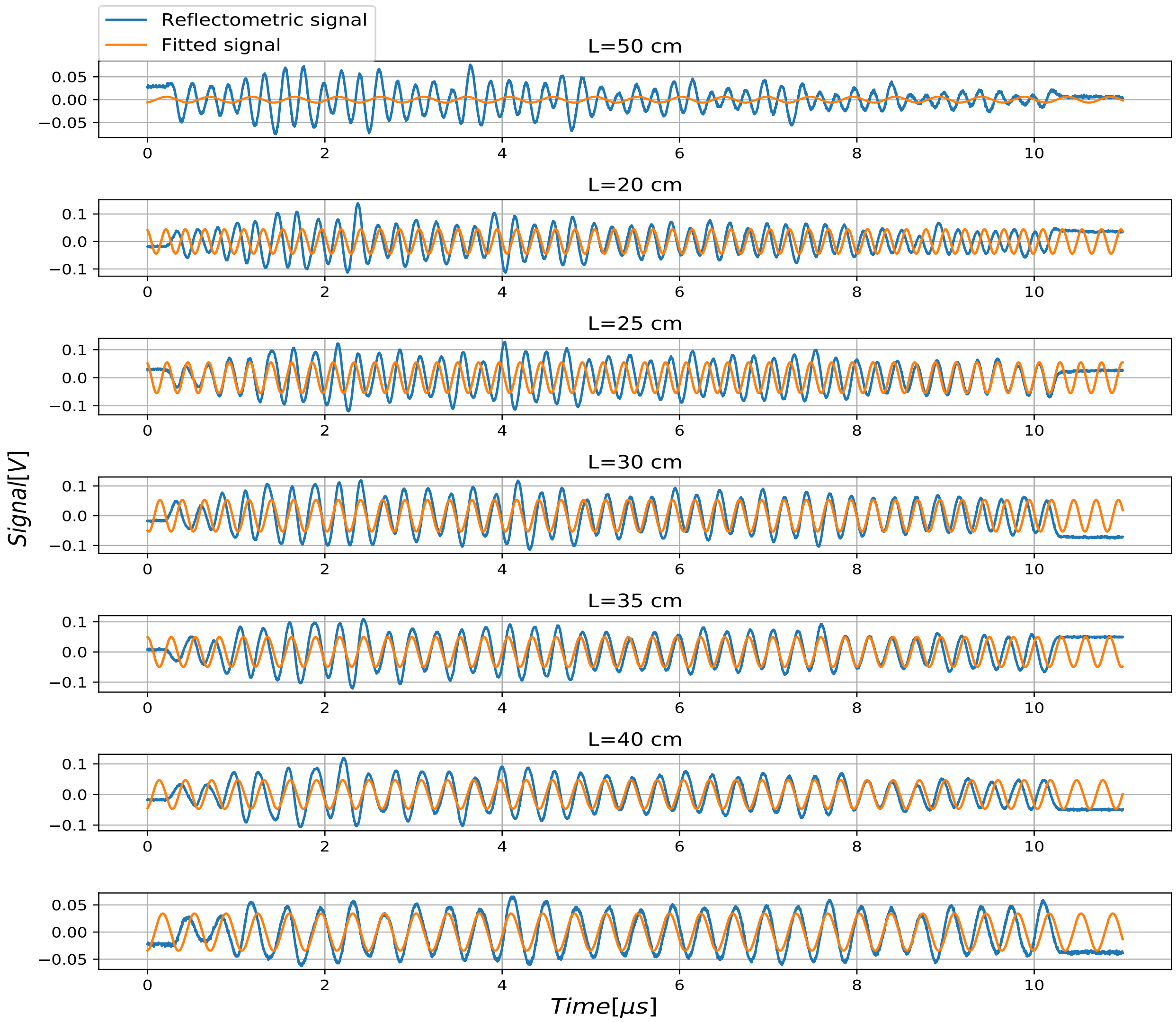

Figure C.2: Reflectometric signals and cosine fit for antennas titled of 10° with respect to each other, at the different experimental distances from the mirror

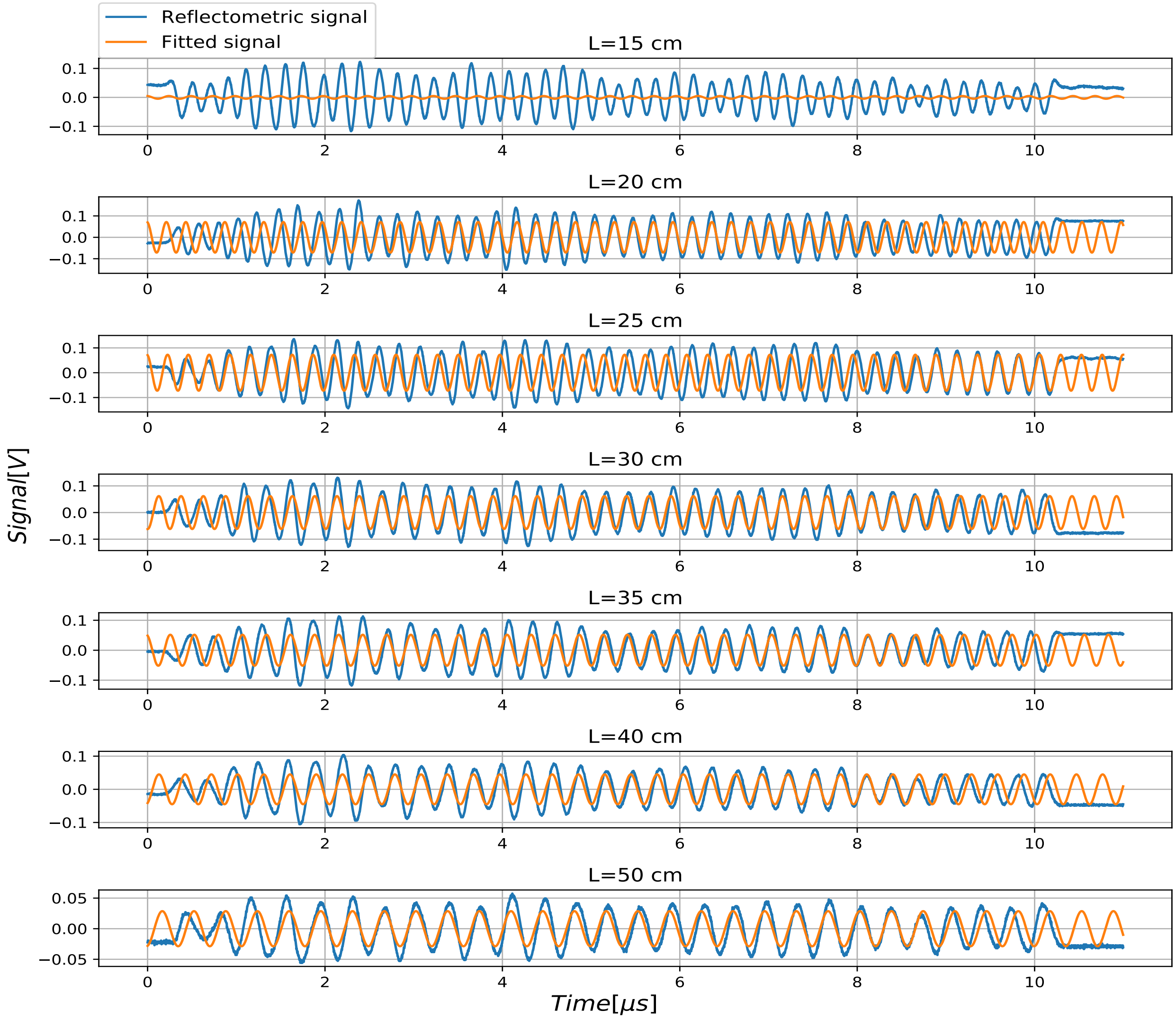

Figure C.3: Reflectometric signals and cosine fit for antennas titled of 15° with respect to each other, at the different experimental distances from the mirror

Bibliography

[1] Susan Solomon, Gian-Kasper Plattner, Reto Knutti, and Pierre Friedlingstein. Irreversible climate change due to carbon dioxide emissions. *Proceedings of the national academy of sciences*, 106(6):1704–1709, 2009.

[2] ourworldindata.org. Energy consumption by source, 2021. URL `https://ourworldindata.org/grapher/energy-consumption-by-source-and-country?stackMode=absolute&country=~OWID_WRL`.

[3] phys.libretext.org. Nuclear binding energy. URL `https://phys.libretexts.org/Bookshelves/University_Physics/Book%3A_University_Physics_%28OpenStax%29/University_Physics_III_-_Optics_and_Modern_Physics_%28OpenStax%29/10%3A__Nuclear_Physics/10.03%3A_Nuclear_Binding_Energy`.

[4] www nds.iaea.org. Evaluated nuclear data file. URL `https://www-nds.iaea.org/exfor/endf.htm`.

[5] acee.princeton.edu. 10 facts about fusion energy via magnetic confinement. URL `https://acee.princeton.edu/acee-news/10-facts-about-fusion-energy-via-magnetic-confinement/`.

[6] simic.it. New contract for the nuclear fusion – iter project. URL `https://www.simic.it/en/news-dettaglio.asp?id=1`.

[7] iter.org. Iter newsline- the lights of autumn. URL `https://www.iter.org/newsline/-/2832`.

[8] Lionello Marrelli, P Martin, ME Puiatti, JS Sarff, BE Chapman, James Robert Drake, DF Escande, and S Masamune. The reversed field pinch. *Nuclear Fusion*, 61(2):023001, 2021.

[9] G De Masi, R Cavazzana, A Fassina, E Martines, B Momo, and M Moresco. Edge density characterization in the rfx-mod experiment using the ultrafast reflectometry technique. *Nuclear Fusion*, 51(5):053016, 2011.

[10] J Santos, L Guimarãis, M Zilker, W Treutterer, M Manso, ASDEX Upgrade Team, et al. Reflectometry-based plasma position feedback control demonstration at asdex upgrade. *Nuclear Fusion*, 52(3):032003, 2012.

[11] JM Santos, GS Santos, M Zilker, L Guimarais, C Rapson, W Treutterer, and B Gonçalves. Enhancement of the asdex upgrade real-time plasma position reflectometry diagnostic. *IEEE Transactions on Nuclear Science*, 62(3):1195–1200, 2015.

[12] Giuseppe Marchiori, Gianluca De Masi, Roberto Cavazzana, Angelo Cenedese, Nicolò Marconato, Rúben Moutinho, and Antonio Silva. Study of a plasma boundary reconstruction method based on reflectometric measurements for control purposes. *IEEE Transactions on Plasma Science*, 46(5):1285–1290, 2018.

[13] G De Masi, R Cavazzana, D Abate, M Bernardi, G Marchiori, M Moresco, A Tiso, and S Peruzzo. Design of a new reflectometric system for real time plasma position control on the rfx-mod2 device. *Journal of Instrumentation*, 17(01):C01071, 2022.

[14] arstechnica.com. A third dimension helps tokamak fusion reactor avoid wall-destroying instability, 2018. URL `https://arstechnica.com/science/2018/09/a-third-dimension-helps-tokamak-fusion-reactor-avoid-wall-destroying-instability/`.

[15] David J Griffiths. Introduction to electrodynamics, 2005.

[16] Ian H Hutchinson. Principles of plasma diagnostics. *Plasma Physics and Controlled Fusion*, 44(12):2603–2603, 2002.

[17] Vitaliĭ Ginzburg. Propagation of electromagnetic waves in plasma.

[18] Niels Henrik Abel. Résolution d'un problème de mécanique. *J. Reine u. Angew. Math*, 1:153–157, 1826.

[19] Mark Chapman. Heterodyne and homodyne interferometry. *Renishaw, New Mills*, 2002.

[20] JL Doane, Eddy Mazzucato, and GL Schmidt. Plasma density measurements using fm–cw millimeter wave radar techniques. *Review of Scientific Instruments*, 52(1):12–15, 1981.

[21] A Malaquias, A Silva, R Moutinho, R Luis, A Lopes, PB Quental, L Prior, N Velez, H Policarpo, A Vale, et al. Integration concept of the reflectometry diagnostic for the main plasma in demo. *IEEE transactions on plasma science*, 46(2):451–457, 2017.

[22] merrian webster.com. URL `https://www.merriam-webster.com`.

[23] Constantine A Balanis. *Antenna theory: analysis and design*. John wiley & sons, 2015.

[24] tutorialspoint.com. Antenna theory - beamwidth. URL `https://www.tutorialspoint.com/antenna_theory/antenna_theory_beam_width.htm`.

[25] Weng Cho Chew and C-C Lu. The use of huygens' equivalence principle for solving the volume integral equation of scattering. *IEEE Transactions on Antennas and Propagation*, 41(7):897–904, 1993.

[26] Samuel Silver. *Microwave antenna theory and design*. Number 19. Iet, 1984.

[27] Antonio Orlandi. Advanced engineering electromagnetics (balanis, ca; 2012)[book review]. *IEEE Electromagnetic Compatibility Magazine*, 4(4):47–47, 2012.

[28] Albert Ruehli. Partial element equivalent circuit (peec) method and its application in the frequency and time domain. In *Proceedings of symposium on electromagnetic compatibility*, pages 128–133. IEEE, 1996.

[29] Albert Ruehli, Jan Garrett, and Clayton Paul. Circuit models for 3d structures with incident fields. In *1993 International Symposium on Electromagnetic Compatibility*, pages 28–32. IEEE, 1993.

[30] G Marchiori, R Cavazzana, G De Masi, and M Moresco. Design of the high field side antenna of the new reflectometric system for plasma position estimate in rfxmod2. *Journal of Instrumentation*, 17(01):C01002, 2022.